# Hydrothermal Syntheses, Structure, Characterization, and Structure-Property Relationships of New Mixed Metal Fluorides

---

A Dissertation

Presented to

the Faculty of the Department of Chemistry

University of Houston

---

In Partial Fulfillment

of the Requirement for the Degree

Doctor of Philosophy

---

By

Sun Woo Kim

August 2014

# Hydrothermal Syntheses, Structure, Characterization, and Structure-Property Relationships of New Mixed Metal Fluorides

_____

Sun Woo Kim

APPROVED by:

_____

Dr. P. Shiv Halasyamani, Chairman

_____

Dr. David Hoffman

_____

Dr. Angela Moeller

_____

Dr. Shoujun Xu

_____

Dr. James K. Meen

_____

Dean, College of Natural Sciences and
Mathematics

## Acknowledgments

I would like to gratefully and sincerely thank Dr. P. Shiv Halasyamani for giving me the opportunity to work his group, and for his invaluable guidance, understanding, patience, and his friendship during my graduate study at University of Houston.

I am also grateful to Dr. David Hoffman, Dr. Angela Moeller, Dr. Shoujun Xu, and Dr. James K. Meen for their kindness and their valuable time in reviewing my dissertation.

I wish to thank Dr. Hongyoung Chang, Dr. Sang-Hwan Kim, Dr. Weiguo Zhang, Dr. Elise Pachoud, Dr. Jeongho Yeon, Dr. Sau Nguyen, Hana Lee, and Thanh Thao Tran in the Dr. Halasyamani group for their support and friendship. Dr. Chris Leighton (University of Minnesota) and Dr. Elise Pachoud and Joshua Tapp performed the magnetic measurements reported in this thesis. Dr. Mark A. Green (University of Kent, UK) performed the neutron diffraction of $RbFe_2F_6$. Dr. Peter Solheid (University of Minnesota) performed the $^{57}Fe$-Mössbauer Spectroscopy measurement of $RbFe_2F_6$ and $K_4Fe_3F_{12}$. Prof. Hans-Conrad zur Loye (University of South Carolina) and Dr. Jeongho Yeon performed the UV-vis diffuse reflectance measurement of $Ba_3Mn_3F_{14}$, $NaBa_7Mn_7F_{34}$, and $CrF_3·0.5H_2O$. The remainder of the reported work, synthesis, and standard characterization were done by me.

My final and most heartfelt acknowledgment must go to my family, my wife Jiwon and my son Hyun-soon. Their support, encouragement, companionship, and sacrifice have turned my journey through graduate school into a pleasure.

**Hydrothermal Syntheses, Structure, Characterization, and Structure-**

**Property Relationships of New Mixed Metal Fluorides**

An Abstract of a Dissertation

the Faculty of the Department of Chemistry

University of Houston

In Partial Fulfillment

of the Requirement for the Degree

Doctor of Philosophy

By

Sun Woo Kim

## Abstract

Mixed-metal fluoride materials are of significant interest attributable to their important physical properties such as magnetic frustration, multiferroicity, ferroelectricity, magnetoelectricity, and non-linear optical behavior. Although a variety of synthetic strategies are known, it still remains a challenge to synthesize new mixed metal fluoride materials. The aim of this research was to synthesize new multiferroic mixed metal fluoride materials, especially materials containing mixed valence ion ($Fe^{2+}/Fe^{3+}$, $Mn^{2+}/Mn^{3+}$) with geometrical or magnetic frustration and investigate the possibility of electronic ferroelectricity or magnetic ferroelectricity as well as their functional properties. In this dissertation, I report on the hydrothermal syntheses, crystal structures, characterizations, and physical properties, and their structure-property relationships in new mixed-metal fluorides.

# Table of Contents

**CHAPTER 2. Experimental Section**

**CHAPTER 3. RbFe$^{2+}$Fe$^{3+}$F$_6$: Synthesis, Structure, and Characterization of a New Charge-ordered Magnetically Frustrated Pyrochlore-related Mixed-metal Fluoride**

**CHAPTER 4. $K_4Fe_3F_{12}$: Synthesis, Structure, and Characterization of a New Mixed Valence Iron ($Fe^{2+}/Fe^{3+}$) Fluoride Material with a Layered Perovskite-related Structure**

**CHAPTER 5. Synthesis, Structure, and Characterization of a New Mixed Valence Manganese ($Mn^{2+}/Mn^{3+}$) Fluoride Materials, $Ba_3Mn_3F_{14}$ and $NaBa_7Mn_7F_{34}$**

**CHAPTER 6. CrF$_3$·0.5H$_2$O: Synthesis, Structure, Characterization of a New Cubic**

**Pyrochlore-related Mixed-metal Fluoride**

**CHAPTER 7. Conclusions and Future Work**

xiii

# List of Tables

The following chapter is a modified version of a published paper and permission for reuse of figures and tables in the publication is granted by journal.

**CHAPTER 3.**    Kim, S. W.; Kim, S.-H.; Halasyamani, P. S.; Green, M. A.; Bhatti, K. P.; Leighton, C.; Das, H.; Fennie, C. J. "RbFe$^{2+}$Fe$^{3+}$F$_6$: Synthesis, Structure, and Characterization of a New Charge-ordered Magnetically Frustrated Pyrochlore-related Mixed-metal Fluoride" *Chem. Sci.* **2012**, *3*, 741.

**CHAPTER 1. General Introduction**

Mixed-metal fluorides are of topical interest attributable to their varied functional properties, e.g., multiferroic behavior, magnetic frustration, ferroelectricity, and non-linear optical behavior.[1] However, less research has been done compared to those in oxide materials due to difficulties of synthesis of new mixed metal fluoride materials. Also well-defined crystal structures as well as characterization of many of the fluoride materials are lacking. Thus, new synthetic methods or strategies are required to make new fluoride materials and to investigate their physical properties. In the following sections, we will discuss synthetic method of fluoride materials, crystal structures, and physical properties related to crystal structure.

**1.1 Synthesis of fluoride materials**

Mixed-metal fluoride materials are not as common as oxides, attributable to their relatively low thermal stability and hydrolysis to oxides.[1] For solid state reaction for synthesis of fluoride materials, HF, $F_2$, and $CF_4$ gases were normally used as fluorination sources as well as to prevent hydrolysis to oxides, e.g., the $BaMF_4$ families of materials were grown as crystals from the melt of $BaF_2$ and $MF_2$ in a HF atmosphere at elevated temperatures – above 800 $^o$C.[2] However, fluorination by HF, $F_2$ and $CF_4$ gases itself is very dangerous, toxic and requires a great deal of precaution for its safe handling.[1,3] Another alternative way to synthesize fluoride materials is hydrothermal or solvothermal method.[4-5] Hydrothermal or solvothermal method is an well-known technique for crystal

growth and materials processing. Hydrothermal/solvothermal usually refers to any heterogeneous reaction in the presence of aqueous solvent or organic solvent under high pressure and temperature conditions to dissolve and re-crystallize materials that are relatively insoluble under ordinary conditions. There are many examples using these techniques to obtain high quality single crystals. Although hydro-/solvothermal methods have been used to synthesize various fluoride materials, aqueous HF was added to adjust the acidity of their reactions. Aqueous HF is also difficult to use in synthetic experiments due to its toxicity and propensity to dissolve glass materials. Recently, we have developed a new synthetic method to synthesize complex fluoride materials using a $CF_3COOH$ aqueous solution instead of aqueous HF via hydrothermal route. We have previously demonstrated that this method can be used to synthesize phase-pure and polycrystalline $BaMF_4$ (M = Mg, Mn, Co, Ni and Zn).[6] We are arguing that a $CF_3COOH$ aqueous solution could generate in situ aqueous HF under hydrothermal conditions. Possible reaction mechanisms are as follow:

$$BaF_2(s) + 2CF_3COOH(aq) \rightarrow (CF_3COO)_2Ba(aq) + 2HF(aq) \text{ (1)}$$

$$MF_2(s) + 2CF_3COOH(aq) \rightarrow (CF_3COO)_2M(aq) + 2HF(aq) \text{ (2)}$$

$$(CF_3COO)_2Ba(aq) + (CF_3COO)_2M(aq) + 4HF(aq) \rightarrow BaMF_4(s) + 4CF_3H + 4CO_2 \uparrow \text{ (3)}$$

First of all, the reaction of metal fluoride and $CF_3COOH$ aqueous solution under hydrothermal conditions generated metal trifluoroacetate salts and aqueous HF in situ. After that, in situ intermediates reacted with each other, finally producing $BaMF_4$. This

synthetic method could be applied to synthesize other complex fluoride materials, especially mixed valence transition metal ($Fe^{2+}/Fe^{3+}$, $Mn^{2+}/Mn^{3+}$) fluoride materials.[7]

## 1.2 Crystal structures of fluoride materials

Because of strong ionic character of fluorine bonds as well as low polarizability of fluorine ion, crystal structures of fluoride materials are relatively simple and the structural distortions in the crystal structure are very difficult to observe compared to oxide materials.[1,8] Generally, the crystal structure of transition metal fluoride materials exhibit octahedral coordination environment and isolated, corner-sharing, edge-sharing, or face-sharing octahedra can be observed in the crystal structure.[8] Also various structural forms could exist and unusual physical properties are derived from those structures.

### 1.2.1 Three dimensional structures in fluoride materials

In three dimensional framework structure in fluoride materials, perovskites ($AM^{2+}F_3$), hexagonal or tetragonal bronzes ($A_xMF_3$), pyrochlores ($AM^{2+}M^{3+}F_6$), and weberites ($A_2M^{2+}M^{3+}F_7$) structure can be observed (See Figure 1.1).[8] Their physical properties are derived from the various atomic occupation of different crystallographic sites in each lattice. Especially, in pyrochlore-related fluoride materials, the crystal structure of various $AM^{2+}M^{3+}F_6$ (A = $K^+$, $Rb^+$, $Cs^+$, $NH_4^+$; $M^{2+}$ = $Mg^{2+}$, $Mn^{2+}$, $Fe^{2+}$, $Co^{2+}$, $Ni^{2+}$, $Cu^{2+}$ ; $M^{3+}$ = $Al^{3+}$, $Ga^{3+}$, $V^{3+}$, $Cr^{3+}$, $Fe^{3+}$) materials were investigated.[9-10] Interestingly, both

crystallographic disorder and order are observed between the $M^{2+}$ and $M^{3+}$ cations on the octahedral sites.[7,9-14] Depending on the crystallographic disorder and order in $M^{2+}$ and $M^{3+}$, lowering crystallographic symmetry is also observed (cubic vs. orthorhombic).[7,12-14]
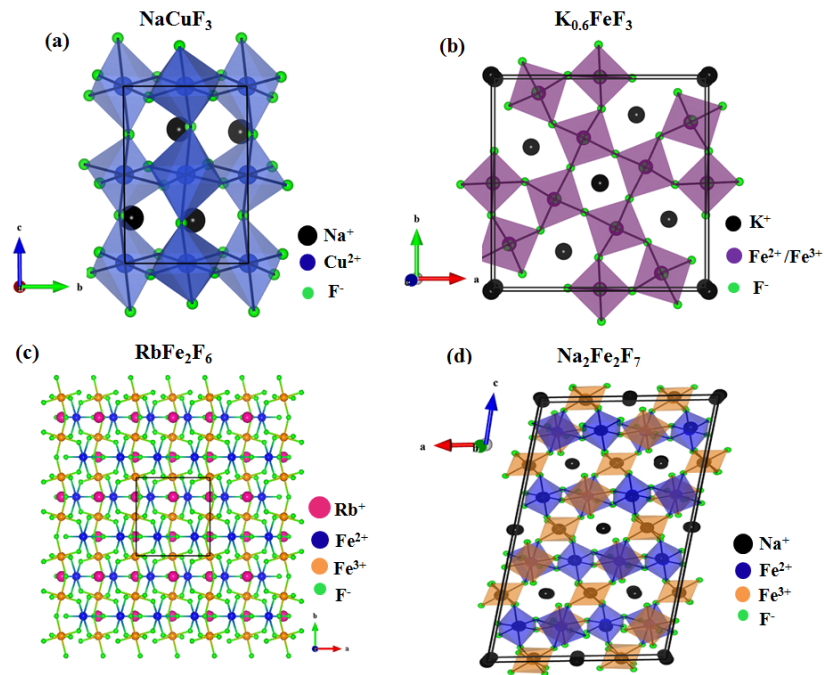


**Figure 1.1** Examples of three dimensional structures in fluoride materials: (a) Perovskite $(NaCuF_3)$,[15] (b) Bronze $(K_{0.6}FeF_3)$,[16] (c) Pyrochlore $(RbFe_2F_6)$,[7] and (d) Weberite $(Na_2Fe_2F_7)$.[17]

## 1.2.2 Layered structures in fluoride materials

In layered structures in fluoride materials, single layered, double layered and triple layered materials are observed.[8] Their physical properties are derived from the various

atomic occupation of different crystallographic sites in each lattice. Depending on the connection of corner-shared octahedra (cis or trans) in the crystal structure, various layered structures can be obtained. Examples of layered structure of fluoride materials are shown in Figure 1.2.
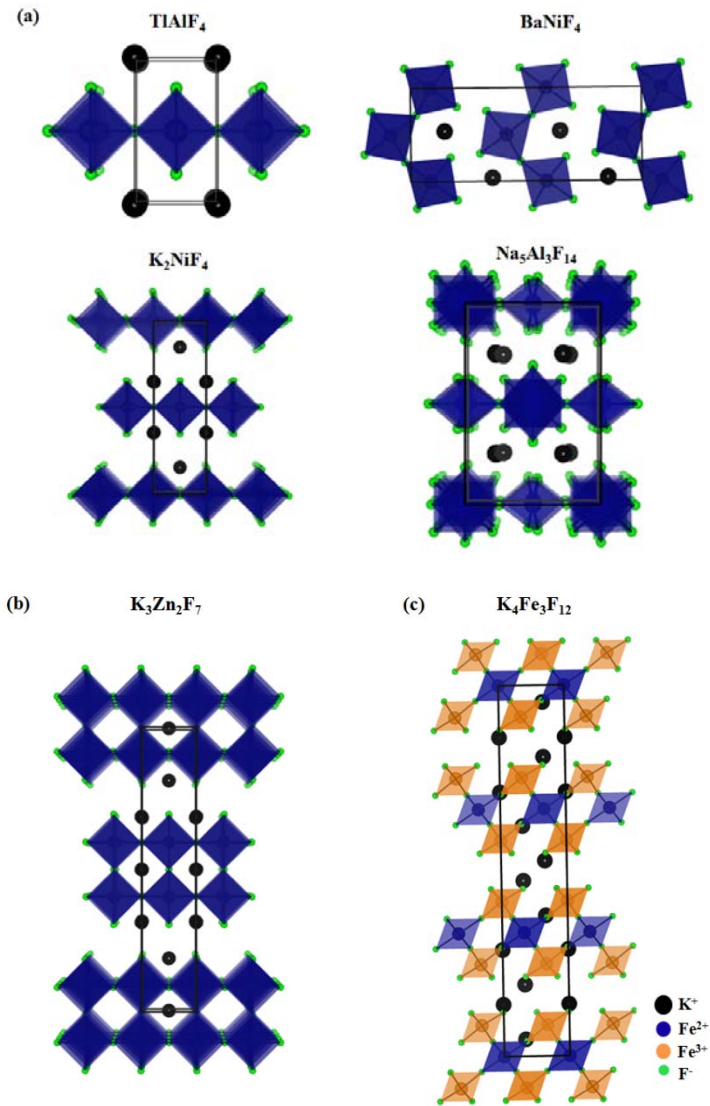


**Figure 1.2** Examples of layered structures in fluoride materials: (a) single layered structures (TlAlF$_4$,[18] BaNiF$_4$,[6] K$_2$NiF$_4$,[19] and Na$_5$Al$_3$F$_{14}$[20]), (b) double layered structure (K$_3$Zn$_2$F$_7$),[21] and (c) triple layered structure (K$_4$Fe$_3$F$_{12}$).

## 1.2.3 Chain structures in fluoride materials

In chain structures in fluoride materials, single chain, double chain, and triple chain materials can be observed.[8] From single chain fluoride materials, trans- or cis-type chain are found in the crystal structures. Examples of chain structures of fluoride materials are shown in Figure 1.3.
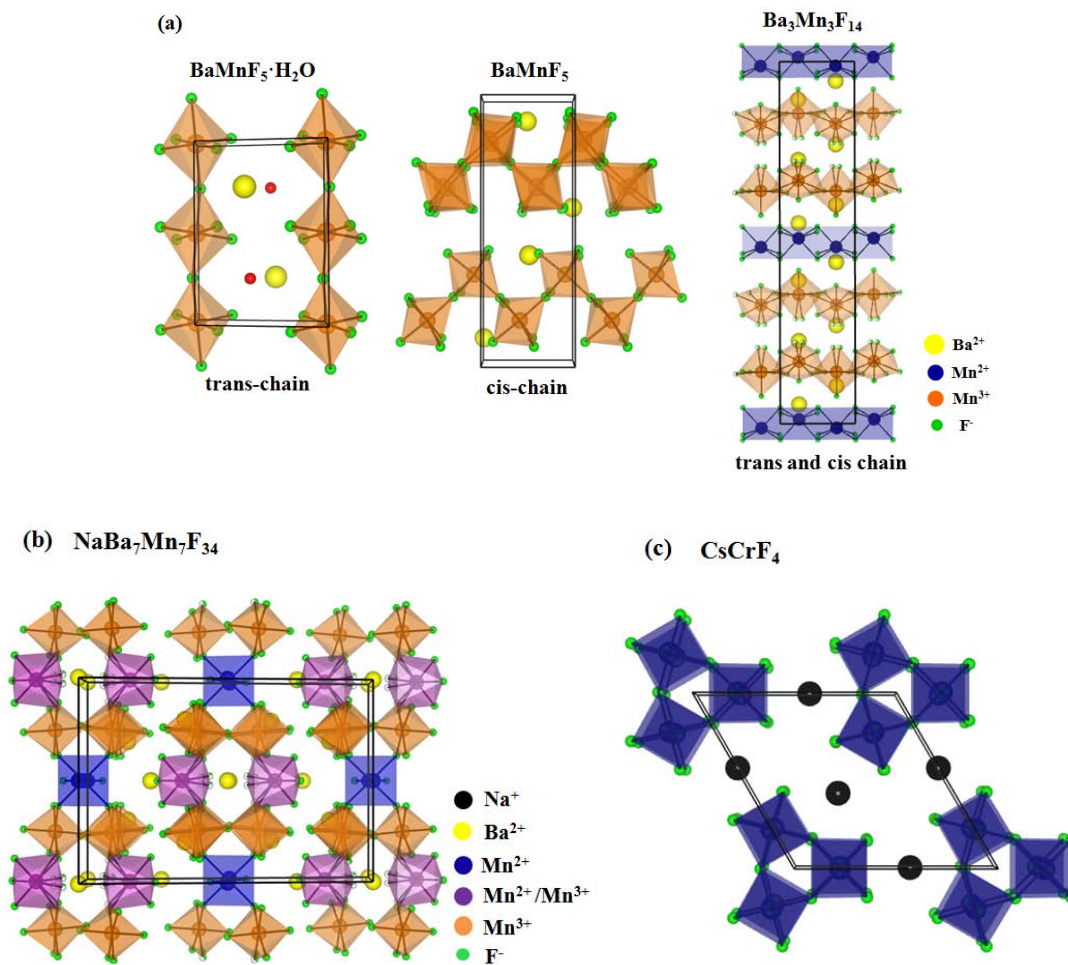


**Figure 1.3** Examples of chain structures in fluoride materials: (a) single chain structures ($BaMnF_5 \cdot H_2O$,[22] $BaMnF_5$,[23] $Ba_3Mn_3F_{14}$), (b) double chain structure ($NaBa_7Mn_7F_{34}$), and (c) triple chain structure ($CsCrF_4$).[24]

## 1.3 Physical properties of fluoride materials

  Because fluorine is the most electronegative element and has small ionic size, it leads to uncommon properties, for example, large optical transmission domain, high resistivity and anionic conductivity.[1] In addition, the $\pi$-donor character and the absence of any $\pi$-acceptor character of the fluorine ions essentially determine its low crystalline field (high-spin) character and the fluorine ion produces more effective super-exchange interaction between magnetic cations than do oxygen, thus fluoride materials show excellent magnetic properties.


### 1.3.1 Magnetic properties

  For magnetic properties, materials must have partially filled d or f shells of transition metal or rare-earth cations and exchange interactions between magnetic cations generate magnetic ordering, such as paramagnetic, anti-ferromagnetic, ferromagnetic, or ferrimagnetic ordering (See Figure 1.4). Paramagnetism has unpaired electrons randomly arranged, thus the spin of a paramagnetic material is easily able to be aligned by an applied magnetic field. Anti-ferromagnetic ordering has unpaired electrons aligned anti-parallel, thus there is no net magnetic moment. Ferromagnetic ordering has all unpaired electrons aligned, thus it shows a net magnetic moment without an applied magnetic field. Ferrimagnetic ordering has unpaired electrons aligned partially anti-parallel, thus it shows a net magnetic moment without an applied magnetic field because of different magnitude of adjacent spins.
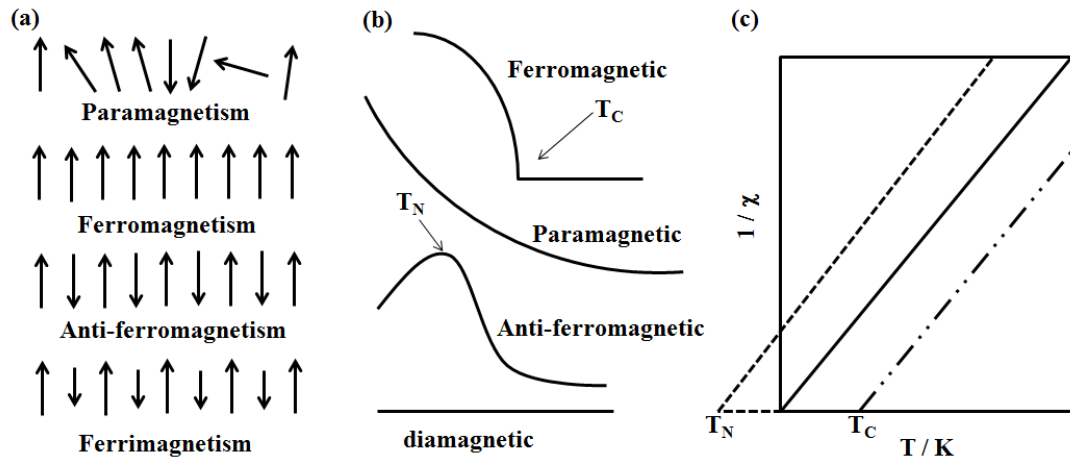
**Figure 1.4** Examples of magnetic behavior: (a) illustration of magnetic ordering, (b) diagram of magnetic susceptibility vs. temperature, and (c) diagram of inverse magnetic susceptibility vs. temperature.

Magnetic susceptibility is the quantitative measure of the response of a material under an applied magnetic field and is described by the following equation:

$$\chi = \frac{M}{H} \qquad (4)$$

where $\chi$ is the magnetic susceptibility, M is the magnetization and H is the applied magnetic field.

The Curie law describes the temperature dependence of paramagnetism. For Curie law,

$$\chi = \frac{C}{T} \qquad (5)$$

where C is the Curie constant and T is temperature. The Curie constant (C) is described by the following equation:

8

$$C = \frac{Ng^2\mu_B{}^2}{3k} S(S + 1) \quad (6)$$

where N is Avagadro's number, g is the Lande g factor, $\mu_B$ is Bohr magneton, k is Boltzman constant, and S is the spin quantum number.

The Curie-Weiss law describes the temperature dependence of ferromagnetism or anti-ferromagnetism. For Curie-Weiss law,

$$\chi = \frac{C}{T-\theta} \quad (7)$$

where C is the Curie constant, T is temperature, and $\theta$ is the Weiss constant.

In order to predict magnetic properties of materials from their crystal structures, super-exchange interactions can be used for describing the magnetic coupling. Super-exchange interaction defined as the strong magnetic coupling, usually anti-ferromagnetic coupling between two next-to-nearest magnetic cations connected by non-magnetic anions ($O^{2-}$ or $F^-$).[25-26] Depending on the bond angle between the magnetic cations through the non-magnetic anion as well as on the spin configuration of each magnetic cation, different types and degrees of magnetic coupling are expected according to the Goodenough-Kanamori's rule.[27-29] For example, NiO shows strong anti-ferromagnetic interactions attributable to the 180° type super-exchange couplings between $Ni^{2+}$ ($d^8$) and $Ni^{2+}$ ($d^8$) connected by $O_{2p}$ orbitals.[26]
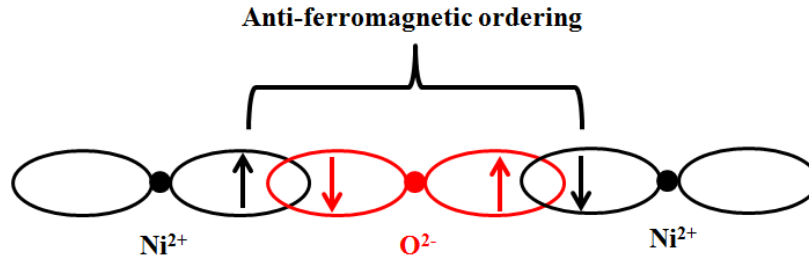
**Figure 1.5** Schematic illustration of the super-exchange interaction ($Ni^{2+}$ - $O_{2p}$ - $Ni^{2+}$) in NiO.

## 1.3.2 Geometrical frustration

Geometrical frustration could be mostly observed from anti-ferromagnetic ordering in 3D or 2D frustrated lattices, e.g., pyrochlore (3D), tetrahedron (3D), triangular (2D) or kagome net (2D) (See Figure 1.6). Attributable to the presence of frustration in crystal lattice, it prevents the easy formation of spin-ordered state (anti-ferromagnetic ordering). Thus, unusual magnetic properties can be induced from these phenomena such as quantum spin liquid, spin glass or spin ice behavior. An excellent review of geometrical frustration was reported by Ramirez.[30] The degree of frustration is obtained by the ratio of the Weiss temperature ($\theta_w$) and the anti-ferromagnetic ordering temperature ($T_N$) ($|\theta_w|/T_N$). If the frustration parameter ($|\theta_w|/T_N$) is higher than 10, it indicates that the magnetic moment might be geometrically frustrated.
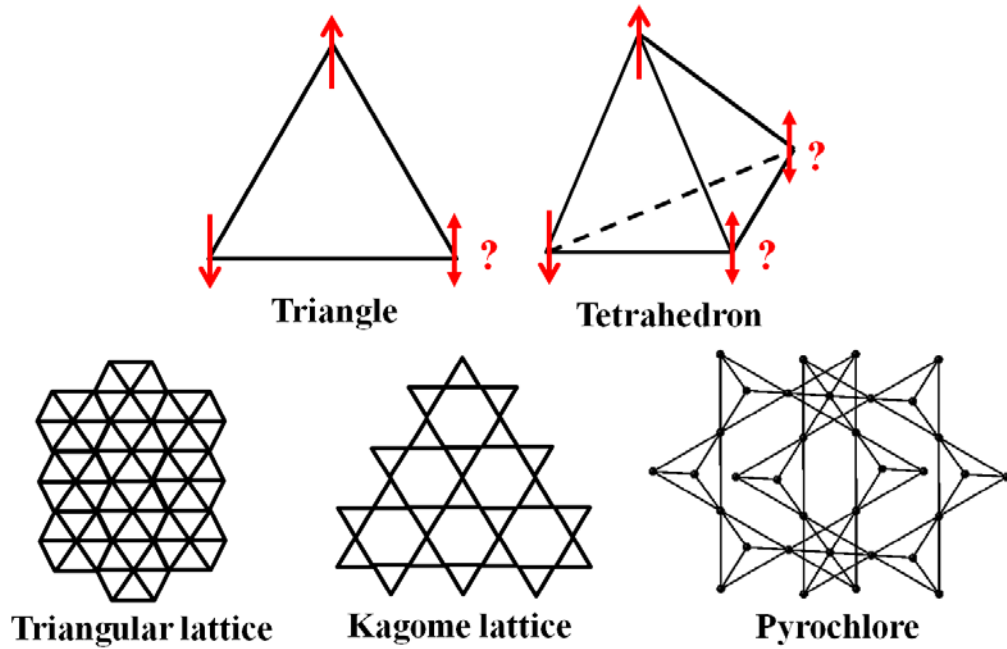
**Figure 1.6** Illustration of geometrical frustration in frustrated crystal lattices.

### 1.3.3 Second Harmonic Generation (SHG)

Second harmonic generation (SHG), or frequency doubling is a special case of the nonlinear optical process, in which photons interacting with a nonlinear material are effectively combined to form new photons with twice the energy. Therefore, twice the frequency and half the wavelength of the initial photons are generated. When the dipole moments of the NCS material respond instantaneously to an applied electric field, the induced polarization, $P$(t), at time t in a medium can be expressed as the following power series in the electrical field.

$$P(t) \propto \chi^{(1)}E(t) + \chi^{(2)}E(t) + \chi^{(3)}E(t) + \cdots$$

Here, the coefficients $\chi^{(n)}$ are the n-th order susceptibilities of the medium. For any mixing process, the second-order term is crucial, because it only results in non-zero values of the susceptibility in media with no inversion symmetry. $\chi^{(2)}$ expressed as $\chi_{ijk}$ can be replaced by experimental $d_{ijk}$ coefficients, where $2d_{ijk} = \chi_{ijk}$. Since Perry and Kurtz[31] developed the SHG measurements with polycrystalline samples, the SHG efficiency and type I phase-marching information can be determined. Figure 1.7 represents the phase-matching or non-phase-matching behavior of the reference materials. In type I phase-matching, two photons with ordinary polarization will combine to generate one photon with double frequency and extraordinary polarization. In other words, it occurs when the phase velocity of the fundamental radiation equals the second harmonic. Also, with phase-matching behavior, the SHG efficiency increases as the particle size increases. However, with non-phase-matching behavior, the SHG efficiency increases to a maximum until the particle size increase at certain point and decreases as further increases of particle size. In addition, on the basis of the SHG efficiency and phase-matching behavior, the average non-linear optical (NLO) susceptibility, $<d_{eff}>$ with units of pm/V, can be determined by the following equations.[32]

$$< d_{eff} >_{PM} = \left\{ \frac{I^{2\omega}(A)}{I^{2\omega}(LiNbO_3)} (7.98 \times 10^2) \right\}^{1/2} \quad (8)$$

$$< d_{eff} >_{NPM} = \left\{ \frac{I^{2\omega}(A)}{I^{2\omega}(SiO_2)} (0.3048) \right\}^{1/2} \quad (9)$$

The SHG efficiency of the material is either compared with that of $LiNbO_3$ (SHG efficiency of $600 \times \alpha\text{-}SiO_2$) or with that of $SiO_2$ depending on whether the material is type I phase-matching (PM) or non-phase-matching (NPM).
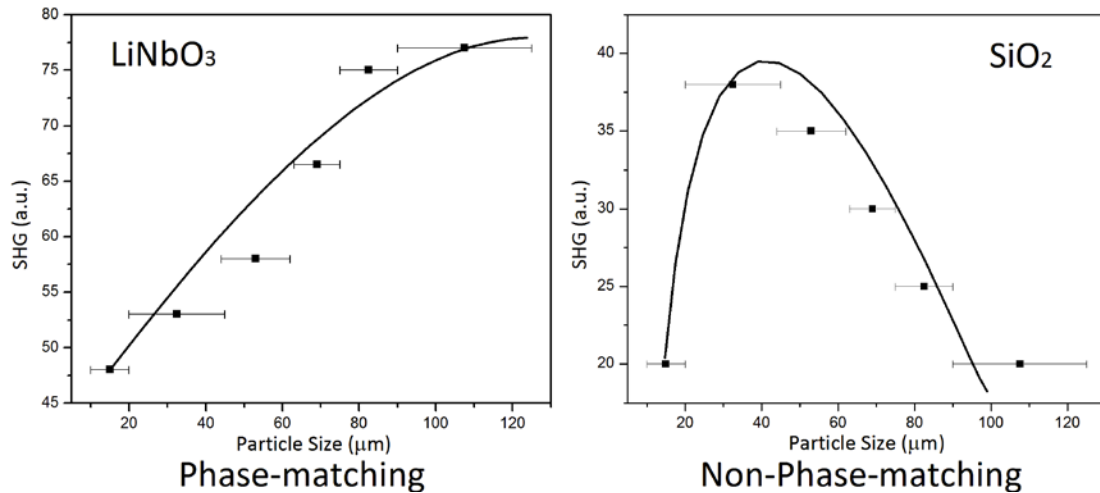


**Figure 1.7** Examples of Type I SHG phase-matching and non-phase-matching curves.[32] The curves are drawn to guide the eye and are not fits to the data.

## 1.3.4 Ferroelectricity

Ferroelectric materials can be formally defined as pyroelectric materials exhibiting a spontaneous electric polarization that can be reversed by an applied external electric field.[33] Therefore, the materials must be polar so that they have a permanent dipole moment. As found in pyroelectric materials, in order for a material to exhibit ferroelectric behavior, it must crystallize in one of the ten polar crystal classes, i.e. 1, 2, 3, 4, 6, m, mm2, 3m, 4mm, or 6mm. However, although the polarization reversal is not required in pyroelectric, the polarization observed in a ferroelectric can be reversed

under an applied electric field. One of the interesting features is the ferroelectric hysteresis loop determined by measuring the polarization change of the material, in $\mu C/cm^2$, as a function of applied voltage, V (see Figure 1.8).
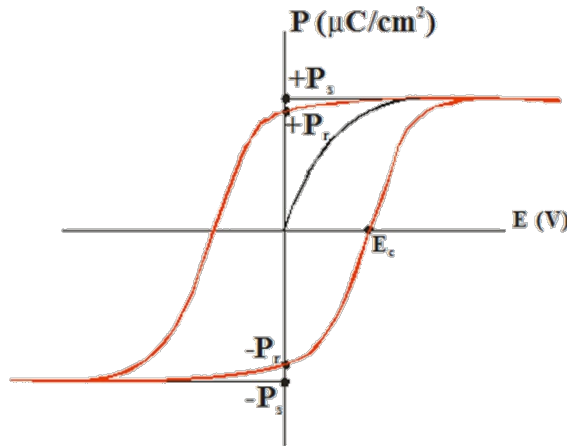


**Figure 1.8** Ferroelectric hysteresis loop (polarization (P) versus applied voltage (E)). $P_s$ is the spontaneous polarization, $P_r$ is the remanent polarization, and $E_c$ is the coercive field.

Another interesting feature found in ferroelectrics is a phase transition from non-centrosymmetric to centrosymmetric structures at a certain temperature called the Curie temperature. $(NH_4)_2BeF_4$[34] and $SrAlF_5$[35] are known ferroelectric fluoride materials.

### 1.3.5 Multiferroicity

Multiferroicity is defined as the simultaneous coexistence of at least two ferroic properties, e.g., ferromagnetism (or anti-ferromagnetism, ferrimagnetism), ferroelectricity (or anti-ferroelectricity), and ferroelasticity in the same material (See

Figure 1.9).[36-38] For multiferroic fluoride materials, the $BaMF_4$ ($M^{2+}$ = Mg, Mn, Co, Ni, and Zn) family[2,39-42], the $K_3Fe_5F_{15}$ ($K_3Fe_2Cu_3F_{15}$ and $K_3Fe_3Cr_2F_{15}$) family[16,43-50], and the $Pb_5Cr_3F_{19}$ family[51] have been investigated.[52-53]

In order to design new multiferroic materials, it is very important to understand how to combine magnetism and ferroelectricity in the same material. There are 4 possible approaches to induce macroscopic electric polarization (ferroelectricity) in a multiferroic material.

The first approach is to target lone-pair multiferroics. In the perovskite structure $ABO_3$, examples have an A site occupied by a stereo-active lone pair cation such as $Pb^{2+}$ or $Bi^{3+}$, which could induce ferroelectricity, and a B site occupied by a magnetic cation, which generates magnetic properties. $BiFeO_3$,[54] $BiMnO_3$,[55] and $PbVO_3$[56] are examples of lone-pair multiferroics (Class I).

The second approach is using charge ordering phenomena. Charge ordering is often observed in transition metal materials, especially containing mixed valence magnetic cations with geometrical or magnetic frustration. These mixed valence cations may generate a polar arrangement, which induced possible ferroelectricity.[57] $Fe_3O_4$,[58] $LuFe_2O_4$,[59] $K_3Fe_5F_{15}$[60] are examples of charge ordering multiferroics (Class I).
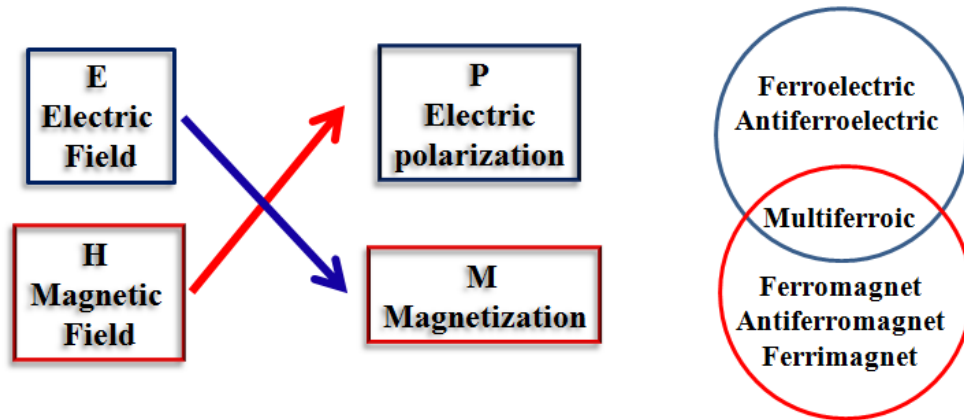
**Figure 1.9** Schematic illustration of multiferroic properties: coupling between electric and magnetic properties.

The third approach is to target geometric ferroelectricity. A structural phase transition at high temperature can generate ferroelectricity. For example, $YMnO_3$ show a ferroelectric phase transition at around 1300 K due to the tilting of the MnO5 bipyramid block (Class I). [61]

The last approach is to target magnetic multiferroics. Ferroelectricity is induced by magnetic long-range ordering. Macroscopic electric polarization occur because of particular spiraling magnetic phase or collinear magnetic structure. $TbMnO_3$,[62] $TbMn_2O_5$,[63] $Ni_3V_2O_8$,[64] $MnWO_4$,[65] $Ca_3CoMnO_6$[66] are examples of magnetic multiferroics (Class II).

## 1.4 Outline of dissertation

In order to find new multiferroic fluoride materials, exploratory experiments were performed to synthesize new mixed valence transition metal ($Fe^{2+}/Fe^{3+}$, $Mn^{2+}/Mn^{3+}$) fluoride materials with the concept of mixed valence ions with geometrical or magnetic frustration. Through the hydrothermal method using $CF_3COOH$ aqueous solutions, several new fluoride materials were synthesized and characterized. Powder and single crystal X-ray diffraction were used to determine the phase purity of the materials, as well as their crystal structures. For newly synthesized materials, infrared, Uv-vis diffuse spectroscopy, and thermal analyses such as thermogravimetric analysis (TGA) or differential thermal analysis (DTA) and magnetic property measurements were utilized to characterize the materials. The bond valence sum (BVS)[67-69] calculation was used for determination of the oxidation state of the transition metal ion. For mixed valence iron ($Fe^{2+}/Fe^{3+}$) fluoride materials, $^{57}$Fe‑Mössbauer spectroscopy was used to characterize the ratio of $Fe^{2+}$ and $Fe^{3+}$.

In Chapter 2, all of the experimental details will be described.

In Chapter 3, a new charge-ordered magnetically frustrated mixed-metal fluoride with a pyrochlore-related structure, $RbFe_2F_6$ will be introduced. Synthesis, structure, characterization and magnetic property will be discussed.

In Chapter 4, synthesis, structure, and characterization of a new mixed valence iron ($Fe^{2+}/Fe^{3+}$) fluoride material with a triple layered perovskite-related structure, $K_4Fe_3F_{12}$ will be discussed.

In Chapter 5, two new mixed valence manganese ($Mn^{2+}/Mn^{3+}$) fluoride materials, $Ba_3Mn_3F_{14}$ and $NaBa_7Mn_7F_{34}$ will be introduced. Syntheses, crystal structures, characterization, and magnetic propertied of the two new materials will be discussed.

In Chapter 6, synthesis, crystal structure, characterization of a cubic pyrochlore fluoride material, $CrF_3 \cdot 0.5H_2O$ will be discussed.

Finally, in Chapter 7, general conclusions will be given. In addition, important future works for each system will be suggested.

## 1.5 References

(1)     Hagenmuller, P. *INORGANIC SOLID FLUORIDES Chemistry and Physics*; Academic Press, INC.: Orlando, 1985.

(2)     Eibschutz, M. G., H. J. *Solid State Commun.* **1968**, *6*, 737.

(3)     Tressaud, A. *Functionalized Inorganic Fluorides Synthesis, Characterization & Properties of Nanostructured Solids*; John Wiley & Sons, Ltd, 2010.

(4)     Feng, S.; Xu, R. *Acc. Chem. Res.* **2000**, *34*, 239.

(5)     Byrappa, K. Y., M. *Handbook of Hydrothermal Technology: Technology for Crystal Growth and Materials Processing.* ; Noyes Publications /William Andrew Publishing, LLC, 2001.

(6)     Kim, S. W.; Chang, H. Y.; Halasyamani, P. S. *J. Am. Chem. Soc.* **2010**, *132*, 17684.

(7)     Kim, S. W.; Kim, S.-H.; Halasyamani, P. S.; Green, M. A.; Bhatti, K. P.; Leighton, C.; Das, H.; Fennie, C. J. *Chem. Sci.* **2012**, *3*, 741.

(8)     Massa, W.; Babel, D. *Chem. Rev.* **1988**, *88*, 275.

(9)     Babel, D.; Pausewang, G.; Viebahn, W. *Z. Naturforsch., B* **1967**, *22*, 1219.

(10)    Babel, D. *Z. Anorg. Allg. Chem.* **1972**, *387*, 161.

(11)    Kurtz, W.; Roth, S. *Physica B+C* **1977**, *86–88, Part 2*, 715.

(12)    Ferey, G.; Leblanc, M.; De, P. R.; Pannetier, J. *Solid State Commun.* **1985**, *53*, 559.

(13)    Baum, E.; Dahlke, P.; Kaiser, V.; Molinier, M.; Schmidt, R. E.; Pebler, J.; Massa, W.; Babel, D. *Z. Anorg. Allg. Chem.* **2006**, *632*, 2244.

(14)     Molokeev, M. S.; Bogdanov, E. V.; Misyul, S. V.; Tressaud, A.; Flerov, I. N. *J. Solid State Chem.* **2013**, *200*, 157.

(15)     Kaiser, V.; Otto, M.; Binder, F.; Babel, D. *Z. Anorg. Allg. Chem.* **1990**, *585*, 93.

(16)     Hardy, A. M.; Hardy, A.; Ferey, G. *Acta Cryst. B* **1973**, *29*, 1654.

(17)     Yakubovich, O.; Urusov, V.; Massa, W.; Frenzen, G.; Babel, D. *Z. Anorg. Allg. Chem.* **1993**, *619*, 1909.

(18)     Fourquet, J. L.; Plet, F.; Courbion, G.; Bulou, A.; De Pape, R. *Rev. Chim. Miner.* **1979**, *16*, 490.

(19)     Balz, D.; Plieth, K. *Z. Elektrochem. Angew. Phys. Chem.* **1955**, *59*, 545.

(20)     Brosset, C. *Z. Anorg. Allg. Chem.* **1938**, *238*, 201.

(21)     Herdtweck, E.; Babel, D. *Z. Kristallogr.* **1980**, *153*, 189.

(22)     Massa, W.; Burk, V. *Z. Anorg. Allg. Chem.* **1984**, *516*, 119.

(23)     Bukovec, P.; Hoppe, R. *Z. Anorg. Allg. Chem.* **1984**, *509*, 138.

(24)     Babel, D.; Knoke, G. *Z. Anorg. Allg. Chem.* **1978**, *442*, 151.

(25)     Kramers, H. A. *Physica (The Hague)* **1934**, *1*, 182.

(26)     Anderson, P. W. *Phys. Rev.* **1959**, *115*, 2.

(27)     Goodenough, J. B. *Phys. Rev.* **1955**, *100*, 564.

(28)     Kanamori, J. *J. Phys. Chem. Solid* **1959**, *10*, 87.

(29)     Goodenough, J. B. *Magnetism and the Chemical Bond*; Interscience: New York, 1963.

(30)     Ramirez, A. *Comments. Cond. Mat. Phys.* **1996**, *18*, 21.

(31)     Kurtz, S. K.; Perry, T. T. *J. Appl. Phys.* **1968**, *39*, 3798.

(32)   Ok, K. M. C., E. O.; Halasyamani, P. S. *Chem. Soc. Rev.* **2006**, *35*, 710.

(33)   Lines, M. E. G., A. M. *Principles and Application of Ferroelectrics and Related Materials*; Oxford University Press: Oxford, UK, 1991.

(34)   Pepinsky, R.; Jona, F. *Phys. Rev.* **1957**, *105*, 344.

(35)   Abrahams, S. C.; Ravez, J.; Simon, A.; Chaminade, J. P. *J. Appl. Phys.* **1981**, *52*, 4740.

(36)   Schmid, H. *Magnetoelectric Interaction Phenomena in Crystals*; Kluwer: Dordrecht, 2004.

(37)   Spaldin, N. A.; Fiebig, M. *Science* **2005**, *309*, 391.

(38)   Khomskii, D. I. *Physics* **2009**, *2*, 20.

(39)   Keve, E. T.; Abrahams, S. C.; Bernstein, J. L. *J. Chem. Phys.* **1969**, *51*, 4928.

(40)   Keve, E. T.; Abrahams, S. C.; Bernstein, J. L. *J. Chem. Phys.* **1970**, *53*, 3279.

(41)   Bergman, J. G.; Crane, G. R.; Guggenheim, H. *J. Appl. Phys.* **1975**, *46*, 4645.

(42)   Asahi, T.; Tomizawa, M.; Kobayashi, J.; Kleemann, W. *Phys. Rev. B* **1992**, *45*, 1971.

(43)   Ravez, J.; Abrahams, S. C.; De, P. R. *J. Appl. Phys.* **1989**, *65*, 3987.

(44)   Ravez, J.; Abrahams, S. C.; Mercier, A. M.; Rabardel, L.; De Pape, R. *J. Appl. Phys.* **1990**, *67*, 2681.

(45)   Fabbrici, S.; Montanari, E.; Righi, L.; Calestani, G.; Migliori, A. *Chem. Mater* **2004**, *16*, 3007.

(46)    Blinc, R.; Tavcar, G.; Zemva, B.; Hanzel, D.; Cevc, P.; Filipic, C.; Levstik, A.; Jaglicic, Z.; Trontelj, Z.; Dalal, N.; Ramachandran, V.; Nellutla, S.; Scott, J. F. *J. Appl. Phys.* **2008**, *103*, 074114/1.

(47)    Mezzadri, F.; Fabbrici, S.; Montanari, E.; Righi, L.; Calestani, G.; Gilioli, E.; Bolzoni, F.; Migliori, A. *Phys. Rev. B: Condens. Matter Mater. Phys.* **2008**, *78*, 064111/1.

(48)    Blinc, R.; Tavčar, G.; Žemva, B.; Goreshnik, E.; Hanžel, D.; Cevc, P.; Potočnik, A.; Laguta, V.; Trontelj, Z.; Jagličič, Z.; Scott, J. F. *J. Appl. Phys.* **2009**, *106*.

(49)    Blinc, R.; Cevc, P.; Potočnik, A.; Žemva, B.; Goreshnik, E.; Hanžel, D.; Gregorovič, A.; Trontelj, Z.; Jagličič, Z.; Laguta, V.; Perović, M.; Dalal, N. S.; Scott, J. F. *J. Appl. Phys.* **2010**, *107*.

(50)    Mezzadri, F.; Calestani, G.; Pernechele, C.; Solzi, M.; Spina, G.; Cianchi, L.; Del, G. F.; Lantieri, M.; Buzzi, M.; Gilioli, E. *Phys. Rev. B: Condens. Matter Mater. Phys.* **2011**, *84*, 104418/1.

(51)    Ravez, J.; Arquis, S.; Grannec, J.; Simon, A.; Abrahams, S. C. *J. Appl. Phys.* **1987**, *62*, 4299.

(52)    Scott, J. F.; Blinc, R. *J. Phys. Condens Matter* **2011**, *23*, 113202.

(53)    Scott, J. F.; Blinc, R. *J. Phys. Condens Matter* **2011**, *23*, 299401.

(54)    Catalan, G.; Scott, J. F. *Adv. Mater. (Weinheim, Ger.)* **2009**, *21*, 2463.

(55)    Hill, N. A.; Rabe, K. M. *Phys. Rev. B: Condens. Matter Mater. Phys.* **1999**, *59*, 8759.

(56)    Shpanchenko, R. V.; Chernaya, V. V.; Tsirlin, A. A.; Chizhov, P. S.; Sklovsky, D. E.; Antipov, E. V.; Khlybov, E. P.; Pomjakushin, V.; Balagurov, A. M.; Medvedeva, J. E.; Kaul, E. E.; Geibel, C. *Chem. Mater.* **2004**, *16*, 3267.

(57)    van, d. B. J.; Khomskii, D. I. *J. Phys.: Condens. Matter* **2008**, *20*, 434217/1.

(58)    Khomskii, D. I. *J. Magn. Magn. Mater.* **2006**, *306*, 1.

(59)    Ikeda, N.; Ohsumi, H.; Ohwada, K.; Ishii, K.; Inami, T.; Kakurai, K.; Murakami, Y.; Yoshii, K.; Mori, S.; Horibe, Y.; Kito, H. *Nature (London, U. K.)* **2005**, *436*, 1136.

(60)    Yamauchi, K.; Picozzi, S. *Phys. Rev. Lett.* **2010**, *105*, 107202/1.

(61)    Van Aken, B. B.; Palstra, T. T. M.; Filippetti, A.; Spaldin, N. A. *Nat. Mater.* **2004**, *3*, 164.

(62)    Kimura, T.; Goto, T.; Shintani, H.; Ishizaka, K.; Arima, T.; Tokura, Y. *Nature (London, U. K.)* **2003**, *426*, 55.

(63)    Hur, N.; Park, S.; Sharma, P. A.; Ahn, J. S.; Guha, S.; Cheong, S. W. *Nature (London, U. K.)* **2004**, *429*, 392.

(64)    Kimura, T. *Annu. Rev. Mater. Res.* **2007**, *37*, 387.

(65)    Heyer, O.; Hollmann, N.; Klassen, I.; Jodlauk, S.; Bohaty, L.; Becker, P.; Mydosh, J. A.; Lorenz, T.; Khomskii, D. *J. Phys.: Condens. Matter* **2006**, *18*, L471.

(66)    Wu, H.; Burnus, T.; Hu, Z.; Martin, C.; Maignan, A.; Cezar, J. C.; Tanaka, A.; Brookes, N. B.; Khomskii, D. I.; Tjeng, L. H. *Phys. Rev. Lett.* **2009**, *102*, 026404/1.

(67)    Brown, I. D.; Altermatt, D. *Acta Cryst.* **1985**, *B41*, 244.

(68)    Brese, N. E.; O'Keeffe, M. *Acta Cryst.* **1991**, *B47*, 192.

(69)    Brown, I. D. *The Chemical Bond in Inorganic Chemistry - The Bond Valence Model. IUCr monographs on Crystallography 12*; Oxford University Press, 2002.

## CHAPTER 2. Experimental Section

### 2.1 Synthesis

Hydrothermal methods were used to synthesize either polycrystalline samples or crystals.[1] In order to perform the exploratory synthesis in a more systematic and convenient way, the triangle method was applied to optimize the reaction conditions (see figure 2.1). The triangle method helps to choose the ratio of each starting material. The optimized starting materials were combined with 5 ml of $H_2O$ with 2 - 5 ml $CF_3COOH$ in a 23 ml Teflon-lined autoclave. The autoclaves were subsequently closed, gradually heated to 230 °C, held for 24 h, and cooled slowly to room temperature at a rate of 6 °C $h^{-1}$. The mother liquor was decanted, and the products were recovered by filtration using excess distilled water and acetone.[2] In order to remove impurities, washing with hot water, sonication, or hand-sorting were applied.
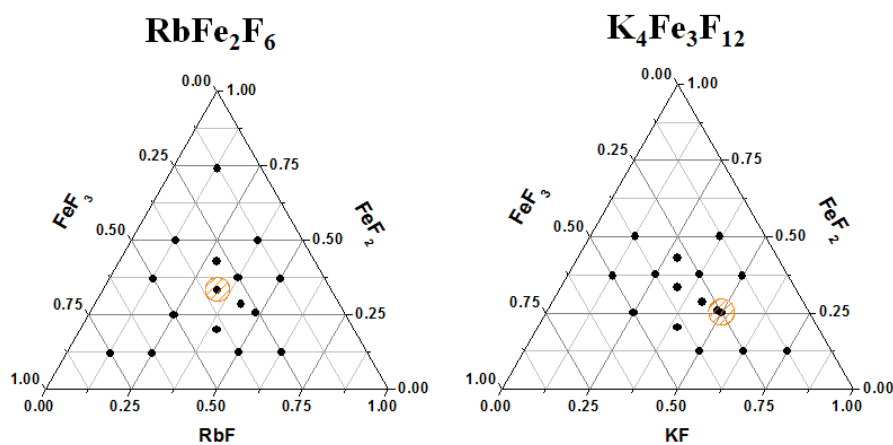


**Figure 2.1** Example of synthesis of RbFe$_2$F$_6$ and K$_4$Fe$_3$F$_{12}$ using triangle method. (the region of orange circle is optimized reaction condition)

25

## 2.2 Characterization

The crystal structures of the materials in this dissertation were characterized by single-crystal X-ray diffraction, and their bulk phases were confirmed by powder X-ray diffraction. For $RbFe_2F_6$ in chapter 3, the variable-temperature powder neutron diffraction (4-300 K) was also performed. As spectroscopic tools, infrared and UV-vis diffuse reflectance spectroscopy were utilized to characterize vibrational modes of functional groups and band gaps of the materials, respectively.[3-7] In addition, thermal analysis such as thermogravimetric analysis (TGA), or differential thermal analysis (DTA) was used to characterize the thermal behaviors of the materials. For $RbFe_2F_6$ and $K_4Fe_3F_{12}$ in chapter 3 and 4, [57]Fe-Mössbauer Spectroscopy was used to characterize the ratio of $Fe^{2+}$ and $Fe^{3+}$.[8]

## 2.2.1 Single crystal X-ray diffraction

For $RbFe_2F_6$ in chapter 3, a brown colored rod shaped crystal ($0.02 \times 0.02 \times 0.1$ mm$^3$), for $K_4Fe_3F_{12}$ in chapter 4, a brownish yellow colored hexagonal plate shaped crystal ($0.04 \times 0.03 \times 0.01$ mm$^3$), for $Ba_3Mn_3F_{14}$ in chapter 5, a light brown colored rod-shaped crystal ($0.02 \times 0.03 \times 0.1$ mm$^3$), for $NaBa_7Mn_7F_{34}$ in chapter 5, a dark brown colored plate-shaped crystal ($0.2 \times 0.1 \times 0.02$ mm$^3$), and for $CrF_3 \cdot 0.5H_2O$ in chapter 6, a dark green colored octahedral crystal ($0.04 \times 0.04 \times 0.07$ mm$^3$) was selected for single crystal data collection. Data were collected using a Siemens SMART diffractometer equipped with a 1K CCD area detector using graphite-monochromated Mo Kα radiation. A hemisphere of data was collected using a narrow-frame method with scan widths of 0.30°

in omega and an exposure time of 40 - 45 s per frame. The data were integrated using the Siemens SAINT program,[9] with the intensities corrected for Lorentz polarization, air absorption, and absorption attributable to the variation in the path length through the detector faceplate. Psi-scans were used for the absorption correction on the hemisphere of data. All of the data were solved by direct methods using SHELXS-97 (or SHELX-2013) and refined using SHELXL-97 (or SHELX-2013).[9-12] All of the atoms were refined with anisotropic thermal parameters except F(9a), F(9b), F(10a) and F(10b) in $NaBa_7Mn_7F_{34}$ in chapter 5 and converged for $I > 2\sigma(I)$. All calculations were performed using the WinGX-98 crystallographic software package.[13] For $CrF_3 \cdot 0.5H_2O$ in chapter 6, during the first refinement, the position of water molecules, Ow (8b site) seemed to be disordered attributable to its anisotropic thermal parameter, thus tried to refine the disorder position. After several refinement, successfully water molecules, Ow were located in 32e sites, which have one fourth occupancy. The structural figures for $RbFe_2F_6$, $K_4Fe_3F_{12}$, $Ba_3Mn_3F_{14,}$ $NaBa_7Mn_7F_{34}$, and $CrF_3 \cdot 0.5H_2O$ were drawn using the VESTA crystal structure drawing package.[14]

## 2.2.2 Powder X-ray diffraction

Powder X-ray diffraction (PXRD) data of the materials were collected using a PANalytical X'Pert PRO diffractometer operating with Cu-Kα radiation. The data were taken in the 2θ range of 5 - 70° with a step size of 0.008° and a fixed time of 0.3 s. The purity of the samples was confirmed by comparing the experimental and calculated powder patterns.

### 2.2.3 Neutron diffraction

Powder neutron diffraction of $RbFe_2F_6$ in Chapter 3 was performed by Dr. Mark A. Green at University of Kent, UK on the BT1 high resolution diffractometer at the NIST Center for Neutron research. Data were collected using a Ge (311) monochromator at $\lambda$ = 2.0782 Å and a (311) monochromator at $\lambda$ = 1.5401 Å, with an in-pile collimation of 15`. Rietveld refinements were performed by Dr. Mark A. Green using the FULLPROF suite of programs.[15] Cooling was performed with a closed cycle refrigerator and measurements were performed at 4, 10, 25, 50, 100, 150, 200, 250 and 300 K.

### 2.2.4 Thermal analysis

Thermogravimetric analysis (TGA), and differential thermal analysis (DTA) were carried out on a EXSTAR TG/DTA 6300 series (SII Nano Technology Inc.). Approximately 10 mg of the samples were placed into a platinum crucible and heated under nitrogen at a rate of 10 °C min$^{-1}$ to 900 °C.

### 2.2.5 Infrared spectroscopy

Infrared spectra were recorded on a Matteson FT-IR 5000 spectrometer or a PerkinElmer Spectrum 100 FT-IR spectrometer in the 400 - 4000 cm$^{-1}$ range. The samples were pressed with KBr chemical of spectroscopic grade. Infrared spectra were used to confirm the identifications of specific stretching or bending modes for materials.[7]

### 2.2.6 UV-vis diffuse reflectance spectroscopy

UV-vis diffuse reflectance spectra in Chapter 3 and 4 were collected on a Varian Cary 500 scan UV-vis-NIR spectrophotometer over the spectral range 200-2000 nm at room temperature. Poly-(tetrafluoroethylene) was used as a reference material. UV-vis Diffuse reflectance spectra in chapter 5 and 6 were obtained by Prof. Hans-Conrad zur Loye and Dr. Jeongho Yeon at University of South Carolina using a Perkin-Elmer Lambda 35 UV-Vis scanning spectrophotometer equipped with an integrating sphere in the range 200-900 nm. Reflectance spectra were converted to absorbance with the Kubelka-Munk function.[3-5]

### 2.2.7 $^{57}$Fe-Mössbauer Spectroscopy

$^{57}$Fe-Mössbauer spectra and parameter of $RbFe_2F_6$ and $K_4Fe_3F_{12}$ in Chapter 3 and Chapter 4 were obtained by Dr. Peter Solheid at University of Minnesota using a Ranger Scientific Mössbauer Spectrometer at R.T.

### 2.2.8 Magnetic property measurements

Magnetic property measurements for $RbFe_2F_6$ and $K_4Fe_3F_{12}$ in Chapter 3 and Chapter 4 were performed by Dr. Chris Leighton at University of Minnesota. DC magnetometry measurements were performed in helium gas in a commercial SQUID (Superconducting Quantum Interference Device) magnetometer (Quantum Design) at temperatures from 2.0 to 300 K, in applied magnetic fields up to 70 kOe. Magnetic property measurements in Chapter 5 and 6 were performed by Dr. Elise Pachoud and Joshua Tapp at University

of Houston on Quantum Design Physical Property Measurement System (PPMS) as a function of temperature from 2.0 to 300 K.

## 2.3 References

(1)     Byrappa, K. Y., M. *Handbook of Hydrothermal Technology: Technology for Crystal Growth and Materials Processing.* ; Noyes Publications /William Andrew Publishing, LLC, 2001.

(2)     Kim, S. W.; Chang, H. Y.; Halasyamani, P. S. *J. Am. Chem. Soc.* **2010**, *132*, 17684.

(3)     Kubelka, P. M.; Munk, F. Z. *Tech. Phys.* **1931**, *12*, 593.

(4)     Tauc, J.; Grigorovici, R.; Vancu, A. *physica status solidi (b)* **1966**, *15*, 627.

(5)     Tauc, J. *Mater. Res. Bull.* **1970**, *5*, 721.

(6)     Lever, A. B. P. *Inorganic Electronic Spectroscopy, 2nd ed.*; Elsevier Science Publishers B. V.: Amsterdam, 1984.

(7)     Nakamoto, K. *Infrared and Raman Spectra of Inorganic and Coordination Compounds Part A: Theory and Applications in Inorganic Chemistry*; 5th ed.; John Wiley & Sons, Inc: New York, 1997.

(8)     Long, G. J.; Grandjean, F. *Mössbauer Spectroscopy Applied to Magnetism and Materials Science.*; Plenum Press: New York, 1993.

(9)     *SAINT, Program for Area Detector Absorption Correction, 4.05*; Siemens Analytical X-ray Systems: Madison, WI, 1995.

(10)    Sheldrick, G. M. *SHELXS-97, A program for automatic solution of crystal structures*; University of Goettingen: Goettingen, Germany, 1997.

(11)    Sheldrick, G. M. *SHELXS-97, A program for Crystal Structure Refinement*; University of Goettingen: Goettingen, Germany, 1997.

(12)     Sheldrick, G. *Acta Cryst.* **2008**, *A64*, 112.

(13)     Farrugia, L. *J. Appl. Cryst.* **1999**, *32*, 837.

(14)     Momma, K.; Izumi, F. *J. Appl. Cryst.* **2008**, *41*, 653.

(15)     Rodriguez-Carvajal, J. *Physica B (Amsterdam)* **1993**, *192*, 55.

# CHAPTER 3. $RbFe^{2+}Fe^{3+}F_6$: Synthesis, Structure, and Characterization of a New Charge-ordered Magnetically Frustrated Pyrochlore-related Mixed-metal Fluoride

## 3.1 Abstract

A new charge-ordered magnetically frustrated mixed-metal fluoride with a pyrochlore-related structure has been synthesized and characterized. The material, $RbFe_2F_6$ ($RbFe^{2+}Fe^{3+}F_6$) was synthesized through mild hydrothermal conditions. The material exhibits a three-dimensional pyrochlore-related structure consisting of corner-shared $Fe^{2+}F_6$ and $Fe^{3+}F_6$ octahedra. In addition to single-crystal diffraction data, neutron powder diffraction and magnetometry measurements were carried out. Magnetic data clearly reveal strong anti-ferromagnetic interactions (a Curie–Weiss temperature of -270 K) but sufficient frustration to prevent ordering until 16 K. No structural phase transformation is detected from the variable-temperature neutron diffraction data. Infrared, UV-vis, $^{57}Fe$-Mössbauer, thermogravimetric, and differential thermal analysis measurements were also performed. Crystal data: $RbFe_2F_6$, orthorhombic space group *Pnma* (No. 62), $a = 7.0177(6)$, $b = 7.4499(6)$, $c = 10.1765(8)$ Å, $V = 532.04(8)$ Å$^3$, $Z = 4$, $T = 296(2)$ K.

## 3.2 Introduction

Mixed-metal fluorides are of topical interest attributable to their varied functional properties.[1] These include multiferroic behavior ($BaNiF_4^{2-4}$ and $Pb_5Cr_3F_{19}^5$), magnetic frustration ($Na_2NiFeF_7^6$ and $MnCrF_5^7$), ferroelectricity ($K_3Fe_5F_{15}^{8-9}$ and $SrAlF_5^{10}$), and non-linear optical behavior ($BaMgF_4$).[11] Recently, attention has been paid to the multiferroic $K_3Fe_5F_{15}$ and related materials such as $K_3Cu_3Fe_2F_{15}^{12}$ and $K_3Cr_2Fe_3F_{15}$,[13] as well as multiferroic fluorides as a whole.[14-15] $K_3Fe_5F_{15}$ and $K_3Cu_3Fe_2F_{15}$ have been shown to be ferri- and anti-ferromagnetic respectively, whereas $K_3Cr_2Fe_3F_{15}$ exhibits relaxor-like magnetic transitions. Although full structural data is lacking for the quaternary phases, multiferroic behavior is suggested.[12-13] It should also be noted that in $K_3Cu_3Fe_2F_{15}$ and $K_3Cr_2Fe_3F_{15}$, the $Cu^{2+}/Fe^{3+}$ and $Cr^{3+}/Fe^{2+}$ cations, respectively, are crystallographically disordered.

With respect to $AM^{2+}M^{3+}F_6$ materials (A = alkali metal or $NH_4$; $M^{2+}$ = Mg, Mn, Fe, Co, Ni, Cu; $M^{3+}$ = Al, Ga, V, Cr, Fe) a host of materials have been reported,[16-17] although well-determined crystal structures are lacking for many. Structure types for the $AM^{2+}M^{3+}F_6$ materials include trirutile ($LiM^{2+}M^{3+}F_6$),[18] modified pyrochlore (($NH_4)Fe^{2+}Fe^{3+}F_6$),[19] tetragonal ($K_{0.6}Fe^{2+}_{0.6}Fe^{3+}_{0.4}F_3$), and hexagonal ($K_{0.6}Nb_2F_6$) bronzes,[20] and materials isostructural to trigonal $Na_2SiF_6$ ($LiMnGaF_6$).[21]

In these materials, both disorder and order are observed between the $M^{2+}$ and $M^{3+}$ cations. With the pyrochlore related materials, crystallographic disorder, of the $M^{2+}$ and $M^{3+}$ cations on the octahedral sites is observed. This disorder results in spin-glass behavior in $CsMnFeF_6$.[22-23] Ordering of the $M^{2+}$ and $M^{3+}$ cations has been observed, with

a lowering of crystallographic symmetry, in the trirutile $LiFe^{2+}Fe^{3+}F_6$,[18] the fluorobronze $K_{0.6}Fe^{2+}_{0.6}Fe^{3+}_{0.4}F_3$,[24-26] and the pyrochlore-related $(NH_4)Fe^{2+}Fe^{3+}F_6$.[19] Antiferromagnetic behavior has been observed with the $Li^+$ and $NH_4^+$ phases.[18,27] In addition to the aforementioned magnetic behavior, magnetic frustration has been observed in a variety of mixed-metal fluorides.[1] Such frustration can occur not only when the two metal cationic species, $M^{2+}$ and $M^{3+}$, crystallographically order, but also if they are arranged in some form of triangular structural topology, i.e. in the presence of geometric frustration. Magnetically frustrated fluorides include the hexagonal tungsten bronze–$FeF_3$,[28] $Na_2NiFeF_7$,[6] $MnCrF_5$,[7] $Fe_3F_8 \cdot 2H_2O$,[29-30] and $NH_4Fe_2F_6$.[27] In this chapter, we report on the synthesis, structure (X-ray and variable-temperature neutron diffraction), and characterization of $RbFe_2F_6$ ($RbFe^{2+}Fe^{3+}F_6$). This new material represents an example of a charge-ordered pyrochlore-related mixed-metal fluoride that exhibits strong magnetic frustration. In addition to the synthesis and structural characterization, magnetic measurements are performed. These measurements and calculations enable us to develop and understand a variety of important structure–property relationships.

## 3.3 Experimental section

### 3.3.1 Reagents

RbF (Alfa Aesar, 99.7%), $FeF_2$ (Alfa Aesar, 99%), $FeF_3$ (Alfa Aesar, 97%), and $CF_3COOH$ (Alfa Aesar, 99%) were used without any further purification.

### 3.3.2 Synthesis

$RbFe_2F_6$ was obtained by hydrothermal methods using a diluted $CF_3COOH$ solution. 0.119 g ($1.14 \times 10^{-3}$ mol) of RbF, 0.107 g ($1.14 \times 10^{-3}$ mol) of $FeF_2$, 0.129 g ($1.14 \times 10^{-3}$ mol) of $FeF_3$, 3 ml ($3.90 \times 10^{-2}$ mol) of $CF_3COOH$, and 5 ml of $H_2O$ were combined in a 23-mL Teflon-lined stainless steel autoclave. The autoclave was closed, gradually heated to 230 ºC, held for 24 h, and cooled slowly to room temperature at a rate 6 ºC $h^{-1}$. The mother liquor was decanted from the only solid product, brown colored rod shaped crystals of $RbFe_2F_6$, was recovered by filtration and washed with distilled water and acetone. The yield was ~40 % on the basis of $FeF_3$. Powder X-ray diffraction patterns on the synthesized phase are in good agreement with the generated pattern from the single-crystal data.

### 3.4 Results and Discussion

**Synthesis.** Previously reported and related materials, e.g., $NH_4Fe_2F_6$, $NH_4MnFeF_6$, $NH_4MnCrF_6$ and $RbMnFeF_6$,[19,31] were synthesized by using the binary metal fluorides mixed with the alkali metal fluoride or $NH_4F$ solutions in a platinum tube. The tube was sealed, placed in an autoclave, and heated to temperatures above 350 °C that resulted in pressures in excess of 2000 bar. We were able to synthesize $RbFe_2F_6$ through a low-temperature and mild hydrothermal technique. In our method, the binary metal fluorides are combined with RbF and a dilute $CF_3COOH$ aqueous solution. We have previously demonstrated that this method can be used to synthesize phase-pure and polycrystalline $BaMF_4$ (M = Mg, Mn, Co, Ni and Zn).[32]
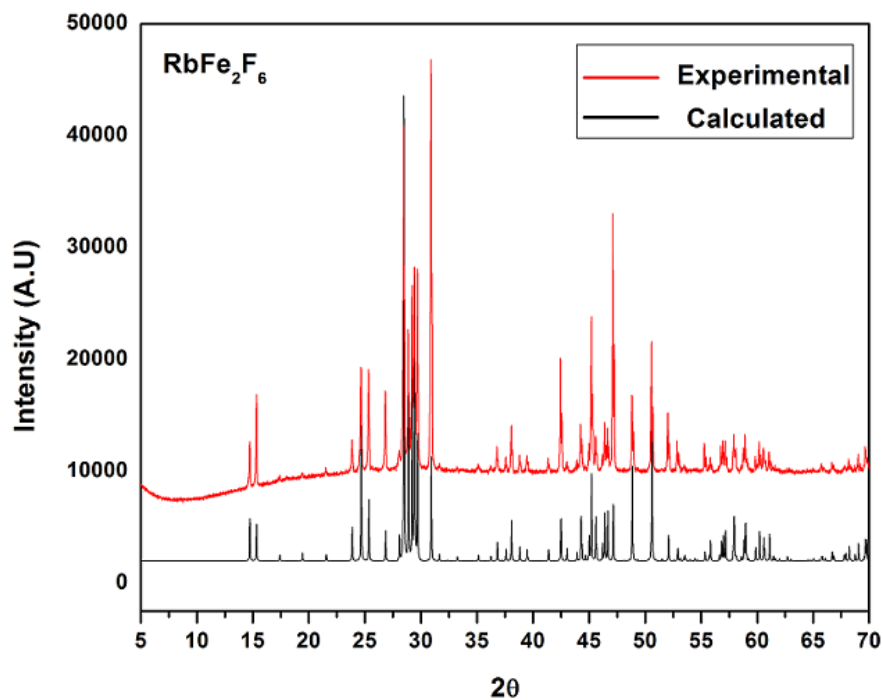
**Figure 3.1** Experimental and calculated powder X-ray diffraction patterns for $RbFe_2F_6$.

**Structure.** $RbFe_2F_6$ crystallizes in the *Pnma* space group with lattice parameters of $a = 7.02134(7)$, $b = 7.45093(7)$, and $c = 10.1795(1)$ Å at room temperature. This represents a reduced orthorhombic cell of the conventional β-pyrochlore lattice with *Fd-3m* symmetry. The β-pyrochlore is related to the more common α-pyrochlore lattice, with the general formula $A_2B_2X_6X$`, through two ordered vacancies. First, one of the two A cations is vacant, which reverts the Kagome network of the A sites in a-pyrochlore into a diamond lattice with $T_d$ point symmetry. Second, the anion, X`, that does not contribute to the $BX_6$ octahedra is vacant; removing this apical anion reduces the eight-coordination of the A cation and leaves an open cage site.

RbFe$_2$F$_6$ exhibits a three-dimensional crystal structure consisting of corner-shared FeF$_6$ octahedra that are separated by Rb$^+$ cations (see Figure. 3.1). The formula may be more descriptively written as RbFe$^{2+}$Fe$^{3+}$F$_6$, as the Fe$^{2+}$ and Fe$^{3+}$ cations are ordered in the structure. The structure of RbFe$_2$F$_6$ may be described as being built up from two connected FeF$_6$ octahedral sub-lattices.

Ball-and-stick representations of RbFe$_2$F$_6$ are shown in Figure 3.2. The *bc*-plane of the structure is shown in Figure 3.2a, and, as can be seen, chains of Fe$^{3+}$F$_6$ octahedra share corners along the *b*-axis direction. These Fe$^{3+}$F$_6$ chains are connected through Fe$^{2+}$F$_6$ octahedra along the *c*-axis direction. The *ac*-plane of the structure is shown in Figure 3.2b. Similarly, chains of Fe$^{2+}$F$_6$ octahedra share corners along the a-axis direction, and these chains are connected through Fe$^{3+}$F$_6$ octahedra along the *c*-axis direction. This octahedral connectivity results in Kagome type nets in both the *bc*- and *ac*-planes of the structure (see Figure. 3.1a and 3.1b). The Fe$^{2+}$–F (Fe$^{3+}$–F) bond distances are in the range 1.961(2)–2.1368(13) Å (1.9098(14)–1.9488(6) Å). The Rb$^+$ cation is in a 10-fold coordinated environment, with Rb–F distances in the range 2.931(2)–3.2477(14) Å. In connectivity terms, the structure may be written as ((Fe(II)F$_{6/2}$)$^-$(Fe(III)F$_{6/2}$)$^0$)$^-$ where charge balance is maintained by a Rb$^+$ cation. Bond valence calculations[33-35] (see Table 4) result in values of 0.821, 1.93, 3.03 and 0.935–0.996 for Rb$^+$, Fe$^{2+}$, Fe$^{3+}$ and F$^-$, respectively.
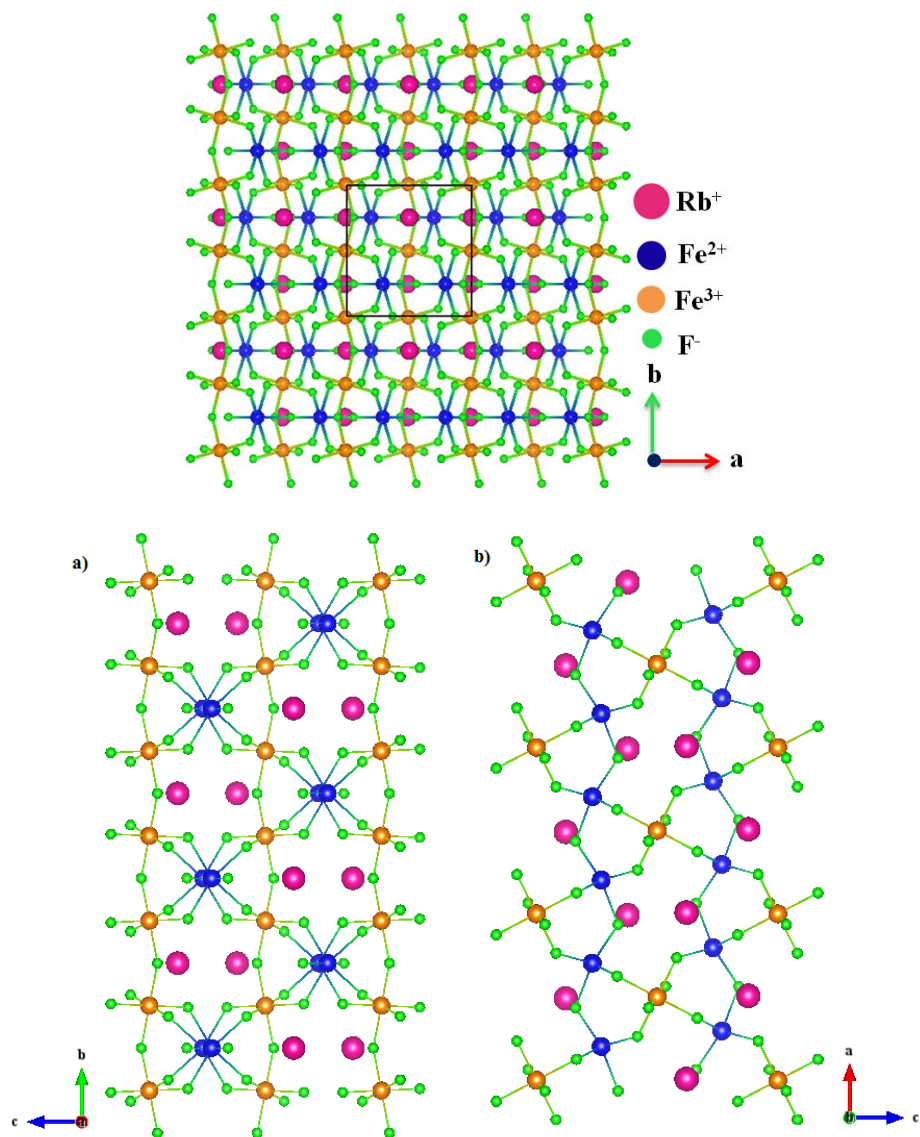
**Figure 3.2** Ball-and-stick representation of RbFe$_2$F$_6$ in the *ab*-plane (top): a) *bc*-plane and b) *ac*-plane (bottom).

**Rb(1)**



**Fe(1)**



**Fe(2)**
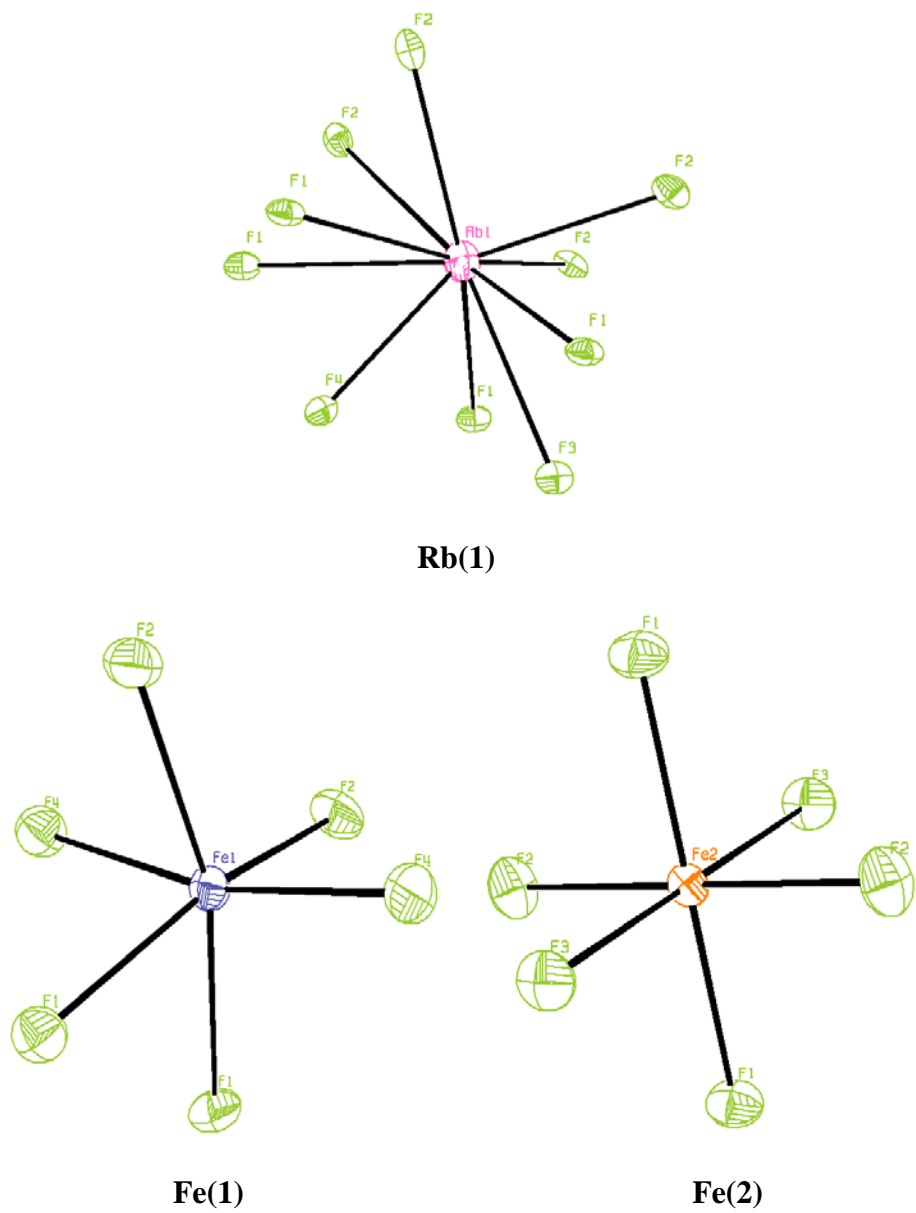
**Figure 3.3** ORTEP (50% probability ellipsoids) diagrams for $RbFe_2F_6$.

**Neutron Diffraction.** Powder neutron diffraction measurements were performed on

$RbFe_2F_6$ at several temperatures in the range 4–300 K. Figure 3.4 shows the typical

quality of fit to the observed data with this model, as obtained at 300 K, resulting in

goodness-of-fit factors of $wR_p$ = 4.49 and $\chi^2$ = 1.29. One key feature of β-pyrochlores

that has greatly hindered their usefulness as model magnetic systems is their tendency

for both site disorder and partial occupancy. To evaluate these possibilities a number of

models were tested and no evidence could be found for such issues in $RbFe_2F_6$; varying

the occupancy of Rb from the ideal value of 1.0 gave a refined value of 0.99(1) and, as

this made no improvement to the goodness-of-fit factors, this parameter was fixed in all

subsequent refinements.
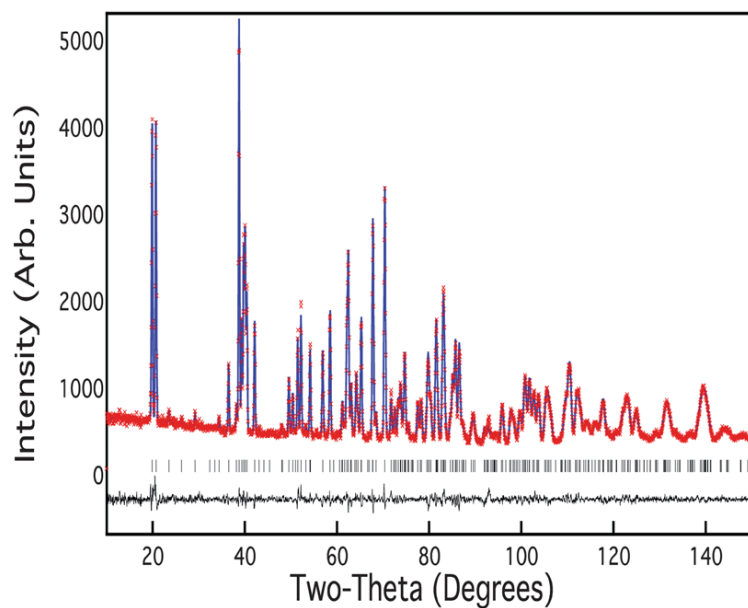


**Figure 3.4** Observed (red), and calculated (blue) and difference (black) data obtained

from Rietveld refinements of neutron diffraction data of $RbFe_2F_6$ at 300 K.

Figure 3.5 shows the lattice parameters from the variable-temperature neutron diffraction data. All three lattice parameters show a modest contraction down to the magnetic ordering temperature, below which there is negative thermal expansion, particularly within the ab-plane. This is confirmed through the increase in volume, as shown in the inset to Figure 3.5b. No structural phase transition was found on cooling, and $RbFe_2F_6$ remained orthorhombic with *Pnma* symmetry to the lowest temperature measured. One central structural feature was the difference between thermal factors of the constituent elements.
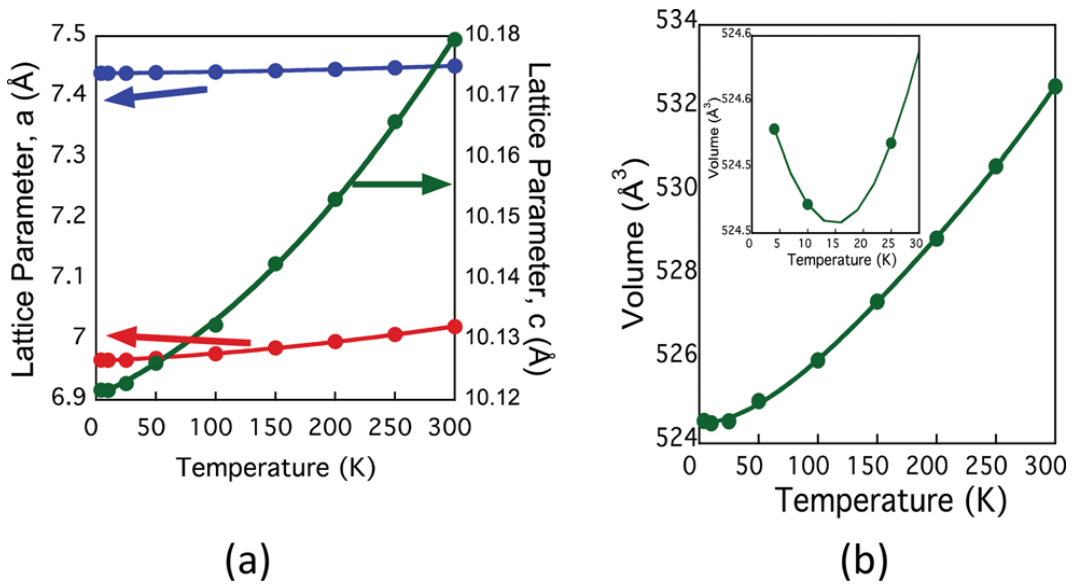


**Figure 3.5** Panel (a) shows the lattice parameter as a function of temperature; there is a contraction in all three directions upon cooling, until the magnetic ordering temperature when $RbFe_2F_6$ shows negative thermal expansion in *a*, *b* and *c*, best visualized by panel (b) which shows the overall increase in volume.

Figure 3.6 shows the isotropic thermal factor, U, for all six atoms as a function of temperature. Although each atom has a typical temperature dependence, the absolute value of U for Rb is ~ 5 times that of the lighter Fe, and even twice that of the F that is over four times lighter. The rattling effect of A site cations within the $\beta$-pyrochlores is well documented and results from a gross mismatch between the ionic radii of the cations and the available space.
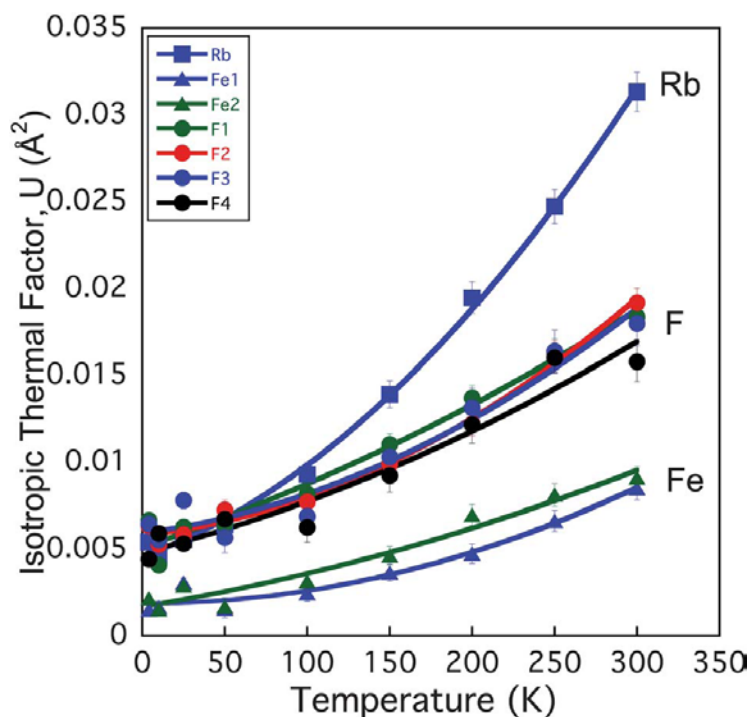


**Figure 3.6** Isotropic thermal factors of $RbFe_2F_6$ as functions of temperature as obtained from Rietveld refinement of powder neutron diffraction data showing the extraordinarily large thermal factor of Rb as a result of the mismatch between Rb ionic size and the open cage site that it occupies.

The magnetic structure was determined from powder neutron diffraction data collected at 4 K on the BT1 diffractometer at NIST. The new magnetic reflections that appeared below $T_N$ could all be indexed with a k = (0 0 0) propagation vector. The atomic positions of the final refinements are given in Table 5 and the observed, calculated and difference plots are shown in Figure 3.7. The magnetic structure is shown in Figure 3.8. Fe(1) with a magnetic moment of 3.99(5) μB is confined to the *b* axis, but can be described as forming anti-ferromagnetic chains along the *a*-axis. These chains are orthogonal to those on Fe(2). The second Fe moment at (0.5 0 0.5) has a slightly larger magnitude of 4.29(5) μB, consistent with its $Fe^{3+}$ oxidation state, and resides along the *a*-axis forming anti-ferromagnetic chains parallel to the *b*-axis. The refined moments are all smaller than the theoretical spin-only contribution to the magnetic moment, but this is consistent with the observed diffuse scattering that is present even at 4 K, resulting from the magnetic frustration, suggesting that not all of the moments become long-range ordered.
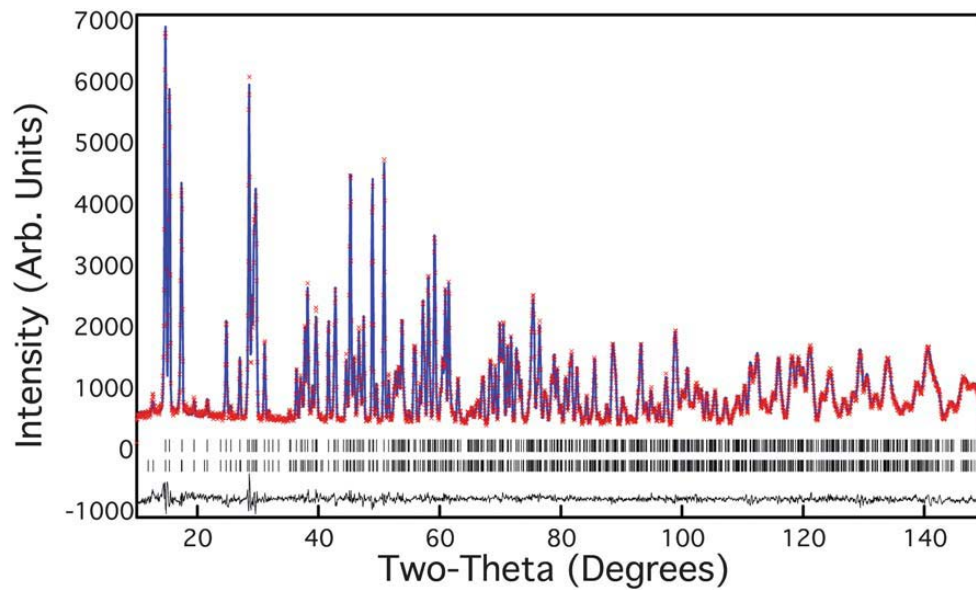
**Figure 3.7** Observed (red), calculated (blue) and difference (black) data obtained from Rietveld refinements of neutron diffraction data of $RbFe_2F_6$ at 4 K. The upper tickmarks represent those associated with the nuclear structure while those below correspond to the magnetic structure refinement.
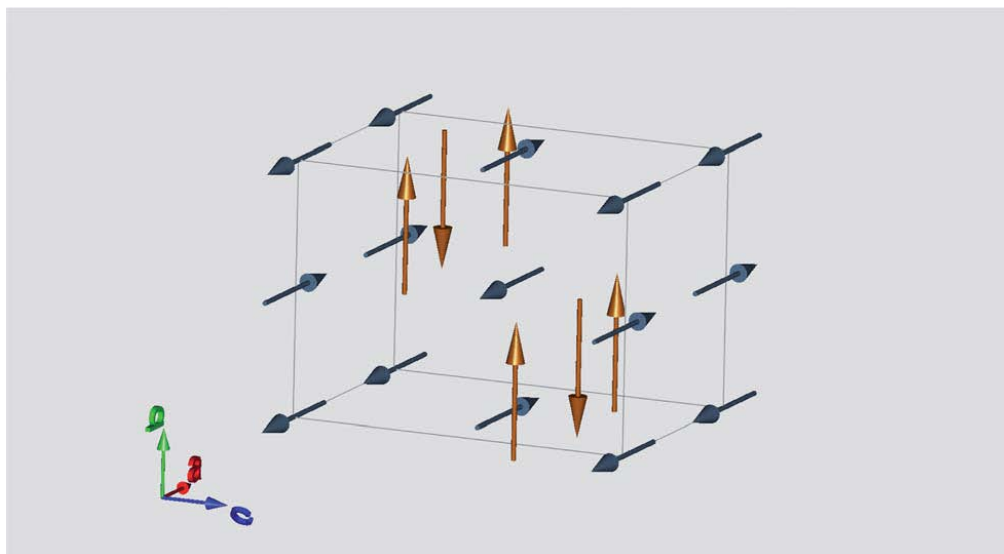
**Figure 3.8** Magnetic structure of $RbFe_2F_6$ at 4 K as determined from Rietveld refinement of powder neutron diffraction data. The magnetic structure has a (0 0 0) propagation vector with the Fe(1) moment (gold) aligned along the *b* axis forming antiferromagnetic chains down *a*, whereas the Fe(2) moments (blue) align along the *a* axis and form antiferromagnetic chains along the *b*.

**Infrared spectroscopy.** The FT-IR spectra of $RbFe_2F_6$ revealed Fe–F vibrations between 1000 and 400 $cm^{-1}$ (See Figure 3.9). The bands occurring between 750–700 $cm^{-1}$ and 530–400 $cm^{-1}$ can be assigned to Fe–F and Fe–F–Fe vibrations, respectively. These assignments are consistent with previous reports.[36-39]
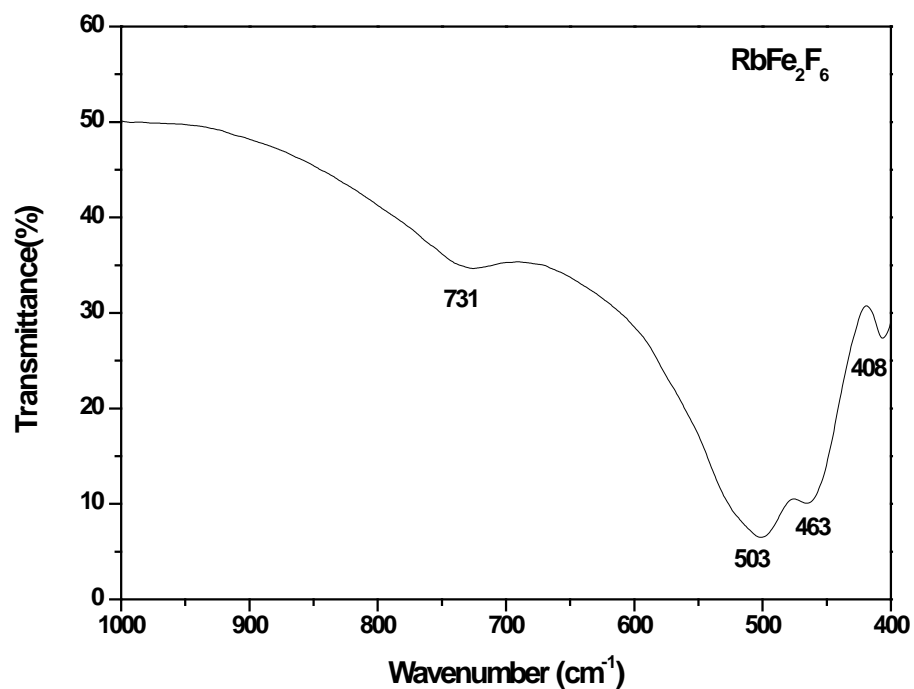
$RbFe_2F_6$

| $\upsilon(Fe-F)$ | $\upsilon(Fe-F-Fe)$ |
| --- | --- |
| 731 | 503 |
| | 463 |
| | 408 |

**Figure 3.9** Infrared spectrum and assignment for $RbFe_2F_6$.[36-39]

**UV-Visible diffuse reflectance spectroscopy.** The UV-vis diffuse reflectance spectra

indicate that the absorption energy for $RbFe_2F_6$ is approximately 1.9 eV, consistent with

the brown color of the material. Absorption (K/S) data were calculated through the Kubelka–Munk function[40]:

$$F(R) = \frac{(1-R)^2}{2R} = \frac{K}{S}$$

where $R$ represents the reflectance, $K$ the absorption, and $S$ the scattering. In a $K/S$ versus $E(eV)$ plot, extrapolating the linear part of the rising curve to zero provides the onset of absorption at 1.9 eV. Three bands in the region of 1.5 – 3.3 eV were attributed to d-d transitions of Fe, the other large broad bands in the region of 3.5 – 5.0 eV were attributed to metal to ligand charge transfer (See figure 3.10).[41]
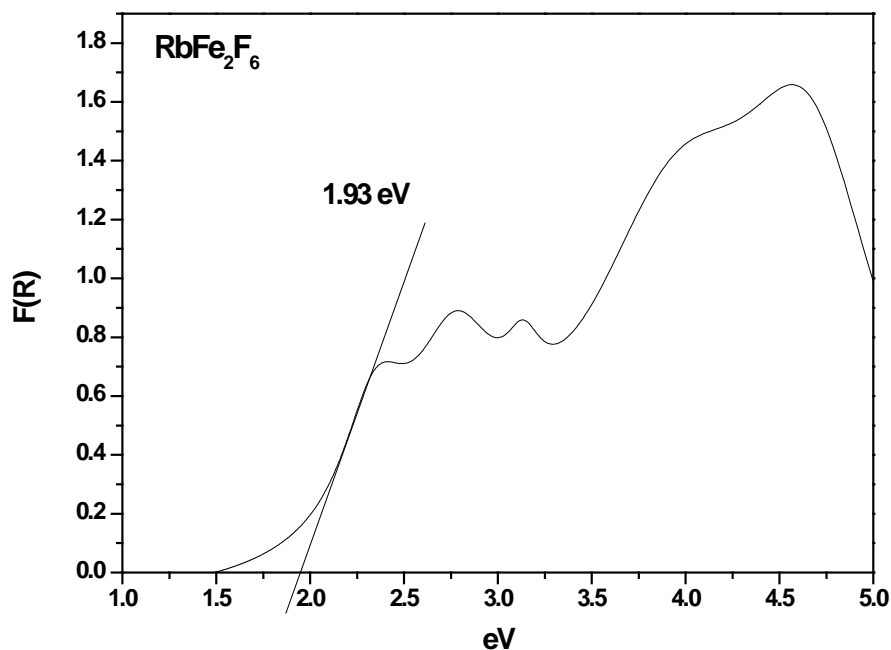


**Figure 3.10** UV-vis diffuse reflectance data for $RbFe_2F_6$.

**[57]Fe-Mössbauer Spectroscopy.** The Mössbauer spectra of $RbFe_2F_6$ at R.T showed two doublets, which indicated the isomer shift and quadruple splitting of $Fe^{2+}$ and $Fe^{3+}$, respectively (See figure 3.11). The isomer shift (1.315 mm/s) and quadruple splitting (2.664 mm/s) observed for $Fe^{2+}$ and the isomer shift (0.474 mm/s) and quadruple splitting (0.720 mm/s) observed for $Fe^{3+}$ revealed the octahedral coordination of $Fe^{2+}$ and $Fe^{3+}$ sites,[42] respectively. The ratio of $Fe^{2+}$ to $Fe^{3+}$ is the same with respect to the peak areas of the spectra. The Mössbauer parameters of $RbFe_2F_6$ are quite similar to reported values for iron fluoride compounds,[24,43-45] in particular, to the mixed valence iron fluoride compounds, $NH_4Fe_2F_6$ and $CsFe_2F_6$ (See table 3.6 ).

**Thermal Analysis.** The thermal behavior of $RbFe_2F_6$ was investigated using thermogravimetric analysis (TGA) and differential thermal analysis (DTA) under a $N_2$ atmosphere (See Figure 3.12). The decomposition started around 350 °C and an additional step was also observed at around 600 °C, which is likely attributable to the loss of fluorides. The DTA also showed two endothermic peaks at ~450 and ~750 °C, which indicate decomposition. The final residue products, $RbFeF_3$ and $FeF_2$, were confirmed by PXRD.
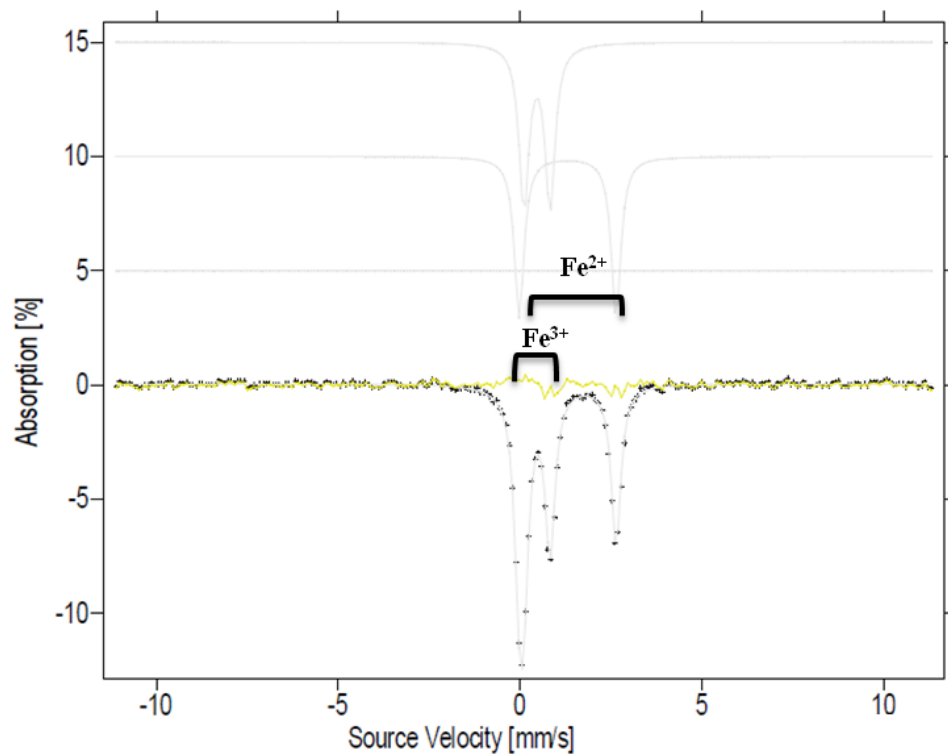
| RbFe$_2$F$_6$ | | | |
|---|---|---|---|
| **Fe** | **I.S.(mm/s) (±0.01)** | **Q.S.(mm/s) (±0.01)** | **Area (%) (±2)** |
| Fe$^{2+}$ | 1.315 | 2.664 | 49 |
| Fe$^{3+}$ | 0.474 | 0.720 | 51 |

**Figure 3.11** Mössbauer Spectra and parameter of RbFe$_2$F$_6$ at R.T.
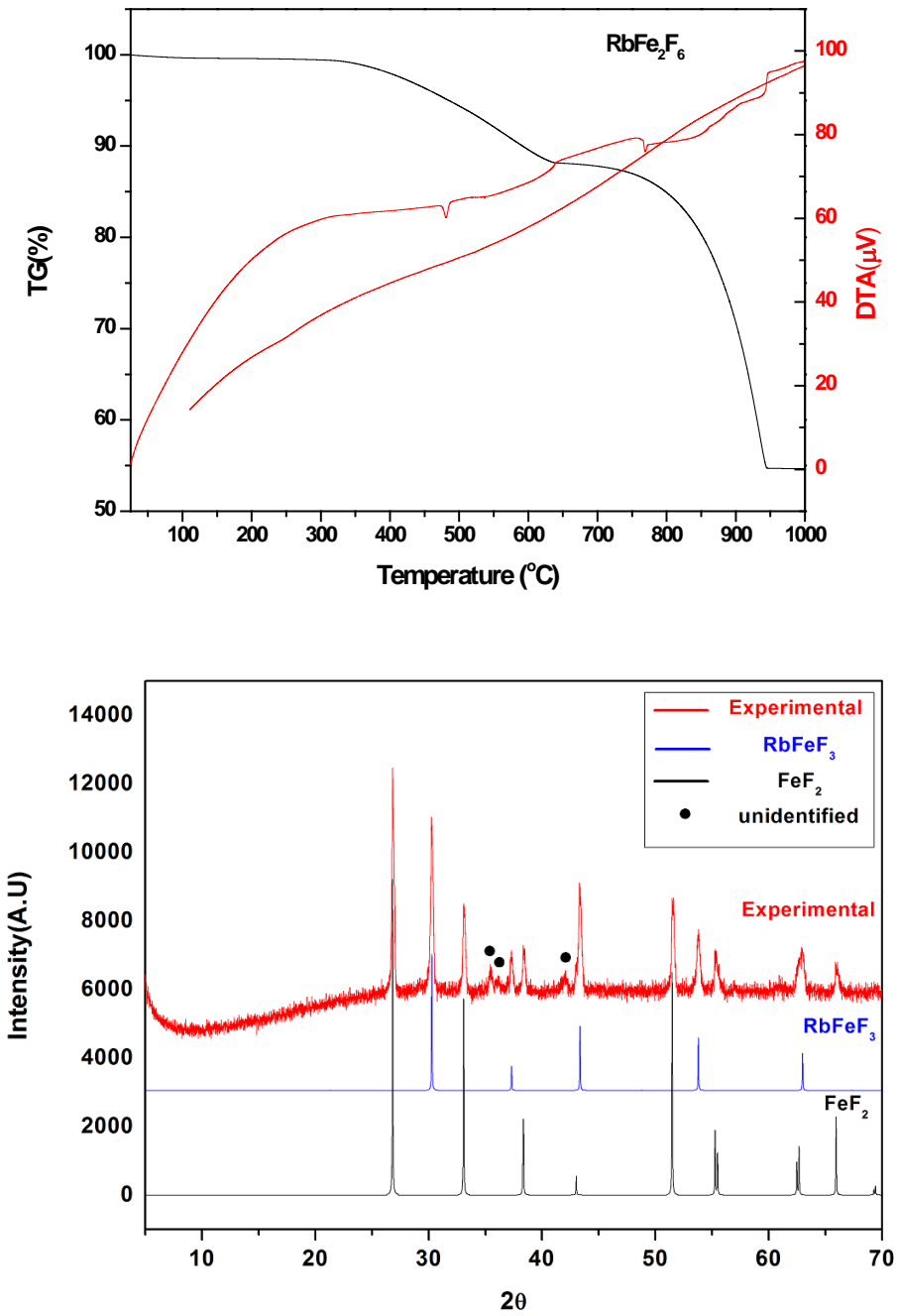
**Figure 3.12** Thermogravimetric analysis and differential thermal analysis diagram (top) and powder X-ray diffraction data for final residuals after TGA Experiment (bottom) for $RbFe_2F_6$.

**Magnetic Property.** Figure 3.13 shows a summary of the basic magnetic characterization of a powder sample of $RbFe_2F_6$. The data shown are measured in an applied magnetic field (H) of 1 kOe, after field cooling (FC) and zero field cooling (ZFC). As shown in panel (a) the dc magnetic susceptibility ($\chi$) is positive, exhibiting a monotonic increase with decreasing temperature down to $16 \pm 0.5$ K, at which point a prominent peak occurs (see inset) and the FC and ZFC curves bifurcate. The $\chi$(T) behavior is thus typical of an antiferromagnet, consistent with the low-temperature neuton diffraction analysis. Considerable additional information can be gathered from the $\chi^{-1}$ vs. T plot shown in Figure 3.13b. The data are seen to adhere quite well to the Curie–Weiss (C–W) form ($\chi$ = C/T - $\theta$), where C and $\theta$ are constants) for T > 100 K or so, yielding a Weiss temperature of -272 K. Fits with an additional temperature-independent paramagnetic susceptibility describe the data even better, yielding an effective number of Bohr magnetons of 7.9 $\mu_B$/f.u. Note that measurement of $\chi$(T) in magnetic fields in the range $10–10^4$ Oe yielded magnetic moment and $\theta$ values that varied by only 10–20%, consistent with the fact that the M(H) curves are quite linear at all T (see inset to Figure 3.13b). The extracted values are similarly robust with respect to the exact temperature range used for the fitting to the C–W form. The theoretical spin only value is 7.7 $\mu$B/f.u. ($Fe^{2+}$ = 4.9 $\mu_B$, $Fe^{3+}$ = 5.9 $\mu_B$), in good agreement with the data. Importantly, the large negative Weiss temperature indicates relatively strong AF interactions between the Fe moments. In fact, comparison to the actual AF ordering temperature of 16 K indicates significant magnetic frustration in this compound, with a frustration ratio ($\theta/T_N$) of 17.[46]
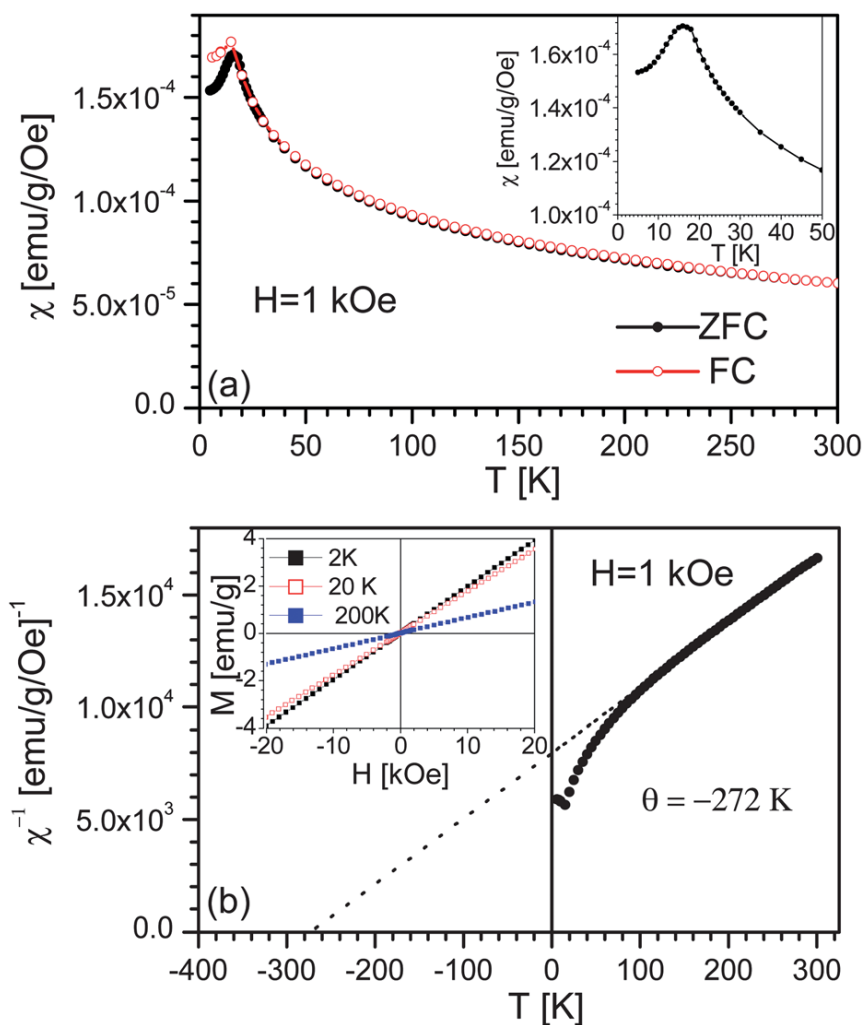
**Figure 3.13** Temperature dependence of (a) the dc magnetic susceptibility measured in 1 kOe (after zero field and field cooling), and (b) the inverse magnetic susceptibility with a Curie–Weiss fit (dotted line). The extracted parameters are shown in the figure. The inset to (a) shows a close up of the low-temperature region revealing the 16 K Néel temperature. The inset to (b) shows the linear magnetization vs. field behavior over the whole temperature range studied.

## 3.5 Conclusion

We have synthesized and characterized a new charge-ordered magnetically frustrated mixed-metal fluoride, $RbFe^{2+}Fe^{3+}F_6$, which exhibits a pyrocholore-related structure. An anti-ferromagnetic ordering temperature of 16 K was observed, however no structural transition was observed in the variable-temperature neutron diffraction data. Theoretical calculations, additional neutron diffraction and magnetic measurements on $RbFe_2F_6$ are in progress.

## 3.6 References

(1)     Hagenmuller, P. *INORGANIC SOLID FLUORIDES Chemistry and Physics*; Academic Press, INC.: Orlando, 1985.

(2)     Keve, E. T.; Abrahams, S. C.; Bernstein, J. L. *J. Chem. Phys.* **1970**, *53*, 3279.

(3)     Keve, E. T.; Abrahams, S. C.; Bernstein, J. L. *J. Chem. Phys.* **1969**, *51*, 4928.

(4)     Eibschutz, M. G., H. J. *Solid State Commun.* **1968**, *6*, 737.

(5)     Ravez, J.; Arquis, S.; Grannec, J.; Simon, A.; Abrahams, S. C. *J. Appl. Phys.* **1987**, *62*, 4299.

(6)     Laligant, Y.; Calage, Y.; Heger, G.; Pannetier, J.; Ferey, G. *J. Solid State Chem.* **1989**, *78*, 66.

(7)     Ferey, G.; de Pape, R.; Boucher, B. *Acta Cryst. B* **1978**, *34*, 1084.

(8)     Ravez, J. *J. Phys. III* **1997**, *7*, 1129.

(9)     Ravez, J.; Abrahams, S. C.; De, P. R. *J. Appl. Phys.* **1989**, *65*, 3987.

(10)    Abrahams, S. C.; Ravez, J.; Simon, A.; Chaminade, J. P. *J. Appl. Phys.* **1981**, *52*, 4740.

(11)    Bergman, J. G.; Crane, G. R.; Guggenheim, H. *J. Appl. Phys.* **1975**, *46*, 4645.

(12)    Blinc, R.; Tavčar, G.; Žemva, B.; Goreshnik, E.; Hanžel, D.; Cevc, P.; Potočnik, A.; Laguta, V.; Trontelj, Z.; Jagličič, Z.; Scott, J. F. *J. Appl. Phys.* **2009**, *106*.

(13)    Blinc, R.; Cevc, P.; Potočnik, A.; Žemva, B.; Goreshnik, E.; Hanžel, D.; Gregorovič, A.; Trontelj, Z.; Jagličič, Z.; Laguta, V.; Perović, M.; Dalal, N. S.; Scott, J. F. *J. Appl. Phys.* **2010**, *107*.

(14)    Scott, J. F.; Blinc, R. *J. Phys. Condens Matter* **2011**, *23*, 113202.

(15)     Scott, J. F.; Blinc, R. *J. Phys. Condens Matter* **2011**, *23*, 299401.

(16)     Babel, D.; Pausewang, G.; Viebahn, W. *Z. Naturforsch., B* **1967**, *22*, 1219.

(17)     Babel, D. *Z. Anorg. Allg. Chem.* **1972**, *387*, 161.

(18)     Greenwood, N. N.; Howe, A. T.; Menil, F. *J. Chem. Soc. A* **1971**, 2218.

(19)     Ferey, G.; Leblanc, M.; De Pape, R. *J. Solid State Chem.* **1981**, *40*, 1.

(20)     Masse, R.; Aleonard, S.; Averbuch-Pouchot, M. T. *J. Solid State Chem.* **1984**, *53*, 136.

(21)     Gaile, J.; Ruedorff, W.; Viebahn, W. *Z. Anorg. Allg. Chem.* **1977**, *430*, 161.

(22)     Kurtz, W.; Roth, S. *Physica B+C* **1977**, *86–88, Part 2*, 715.

(23)     Villain, J. *Z. Phys. B* **1979**, *33*, 31.

(24)     Greenwood, N. N.; Menil, F.; Tressaud, A. *J. Solid State Chem.* **1972**, *5*, 402.

(25)     Tressaud, A.; Menil, F.; Georges, R.; Portier, J.; Hagenmuller, P. *Mater. Res. Bull.* **1972**, *7*, 1339.

(26)     Hardy, A. M.; Hardy, A.; Ferey, G. *Acta Cryst. B* **1973**, *29*, 1654.

(27)     Ferey, G.; Leblanc, M.; De, P. R.; Pannetier, J. *Solid State Commun.* **1985**, *53*, 559.

(28)     Ferey, G.; Leblanc, M.; De Pape, R. *J. Cryst. Growth* **1975**, *29*, 209.

(29)     Herdtweck, E. *Z. Anorg. Allg. Chem.* **1983**, *501*, 131.

(30)     Leblanc, M.; Ferey, G.; Calage, Y.; De, P. R. *J. Solid State Chem.* **1984**, *53*, 360.

(31)     Leblanc, M.; Ferey, G.; Calage, Y.; de Pape, R. *J. Solid State Chem.* **1983**, *47*, 24.

(32)     Kim, S. W.; Chang, H. Y.; Halasyamani, P. S. *J. Am. Chem. Soc.* **2010**, *132*, 17684.

(33)    Brown, I. D.; Altermatt, D. *Acta Cryst.* **1985**, *B41*, 244.

(34)    Brese, N. E.; O'Keeffe, M. *Acta Cryst.* **1991**, *B47*, 192.

(35)    Brown, I. D. *The Chemical Bond in Inorganic Chemistry - The Bond Valence Model. IUCr monographs on Crystallography 12*; Oxford University Press, 2002.

(36)    Raju, K. S.; Wanklyn, B. M. *J. Cryst. Growth* **1993**, *128*, 1078.

(37)    Osin, S. B.; Davliatshin, D. I.; Ogden, J. S. *J. Fluorine Chem.* **1996**, *76*, 187.

(38)    Rother, G.; Worzala, H.; Bentrup, U. *Z. Anorg. Allg. Chem.* **1996**, *622*, 1991.

(39)    Nakamoto, K. *Infrared and Raman Spectra of Inorganic and Coordination Compounds Part A: Theory and Applications in Inorganic Chemistry*; 5th ed.; John Wiley & Sons, Inc: New York, 1997.

(40)    Kubelka, P. M.; Munk, F. *Z. Tech. Phys.* **1931**, *12*, 593.

(41)    Lever, A. B. P. *Inorganic Electronic Spectroscopy, 2nd ed.*; Elsevier Science Publishers B. V.: Amsterdam, 1984.

(42)    Long, G. J.; Grandjean, F. *Mössbauer Spectroscopy Applied to Magnetism and Materials Science.*; Plenum Press: New York, 1993.

(43)    Walton, E. G.; Brown, D. B.; Wong, H.; Reiff, W. M. *Inorg. Chem.* **1977**, *16*, 2425.

(44)    Balcerek, T. W.; Cathey, L.; Karraker, D. G. *J. Inorg. Nucl. Chem.* **1978**, *40*, 773.

(45)    Baum, E.; Dahlke, P.; Kaiser, V.; Molinier, M.; Schmidt, R. E.; Pebler, J.; Massa, W.; Babel, D. *Z. Anorg. Allg. Chem.* **2006**, *632*, 2244.

(46)    Ramirez, A. *Comments. Cond. Mat. Phys.* **1996**, *18*, 21.

**Table 3.1** Crystallographic data for $RbFe_2F_6$.

| Parameter | $RbFe_2F_6$ |
|:---:|:---:|
| **Formula Weight, fw** | 311.17 |
| $T$ **(K)** | 296(2) |
| $\lambda$ **(Å)** | 0.71073 |
| **Crystal System** | Orthorhombic |
| **Space Group** | *Pnma* (No.62) |
| $a$ **(Å)** | 7.0177(6) |
| $b$ **(Å)** | 7.4499(6) |
| $c$ **(Å)** | 10.1765(8) |
| $V$ **(Å$^3$)** | 532.04(8) |
| **Z** | 4 |
| $\rho_{calcd}$ **(g/cm$^3$)** | 3.885 |
| $\mu$**(mm$^{-1}$)** | 14.577 |
| $2\theta_{max}$ **(deg)** | 58.04 |
| $R$ **(int)** | 0.0361 |
| **GOF** | 1.087 |
| $R$ $(F)$[a] | 0.0214 |
| $R_w$ $(F_o^2)$[b] | 0.0497 |

[a]$R\ (F) = \Sigma||F_o| - |F_c||/\Sigma|F_o|$ , [b]$R_w\ (F_o^2) = [\Sigma w(F_o^2 - F_c^2)^2/\Sigma w(F_o^2)^2]^{1/2}$

**Table 3.2** Atomic coordinates for $RbFe_2F_6$.

| Atom | x | y | z | $U_{eq}(\text{Å}^2)^a$ |
|---|---|---|---|---|
| **Rb(1)** | 0.9920(1) | 0.25 | 0.3780(1) | 0.0319(1) |
| **Fe(1) ($Fe^{2+}$)** | 0.7967(1) | 0.25 | 0.7315(1) | 0.0131(1) |
| **Fe(2) ($Fe^{3+}$)** | 0.5 | 0 | 0.5 | 0.0113(1) |
| **F(1)** | 0.7364(2) | 0.0633(2) | 0.5812(1) | 0.0190(3) |
| **F(2)** | 0.3737(2) | 0.0104(2) | 0.6661(1) | 0.0217(3) |
| **F(3)** | 0.4359(3) | 0.25 | 0.4650(2) | 0.0197(4) |
| **F(4)** | 0.5642(3) | 0.25 | 0.8384(2) | 0.0229(4) |

[a] $U_{eq}$ is defined as one-third of the trace of the orthogonal $U_{ij}$ tensor.

**Table 3.3** Selected bond distances for RbFe$_2$F$_6$.

| Bond | Distance (Å) | Bond | Distance (Å) |
|------|--------------|------|--------------|
| **Rb(1) — F(1)** | 3.042(1) × 2 | **Fe(1) — F(1)** | 2.110(1) × 2 |
| **Rb(1) —F(1)** | 3.071(1) × 2 | **Fe(1) — F(2)** | 2.137(1) × 2 |
| **Rb(1) — F(2)** | 3.050(2) × 2 | **Fe(1) — F(4)** | 1.961(2) |
| **Rb(1) — F(2)** | 3.248(1) × 2 | **Fe(1) — F(4)** | 2.008(2) |
| **Rb(1) — F(3)** | 3.239(2) | **Fe(2) — F(1)** | 1.913(1) × 2 |
| **Rb(1) — F(4)** | 2.931(2) | **Fe(2) — F(2)** | 1.910(1) × 2 |
| | | **Fe(2) — F(3)** | 1.949(1) × 2 |
| | | **Fe(1) — Fe(1)** | 3.529(1) × 2 |
| | | **Fe(2) — Fe(2)** | 3.725(1) × 2 |
| | | **Fe(1) — Fe(2)** | 3.602(1) × 2 |
| | | **Fe(1) — Fe(2)** | 3.654(1) × 2 |

**Table 3.4** Bond valence analysis for $RbFe_2F_6{}^a$.

| Atom | F(1) | F(2) | F(3) | F(4) | $\Sigma_{cations}$ |
|---|---|---|---|---|---|
| **Rb(1)** | $0.0922^{[\times2]}$ $0.0853^{[\times2]}$ | $0.0903^{[\times2]}$ $0.0529^{[\times2]}$ | 0.0541 | 0.1246 | **0.8201** |
| **Fe(1)** | $0.2883^{[\times2]}$ | $0.2683^{[\times2]}$ | - | 0.4319 0.3804 | **1.926** |
| **Fe(2)** | $0.5192^{[\times2]}$ | $0.5230^{[\times2]}$ | $0.4707^{[\times2]}$ | - | **3.026** |
| $\Sigma_{anions}$ | **0.9850** | **0.9345** | **0.9955** | **0.9369** | |

$^a$ Bond valence sums calculated with the formula: $S_i = \exp[(R_0 - R_i)/B]$, where $S_i$=valence of bond "$i$" and B=0.37. Superscripts indicate the # of equivalent bonds for anions; subscripts indicate that the # of equivalent bonds for cations.

**Table 3.5** Refined positions as obtained from Rietveld refinement of the powder neutron diffraction at 4 K in the *Pnma* space group with cell parameter of $a = 6.96630(5)$, $b = 7.43903(5)$ and $c = 10.12164(7)$ Å. Final $wR_p = 4.34$ %, $R_{bragg} = 2.17$ %, and R-factor of 3.35 %.

| Atom | x | y | z | B | Moment $\mu_B$ |
|------|------|------|------|------|------|
| Rb(1) | 0.9942(3) | 0.25 | 0.3798(2) | 0.43(3) | |
| Fe(1) | 0.8014(2) | 0.25 | 0.7302(1) | 0.20(2) | 3.99(5) |
| Fe(2) | 0.5 | 0 | 0.5 | 0.17(2) | 4.29(5) |
| F(1) | 0.7413(2) | 0.0644(2) | 0.5784(2) | 0.53(3) | |
| F(2) | 0.3791(2) | 0.0077(3) | 0.6698(1) | 0.50(3) | |
| F(3) | 0.4322(3) | 0.25 | 0.4672(2) | 0.51(4) | |
| F(4) | 0.5682(3) | 0.25 | 0.8407(2) | 0.35(3) | |

**Table 3.6** Mössbauer Parameters for reported iron fluoride materials at R.T.

| Material | $Fe^{2+}$ | | $Fe^{3+}$ | | Ref |
|---|---|---|---|---|---|
| | I.S.(mm/s) | Q.S.(mm/s) | I.S.(mm/s) | Q.S.(mm/s) | |
| $Fe_2F_5 \cdot 2H_2O$ | 1.60 | 2.44 | 0.70 | 0.65 | 44 |
| $Fe_2F_5 \cdot 7H_2O$ | 1.215 | 3.284 | 0.393 | 0.59 | 45 |
| $NH_4Fe_2F_6$ | 1.36 | 2.61 | 0.42 | 0.72 | 24 |
| $RbFe_2F_6$ | 1.315 | 2.664 | 0.474 | 0.720 | This work |
| $CsFe_2F_6$ | 1.27 | 2.55 | 0.32 | 0.73 | 46 |

**CHAPTER 4. K$_4$Fe$_3$F$_{12}$: Synthesis, Structure, and Characterization of a New Mixed Valence Iron (Fe$^{2+}$/Fe$^{3+}$) Fluoride Material with a Layered Perovskite-related Structure**

**4.1 Abstract**

A new mixed valence iron (Fe$^{2+}$/Fe$^{3+}$) fluoride material with a layered perovskite-related structure has been synthesized and characterized. The material, K$_4$Fe$_3$F$_{12}$ (K$_4$(Fe$^{2+}$)(Fe$^{3+}$)$_2$F$_{12}$), was synthesized through mild hydrothermal conditions. The material exhibits a layered perovskite structure consisting of corner-shared Fe$^{2+}$F$_6$ and Fe$^{3+}$F$_6$ octahedra. Each corner-shared FeF$_6$ octahedron is formed the perovskite layers in an ordered fashion; each Fe$^{2+}$F$_6$ octahedral layer is sandwiched between two Fe$^{3+}$F$_6$ layers. In addition to single-crystal diffraction data, magnetic measurement, Infrared, UV-vis, $^{57}$Fe-Mössbauer, thermogravimetric, and differential thermal analysis measurements were carried out. Crystal data: K$_4$Fe$_3$F$_{12}$, trigonal space group *R-3m* (No. 62), $a = 7.0177(6)$, $b = 7.4499(6)$, $c = 10.1765(8)$ Å, $V = 532.04(8)$ Å$^3$, $Z = 4$, $T = 296(2)$ K.

## 4.2 Introduction

Iron-fluoride materials have been investigated thoroughly because of their huge variety of structural forms and some unusual physical properties derived from those structures.[1-2] Simple examples are ferric fluoride ($FeF_3$), which has rhombohedral, hexagonal tungsten bronze (HTB), pyrochlore, and amorphous forms, and which shows several examples of magnetic frustration which may be associated with structural disorder.[1-4] With respect to mixed valence iron ($Fe^{2+}/Fe^{3+}$) fluoride materials, various structure-type materials were synthesized and characterized. For example, there exists the trirutile-type structure $Li(Fe^{2+})(Fe^{3+})F_6$,[5-6] modified pyrochlore-type structure $A(Fe^{2+})(Fe^{3+})F_6$ ($A^+ =$ $Rb^+$, $Cs^+$, $NH_4^+$),[7-10] tetragonal tungsten bronze-type (TTB) structure $K_{0.6}(Fe^{2+})_{0.6}(Fe^{3+})_{0.4}F_3$,[11] hexagonal tungsten bronze-type (HTB) structure $(Fe^{2+})(Fe^{3+})_2F_8 \cdot 2H_2O$,[12] Weberite-type structure $Na_2(Fe^{2+})(Fe^{3+})F_7$,[13] Inverse Weberite-type structure $(Fe^{2+})(Fe^{3+})F_5 \cdot 2H_2O$[14] and Jarite-type structure $Ba_7(Fe^{2+})(Fe^{3+})_6F_{34}$[15] and $Pb_7(Fe^{2+})(Fe^{3+})_6F_{34}$.[16] Interestingly, some mixed valence iron fluoride materials showed unusual magnetic properties as well as ferroelectric properties attributable to charge ordering or magnetic ordering in the structure. For example, $K_3Fe_5F_{15}$, which contains two $Fe^{3+}$ and three $Fe^{2+}$ ions, showed multiferroic behavior.[17-21]

Although the importance of mixed valence iron fluoride materials is recognized, there has not been fully investigated because of difficulties of preparation and controlling the oxidation state of iron. Thus, a new synthetic method should be required to synthesize new mixed valence iron ($Fe^{2+}/Fe^{3+}$) fluoride materials. We recently reported the synthesis and characterization of a new charge-ordered $Fe^{2+}/Fe^{3+}$ fluoride material,

RbFe$_2$F$_6$.[10] This material was synthesized using a mild hydrothermal method using CF$_3$COOH aqueous solution. In this chapter, utilizing a similar synthetic technique, we report the synthesis and characterization of a new charge ordered layered perovskite-related mixed valence iron fluoride material, K$_4$(Fe$^{2+}$)(Fe$^{3+}$)$_2$F$_{12}$.

## 4.3 Experimental Section

### 4.3.1 Reagents

KF (Alfa Aesar, ACS 99 %), FeF$_2$ (Alfa Aesar, 99%), FeF$_3$ (Alfa Aesar, 97%), and CF$_3$COOH (Alfa Aesar, 99%) were used without any further purification.

### 4.3.2 Synthesis

K$_4$Fe$_3$F$_{12}$ was obtained by the hydrothermal method using a diluted CF$_3$COOH solution. Crystals of K$_4$Fe$_3$F$_{12}$ were grown by mixing 0.125 g (2.15×10$^{-3}$ mol) of KF, 0.107 g (1.14×10$^{-3}$ mol) of FeF$_2$, 0.129 g (1.14×10$^{-3}$ mol) of FeF$_3$ and 3 ml (3.90×10$^{-2}$ mol) of CF$_3$COOH with 5 ml of H$_2$O. The resultant solution was placed in a 23-mL Teflon-lined stainless autoclave that was subsequently sealed. The autoclave was gradually heated to 230 ºC, held for 24 h, and cooled slowly to room temperature at a rate of 6 ºC h$^{-1}$. The mother liquor was decanted from the only solid product, brownish yellow colored hexagonal plate shaped crystals of K$_4$Fe$_3$F$_{12}$, which were recovered by filtration and washed with distilled water and acetone. The yield was ~50 % on the basis of FeF$_2$. A powder X-ray diffraction pattern on the synthesized phase is in good agreement with the pattern generated from the single-crystal data.

## 4.4 Results and discussion

**Synthesis.** Previously reported mixed valence iron ($Fe^{2+}/Fe^{3+}$) fluoride materials, e.g., $NH_4Fe_2F_6$, $Fe_2F_5 \cdot 2H_2O$, $Fe_3F_8 \cdot 2H_2O$, and $Ba_7Fe_7F_{34}$ were synthesized by solid state reaction or hydrothermal reaction using aqueous HF solution or $NH_4F$ solution above 350 °C.[7,12,14-15] We were able to synthesize $K_4Fe_3F_{12}$ through a low-temperature and mild hydrothermal technique. In our method, the binary metal fluorides are combined with KF and a dilute $CF_3COOH$ aqueous solution. We have previously demonstrated that this method can be used to synthesize the new mixed valence iron ($Fe^{2+}/Fe^{3+}$) fluoride material, $RbFe_2F_6$.[10]
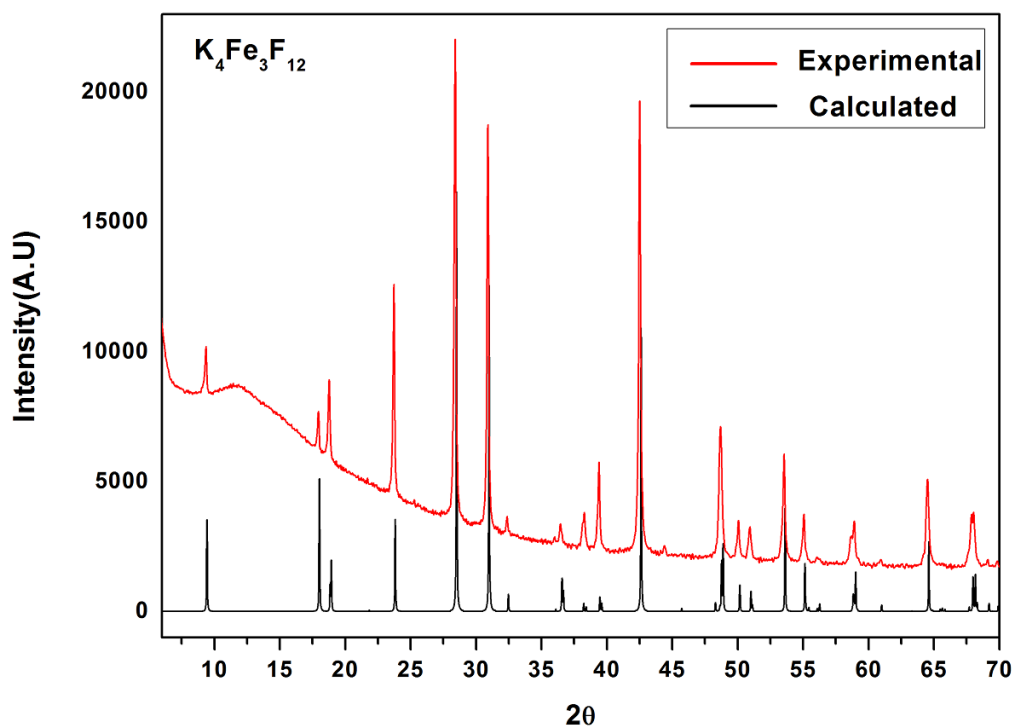


**Figure 4.1** Experimental and calculated powder X-ray diffraction patterns for $K_4Fe_3F_{12}$.

**Structure.** $K_4Fe_3F_{12}$ crystallizes in the *R*-3m space group with lattice parameters of $a = b = 5.7649(9)$ Å, and $c = 28.089(9)$ Å at room temperature. This phase has similarities to perovskite-related $A_nB_{n-\delta}O_{3n}$ (n = 4 and $\delta$ = 1) families, such as $A_4MRe_2O_{12}$ ($A^{2+}$ = Sr, Ba, $M^{2+}$ = Mg, Ca, Co, Ni, Zn, and Cd), $Ba_3LaInW_2O_{12}$, and $Ba_2La_2MnW_2O_{12}$, which also crystallizes in the *R*-3m space group and exhibit characteristic lattice parameters *a*, *b* about 5.7 Å and *c* about 27.4 Å.[22-24]

$K_4Fe_3F_{12}$ exhibits a layered structure consisting of triple perovskite layers of $[Fe_3F_{12}]^{4-}$ stacked alternatively with a layer of $K^+$ along the *c*-axis direction (Figure 4.2). The formula may be also written as $K_4(Fe^{2+})(Fe^{3+})_2F_{12}$, as the $Fe^{2+}$ and $Fe^{3+}$ cations are ordered in the structure. This is very rare example of a layered perovskite structure in a fluoride system. The material has two crystallographically unique iron sites, which contain one $Fe^{2+}$ and one $Fe^{3+}$ cation, respectively. Each corner-shared $FeF_6$ octahedron forms the perovskite layers in an ordered fashion; the $Fe^{2+}F_6$ octahedral layer is sandwiched by two $Fe^{3+}F_6$ layers. In connectivity terms, the structure may be written as $((Fe(II)F_{6/2})^-(2(Fe(III)F_{3/1}F_{3/2})^{1.5-})^{3-})^{4-}$ where charge balance is maintained by four $K^+$ cations. The bond distance of $Fe^{2+}$ - F is 2.079(1) Å and $Fe^{3+}$ - F bond distances range between 1.864(1) -2.016(1) Å. The K(1) and K(2) cations are in a 12 - fold and a 9 - fold coordinate environment, respectively, with K - F distances that range between 2.671(2) - 2.946(1) Å. The bond angles of F - $Fe^{2+}$ - F are 86.85(5)°, 93.17(5)°, and 180.0°, the bond angles of F - $Fe^{3+}$ - F are 85.78(6)°, 88.62(4)°, 96.46(5)° and 172.35(6)°, and the bond angle of $Fe^{2+}$ - F - $Fe^{3+}$ is 174.79(7)° (See Table 4.3). Bond valence calculations[25-26]

(see Table 4.4) resulted in values of 0.867-1.27, 1.88, 3.02 and 0.891-1.05 for $K^+$, $Fe^{2+}$, $Fe^{3+}$ and $F^-$, respectively.
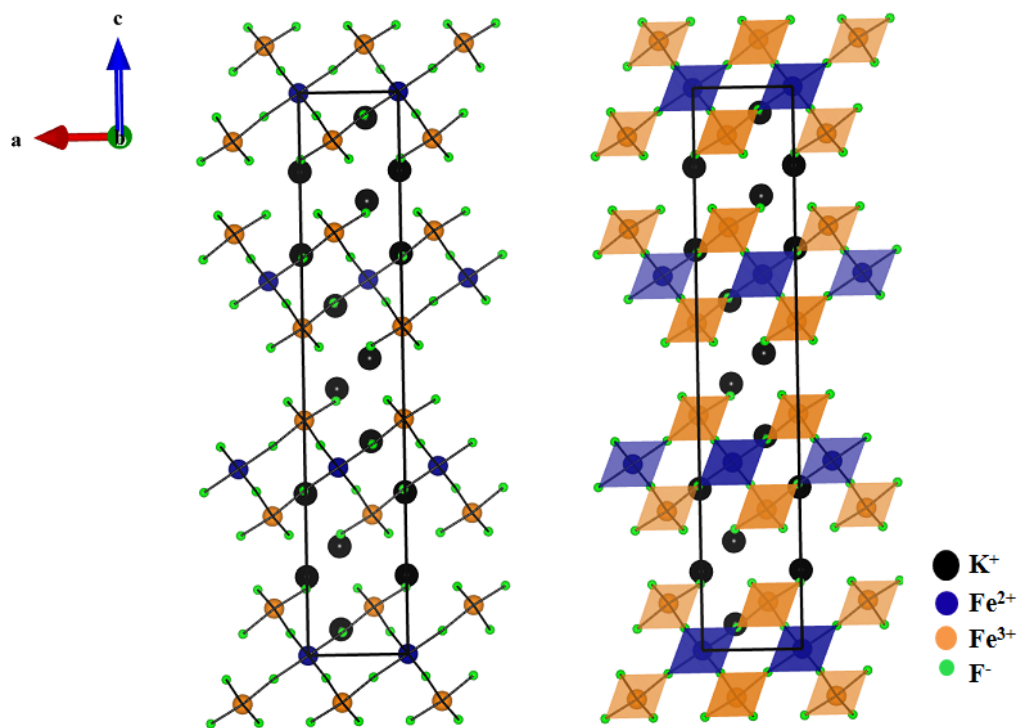


**Figure 4.2** Ball-and-stick and Polyhedral representation of $K_4Fe_3F_{12}$ in the *ac*-plane.

**K(1)**            **K(2)**

**Fe(1)**           **Fe(2)**
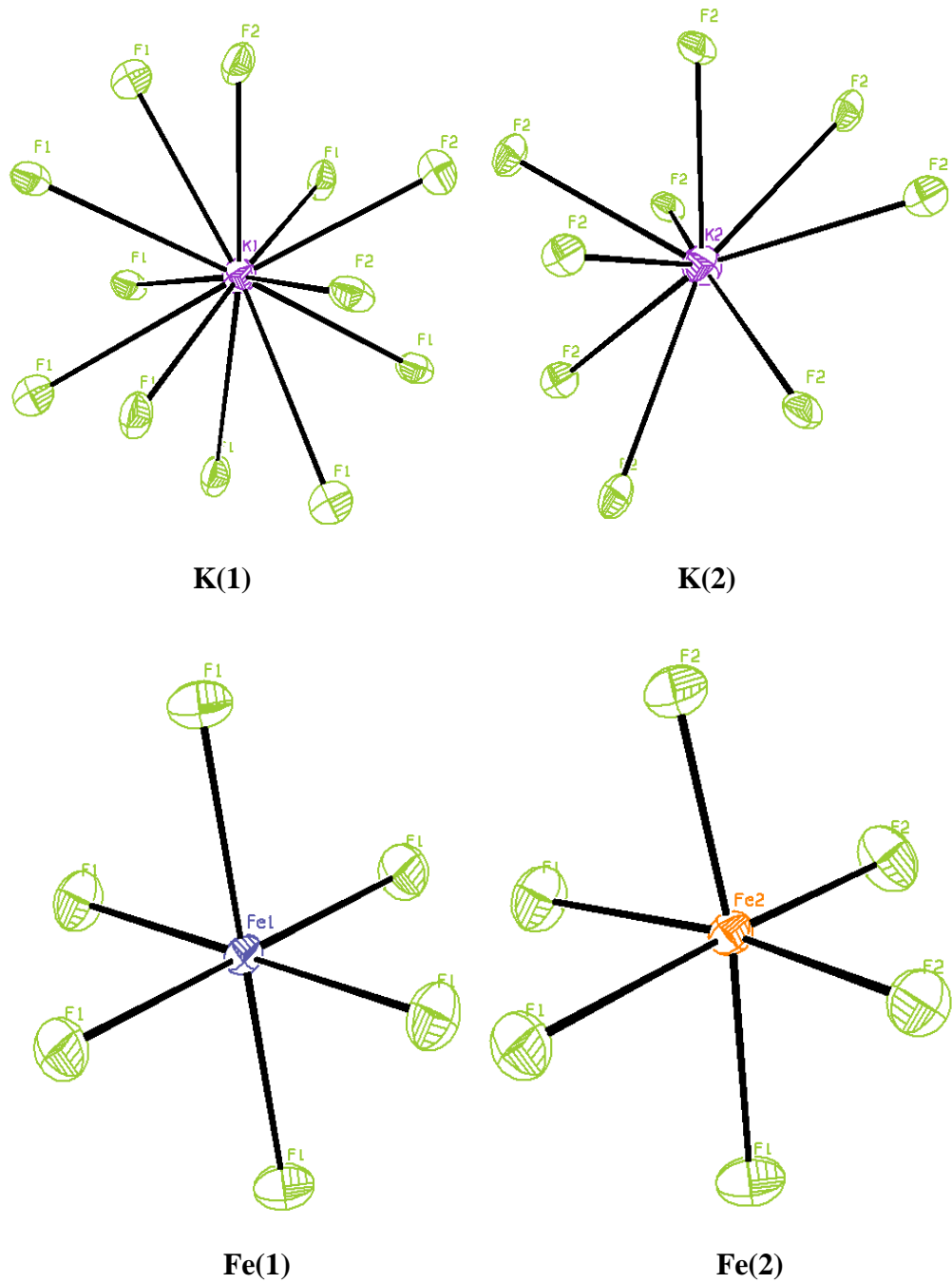
**Figure 4.3** ORTEP (50% probability ellipsoids) diagrams for $K_4Fe_3F_{12}$.

**Infrared Spectroscopy.** The FT-IR spectra of $K_4Fe_3F_{12}$ revealed Fe-F vibrations between 1000 and 400 $cm^{-1}$ (Figure 4.4). The bands occurring between 800 – 700 $cm^{-1}$ and 600 – 400 $cm^{-1}$ can be assigned to Fe – F and Fe – F – Fe vibrations, respectively. These assignments are consistent with previous reports.[27-30]
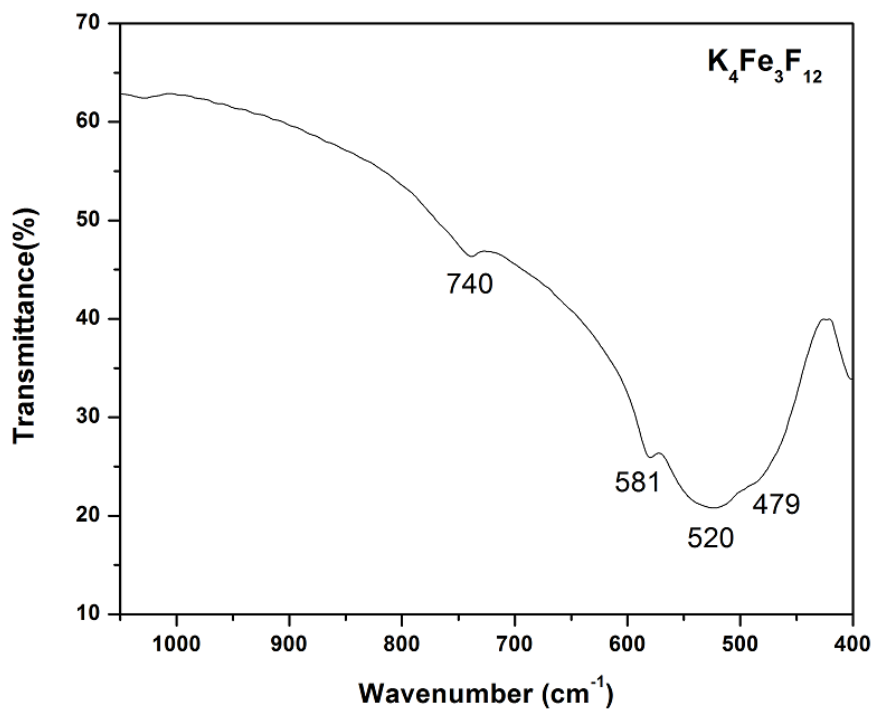


| $K_4Fe_3F_{12}$ | |
|---|---|
| $\upsilon$(Fe-F) | $\upsilon$(Fe-F-Fe) |
| 740 | 581 |
| | 520 |
| | 479 |

**Figure 4.4** IR spectra and assignment for $K_4Fe_3F_{12}$.[27-30]

**UV-Vis Diffuse Reflectance Spectroscopy.** The UV-Vis diffuse reflectance spectra indicated that the absorption energy for $K_4Fe_3F_{12}$ is approximately 2.32 eV. This is consistent with the brownish yellow color of the material. Absorption (K/S) data were calculated through the Kubelka-Munk function[31-32]:

$$F(R) = \frac{(1-R)^2}{2R} = \frac{K}{S}$$

with $R$ representing the reflectance, $K$ the absorption, and $S$ the scattering. In a $K/S$ versus E(eV) plot, extrapolating the linear part of rising curve to zero provides the onset of absorption at 2.32 eV. One band in the region of 2.0 – 3.0 eV was attributed to d-d transition of Fe, the other large broad bands in the region of 3.2 – 5.0 eV were attributed to metal to ligand charge transfer (See Figure 4.5).
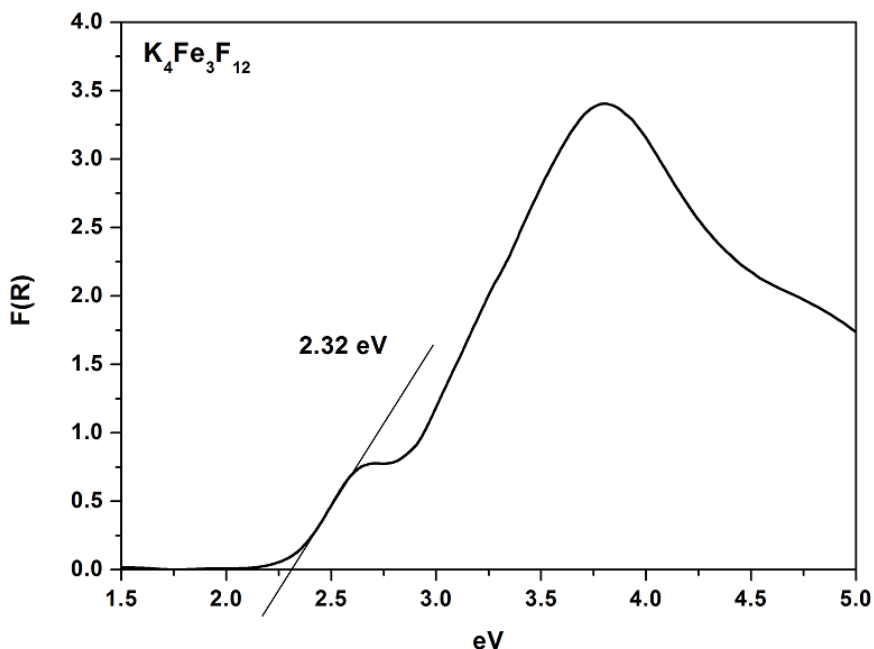


**Figure 4.5** UV-Vis diffuse reflectance spectrum for $K_4Fe_3F_{12}$.

**$^{57}$Fe Mössbauer Spectroscopy.** The Mössbauer spectra of $K_4Fe_3F_{12}$ at R.T showed three doublets, which indicated the isomer shift and quadrupole splitting of one $Fe^{2+}$ and two $Fe^{3+}$, respectively (see Figure 4.6). The isomer shift (1.22 mm/s) and quadrupole splitting (1.00 mm/s) observed for $Fe^{2+}$ and the isomer shift (0.388 mm/s and 0.677 mm/s) and quadrupole splitting (0.467 mm/s and 0.747 mm/s) observed for $Fe^{3+}$ revealed the octahedral coordination of $Fe^{2+}$ and $Fe^{3+}$ sites, respectively.[33] The ratio of $Fe^{3+}$ to $Fe^{2+}$ is almost double with respect to the peak area of spectra.

**Thermal Analysis.** The thermal behavior of $K_4Fe_3F_{12}$ was investigated using thermogravimetric analysis (TGA) and differential thermal analysis (DTA) under nitrogen atmosphere (see Figure 4.7). The decomposition started around 350 $^o$C and additional step was also observed at around 750 $^o$C, which possibly is attributed to the loss of fluorides. DTA also showed two endothermic peaks at ~400 $^o$C and ~800 $^o$C, which indicated the decomposition of samples. Furthermore, during the cooling step, DTA showed strong exthothermic peak at ~830 $^o$C and weak exthothermic peak at ~800 $^o$C, which indicated re-crystallization of decomposed samples. The final residue products, Fe, FeO, and unknown phase were confirmed by PXRD.
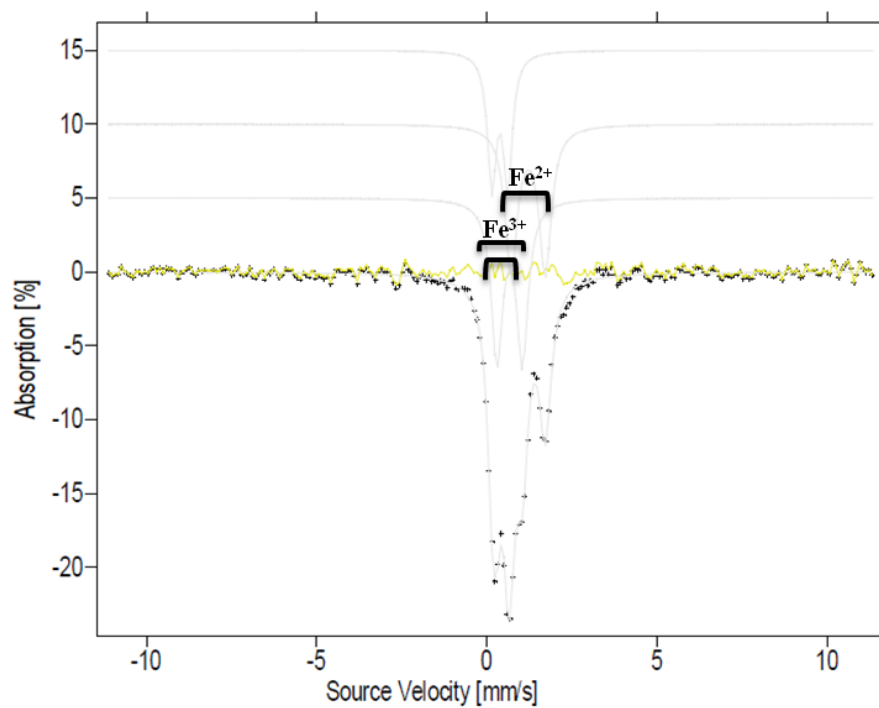
| | K₄Fe₃F₁₂ | | |
|---|---|---|---|
| **Fe** | **I.S. (mm/s) (±0.01)** | **Q.S. (mm/s) (±0.01)** | **Area(%) (±2)** |
| $Fe^{3+}$ | 0.388 | 0.467 | **26** |
| $Fe^{3+}$ | 0.677 | 0.747 | **40** |
| $Fe^{2+}$ | 1.22 | 1.00 | **34** |

**Figure 4.6** Mössbauer Spectra and parameter of $K_4Fe_3F_{12}$ at R.T.
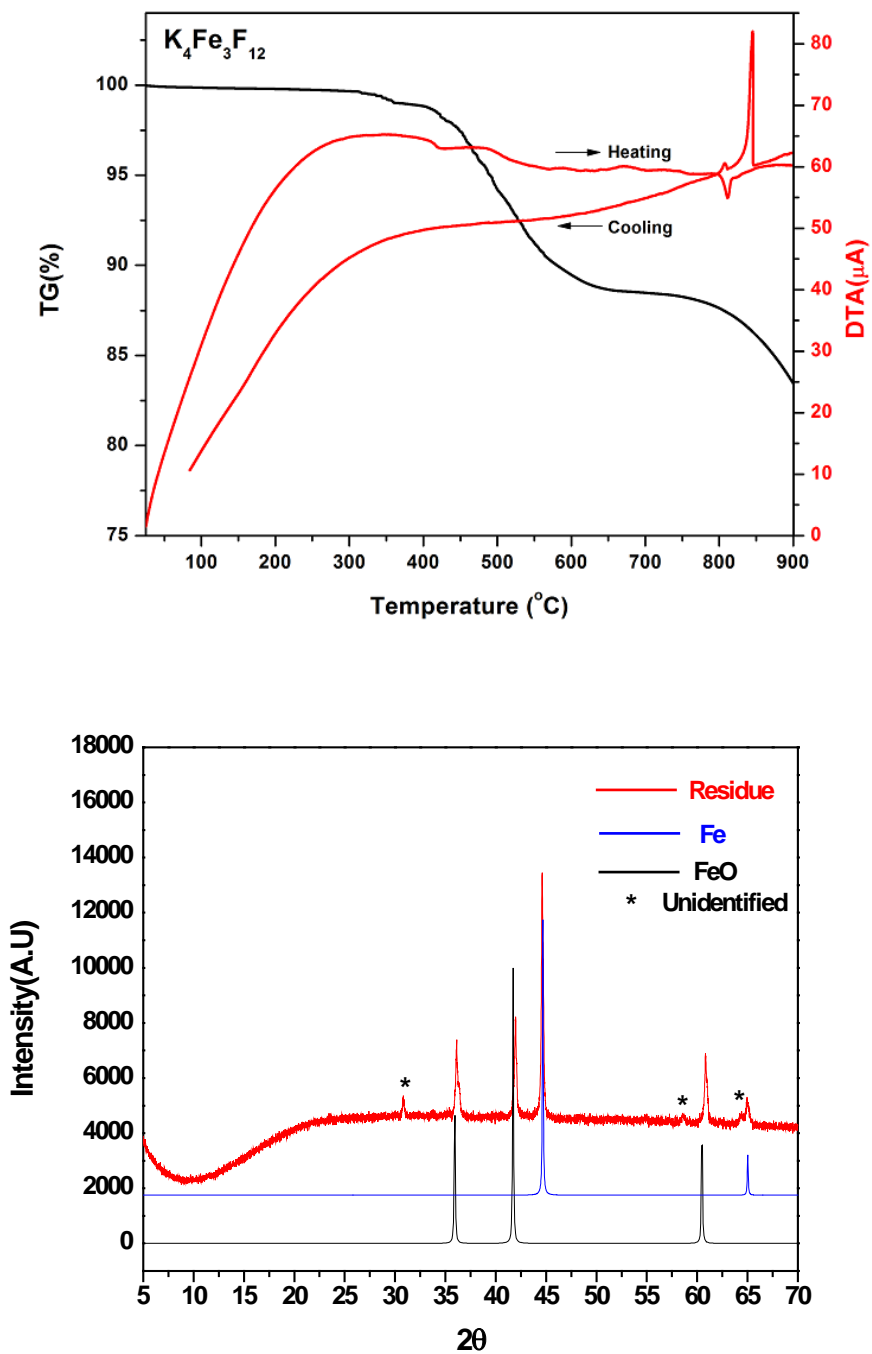
**Figure 4.7** Thermogravimetric analysis and differential thermal analysis diagram (top) and Powder X-ray diffraction data for final residuals after TGA Experiment (bottom) for $K_4Fe_3F_{12}$.

**Magnetic Properties.** Zero field cooled (ZFC) and field cooled (FC) magnetization measurements of $K_4Fe_3F_{12}$ were performed in a range of 2 - 300 K at different magnetic fields (10, 100, 1000, and 10000 Oe). The curves are shown in Figure 4.8 where a significant divergence between ZFC and FC curves occur at around 120 K. The divergence is reduced as the magnetic field increases from 10 to 1000 Oe and eventually, no divergence is found measured at 1 T. Overall, the FC curves reveal a ferromagnetic-like transition at around 120 K. However, the Curie-Weiss fit indicates that anti-ferromagnetic interactions are favorable attributable to negative Weiss temperature of -80 K. Therefore, it is a signature of a ferrimagnetic behavior that is confirmed from field-dependent magnetization measurements. More detailed magnetic measurements and magnetic structure analysis using neutron diffraction are required to understand the magnetic behavior of $K_4Fe_3F_{12}$.
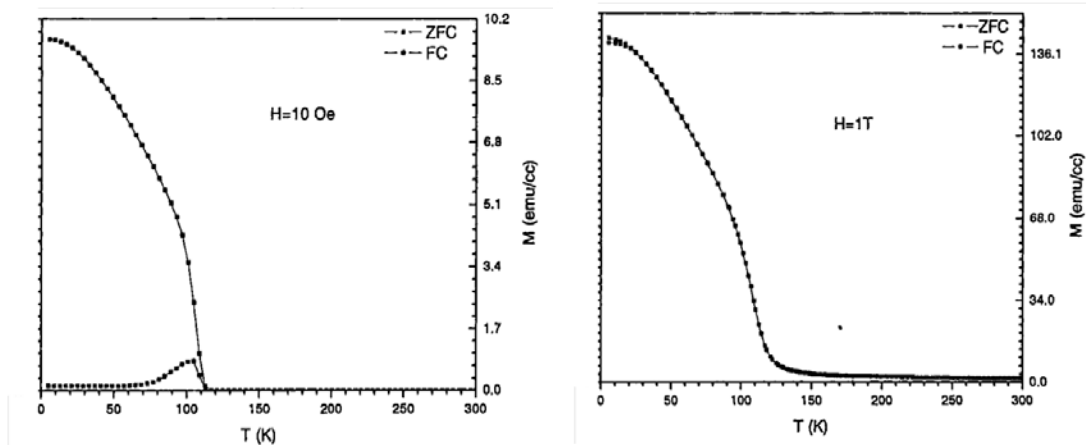


**Figure 4.8** The ZFC and FC temperature dependent magnetization curves measured at 10 Oe (left) and 1 T (right) for $K_4Fe_3F_{12}$.

## 4.5 Conclusion

We have synthesized and characterized a new charge-ordered mixed-metal fluoride material, $K_4(Fe^{2+})(Fe^{3+})_2F_{12}$, that exhibits a layered perovskite-related structure. Magnetic property of $K_4Fe_3F_{12}$ showed ferrimagnetic behavior ($T_c$ = 120 K). More detailed magnetic property measurements and neutron diffraction measurements to understand the magnetic behavior of $K_4Fe_3F_{12}$ are in progress.

**4.6 References**

(1)     Hagenmuller, P. *INORGANIC SOLID FLUORIDES Chemistry and Physics*; Academic Press, INC.: Orlando, 1985.

(2)     Massa, W.; Babel, D. *Chem. Rev.* **1988**, *88*, 275.

(3)     Ferey, G.; Leblanc, M.; De, P. R.; Passaret, M.; Bothorel-Razazi, M. P. *J. Cryst. Growth* **1975**, *29*, 209.

(4)     De Pape, R.; Ferey, G. *Mater. Res. Bull.* **1986**, *21*, 971.

(5)     Shachar, G.; Makovsky, J.; Shaked, H. *Phys. Rev. B* **1972**, *6*, 1968.

(6)     Fourquet, J. L.; Le Samedi, E.; Calage, Y. *J. Solid State Chem.* **1988**, *77*, 84.

(7)     Ferey, G.; Leblanc, M.; De Pape, R. *J. Solid State Chem.* **1981**, *40*, 1.

(8)     Ferey, G.; Leblanc, M.; De, P. R.; Pannetier, J. *Solid State Commun.* **1985**, *53*, 559.

(9)     Baum, E.; Dahlke, P.; Kaiser, V.; Molinier, M.; Schmidt, R. E.; Pebler, J.; Massa, W.; Babel, D. *Z. Anorg. Allg. Chem.* **2006**, *632*, 2244.

(10)    Kim, S. W.; Kim, S.-H.; Halasyamani, P. S.; Green, M. A.; Bhatti, K. P.; Leighton, C.; Das, H.; Fennie, C. J. *Chem. Sci.* **2012**, *3*, 741.

(11)    Hardy, A. M.; Hardy, A.; Ferey, G. *Acta Cryst. B* **1973**, *29*, 1654.

(12)    Herdtweck, E. *Z. Anorg. Allg. Chem.* **1983**, *501*, 131.

(13)    Yakubovich, O.; Urusov, V.; Massa, W.; Frenzen, G.; Babel, D. *Z. Anorg. Allg. Chem.* **1993**, *619*, 1909.

(14)    Walton, E. G.; Brown, D. B.; Wong, H.; Reiff, W. M. *Inorg. Chem.* **1977**, *16*, 2425.

(15)     Le, L. A.; Darriet, J.; Tressaud, A.; Hagenmuller, P. *C. R. Acad. Sci., Ser. 2* **1989**, *308*, 713.

(16)     Pierrard, A.; de, K. A.; Gredin, P.; Renaudin, J. *Z. Anorg. Allg. Chem.* **1996**, *622*, 1200.

(17)     Ravez, J.; Abrahams, S. C.; De, P. R. *J. Appl. Phys.* **1989**, *65*, 3987.

(18)     Ravez, J.; Abrahams, S. C.; Mercier, A. M.; Rabardel, L.; De Pape, R. *J. Appl. Phys.* **1990**, *67*, 2681.

(19)     Fabbrici, S.; Montanari, E.; Righi, L.; Calestani, G.; Migliori, A. *Chem. Mater* **2004**, *16*, 3007.

(20)     Blinc, R.; Tavcar, G.; Zemva, B.; Hanzel, D.; Cevc, P.; Filipic, C.; Levstik, A.; Jaglicic, Z.; Trontelj, Z.; Dalal, N.; Ramachandran, V.; Nellutla, S.; Scott, J. F. *J. Appl. Phys.* **2008**, *103*, 074114/1.

(21)     Mezzadri, F.; Fabbrici, S.; Montanari, E.; Righi, L.; Calestani, G.; Gilioli, E.; Bolzoni, F.; Migliori, A. *Phys. Rev. B: Condens. Matter Mater. Phys.* **2008**, *78*, 064111/1.

(22)     Kemmler-Sack, S. *Z. Anorg. Allg. Chem.* **1980**, *461*, 142.

(23)     Rother, H. J.; Fadini, A.; Kemmler-Sack, S. *Z. Anorg. Allg. Chem.* **1980**, *463*, 137.

(24)     Li, Z.; Sun, J.; You, L.; Wang, Y.; Lin, J. *J. Alloys Comp.* **2004**, *379*, 117.

(25)     Brown, I. D.; Altermatt, D. *Acta Cryst.* **1985**, *B41*, 244.

(26)     Brown, I. D. *The Chemical Bond in Inorganic Chemistry - The Bond Valence Model. IUCr monographs on Crystallography 12*; Oxford University Press, 2002.

(27)     Raju, K. S.; Wanklyn, B. M. *J. Cryst. Growth* **1993**, *128*, 1078.

(28)     Osin, S. B.; Davliatshin, D. I.; Ogden, J. S. *J. Fluorine Chem.* **1996**, *76*, 187.

(29)     Rother, G.; Worzala, H.; Bentrup, U. *Z. Anorg. Allg. Chem.* **1996**, *622*, 1991.

(30)     Nakamoto, K. *Infrared and Raman Spectra of Inorganic and Coordination Compounds Part A: Theory and Applications in Inorganic Chemistry*; 5th ed.; John Wiley & Sons, Inc: New York, 1997.

(31)     Kubelka, P. M.; Munk, F. *Z. Tech. Phys.* **1931**, *12*, 593.

(32)     Tauc, J. *Mater. Res. Bull.* **1970**, *5*, 721.

(33)     Long, G. J.; Grandjean, F. *Mössbauer Spectroscopy Applied to Magnetism and Materials Science.*; Plenum Press: New York, 1993.

**Table 4.1** Crystallographic Data for $K_4Fe_3F_{12}$.

| Parameter | $K_4Fe_3F_{12}$ |
|---|---|
| **F.W.** | 551.95 |
| $T$ **(K)** | 296(2) |
| $\lambda$ **(Å)** | 0.71073 |
| **Crystal System** | Trigonal |
| **Space Group** | *R-3m* (No.166) |
| $a$ **(Å)** | 5.7649(9) |
| $b$ **(Å)** | 5.7649(9) |
| $c$ **(Å)** | 28.086(9) |
| $V$ **(Å$^3$)** | 808.36(3) |
| **Z** | 3 |
| $\rho_{calcd}$ **(g/cm$^3$)** | 3.401 |
| $\mu$**(mm$^{-1}$)** | 5.674 |
| $2\theta_{max}$ **(deg)** | 57.94 |
| $R$ **(int)** | 0.0402 |
| **GOF** | 1.106 |
| $R$ $(F)^a$ | 0.0188 |
| $R_w$ $(F_o^2)^b$ | 0.0579 |

$^a R\ (F) = \Sigma||F_o| - |F_c||/\Sigma|F_o|$ , $^b R_w\ (F_o^2) = [\Sigma w(F_o^2 - F_c^2)^2/\Sigma w(F_o^2)^2]^{1/2}$

**Table 4.2** Atomic Coordinates for $K_4Fe_3F_{12}$.

| Atom | x | y | z | $U_{eq}(Å^2)^a$ |
|------|---|---|---|------------------|
| **K(1)** | 2/3 | 1/3 | 0.0458(1) | 0.0171(2) |
| **K(2)** | 0 | 0 | 0.1399(3) | 0.0239(3) |
| **Fe(1) ($Fe^{2+}$)** | 0 | 0 | 0 | 0.0102(2) |
| **Fe(2) ($Fe^{3+}$)** | 1/3 | -1/3 | 0.0847(1) | 0.0105(1) |
| **F(1)** | 0.6507(2) | -0.1747(1) | 0.0403(1) | 0.0212(4) |
| **F(2)** | 0.4901(1) | -0.0119(3) | 0.1184(3) | 0.0214(3) |

[a] $U_{eq}$ is defined as one-third of the trace of the orthogonal $U_{ij}$ tensor.

**Table 4.3** Selected Bond Distances and Angles for $K_4Fe_3F_{12}$.

| Bond | Distance (Å) | Bond | Distance (Å) |
|---|---|---|---|
| **K(1) — F(1)** | 2.888(1) × 6 | **Fe(1) — F(1)** | 2.079(1) × 6 |
| **K(1) — F(1)** | 2.891(2) × 3 | **Fe(2) — F(1)** | 2.016(1) × 3 |
| **K(1) — F(2)** | 2.671(2) × 3 | **Fe(2) — F(2)** | 1.864(1) × 3 |
| **K(2) — F(2)** | 2.721(2) × 3 | **Fe(1) — Fe(2)** | 4.090(8) × 2 |
| **K(2) — F(2)** | 2.946(1) × 6 | **Fe(1) — Fe(2)** | 4.091(2) × 4 |
| | | **Fe(2) — Fe(2)** | 4.604(3) |

| | Angle (°) | | Angle (°) |
|---|---|---|---|
| **F(1) — Fe(1) — F(1)** | 86.83(5) | **F(2) — Fe(2) — F(2)** | 96.46(5) |
| **F(1) — Fe(1) — F(1)** | 93.17(5) | **F(1) — Fe(2) — F(2)** | 85.78(6) |
| **F(1) — Fe(1) — F(1)** | 180.0 | **F(1) — Fe(2) — F(2)** | 88.62(4) |
| | | **F(1) — Fe(2) — F(2)** | 172.35(6) |
| | | **Fe(1) — F(1) — Fe(2)** | 174.79(7) |

**Table 4.4** Bond valence analysis of the $K_4Fe_3F_{12}$[a].

| Atom | F(1) | F(2) | $\Sigma_{\text{cations}}$ |
|---|---|---|---|
| **K(1)** | $0.088^{[\times 6]}$ $0.087^{[\times 3]}$ | $0.159^{[\times 3]}$ | **1.27** |
| **K(2)** | - | $0.139^{[\times 3]}$ $^{[\times 2]}0.075^{[\times 6]}$ | **0.867** |
| **Fe(1)** | $0.314^{[\times 6]}$ | - | **1.88** |
| **Fe(2)** | $0.402^{[\times 3]}$ | $0.606^{[\times 3]}$ | **3.02** |
| $\Sigma_{\text{anions}}$ | **0.891** | **1.05** | |

[a] Bond valence sums calculated with the formula: $S_i = \exp[(R_0-R_i)/B]$, where $S_i$ = valence of bond "$i$", $R_0$ is a constant dependent on the bonded elements, $R_i$ is the bond length of bond $i$ and B=0.37. Left and right superscripts indicate the # of equivalent bonds for anions and cations, respectively.

# CHAPTER 5. Synthesis, Structure, and Characterization of Mixed Valence Manganese ($Mn^{2+}$/$Mn^{3+}$) Fluoride Materials, $Ba_3Mn_3F_{14}$ and $NaBa_7Mn_7F_{34}$

## 5.1 Abstract

New mixed valence manganese ($Mn^{2+}$/$Mn^{3+}$) fluoride materials, $Ba_3Mn_3F_{14}$ and $NaBa_7Mn_7F_{34}$ have been synthesized and characterized. Both materials were synthesized by hydrothermal method using $CF_3COOH$ aqueous solution. The aqueous solution of $CF_3COOH$ acted as a reducing agent, and reduce some of the $Mn^{3+}$ to $Mn^{2+}$ during hydrothermal reaction. The amount of $CF_3COOH$ also played an important role for controlling the reduction process. $Ba_3Mn_3F_{14}$ exhibits a chain structure consisting of separate edge-shared $Mn^{2+}F_6$ trigonal prisms and corner-shared $Mn^{3+}F_6$ distorted octahedra that run along the $b$-direction. $NaBa_7Mn_7F_{34}$ exhibits a Jarlite-type structure consisting of corner-shared $Mn^{2+}F_6$, ($Mn^{2+}$/$Mn^{3+}$)$F_6$ and $Mn^{3+}F_6$ distorted octahedra, which forms infinite helicoidal double-chains along the $b$-axis. In addition to single-crystal diffraction data, magnetic measurements, infrared, UV-vis, thermogravimetric analysis measurements were carried out. Crystal data: $Ba_3Mn_3F_{14}$, orthorhombic, space group *Pnma* (No. 62), $a = 27.272(2)$, $b = 5.6613(4)$, $c = 7.4711(6)$ Å, $V = 1153.51(15)$ Å$^3$, $Z = 4$, $T = 296(2)$ K; $NaBa_7Mn_7F_{34}$, Monoclinic, space group *C2/m* (No. 12), $a = 16.961(9)$, $b = 11.551(6)$, $c = 7.651(4)$ Å, $\beta = 101.785(12)°$, $V = 1467.4(13)$ Å$^3$, $Z = 2$, $T = 296(2)$ K.

## 5.2 Introduction

Manganese fluoride materials have been investigated extensively because of their important magnetic, electric, multi-ferroic and optical properties.[1] For example, $BaMnF_4$ exhibits multi-ferroic behavior, as well as non-linear optical properties.[2-4] Recently, $Li_2MnF_5$ was suggested to be a promising Li-ion cathode material.[5] Manganese(III) fluoride materials have been often observed in low-dimensional crystal structures attributable to the strong first-order Jahn-Teller distortion of $Mn^{3+}(d^4)$.[6-8] These materials, e.g., $A_3MnF_6$ ($A^+$ = Li, Na, K, Rb, Cs, and $NH_4$),[6,8] $A_2MnF_5$ ($A^+$ = Li, Na, Rb, Cs, and $NH_4$),[9-13] $AMnF_4$ ($A^+$ = Li, Na, K, Rb, Cs, and Tl)[14-21] and $BMnF_5$ ($B^{2+}$ = Ca, Ba, and Cd)[22-23] exhibit isolated, chains or layers of corner-shared $Mn^{3+}F_6$ octahedra.

Among the large number of manganese fluoride compounds, mixed valence manganse ($Mn^{2+}/Mn^{3+}$) fluoride compounds are extremely rare and have not been fully investigated owing to difficulties of preparation and controlling the oxidation state of manganese.[8] In fact, only three mixed valence manganese ($Mn^{2+}/Mn^{3+}$) fluoride materials have been reported; $CsMn_2F_6$ ($CsMn^{2+}Mn^{3+}F_6$), $K_4Mn_3F_{12}$ ($K_4Mn^{2+}(Mn^{3+})_2F_{12}$) and $Mn_3F_8 \cdot 12H_2O$ ($[Mn^{2+}(H_2O)_6][Mn^{3+}(H_2O)_2F_4]_2 \cdot 2H_2O$).[8,24-26] $CsMn_2F_6$ ($CsMn^{2+}Mn^{3+}F_6$) is expected to have a modified pyrochlore structure, similar to $NH_4Fe_2F_6$ ($NH_4Fe^{2+}Fe^{3+}F_6$). To date, however, no crystal structure has been reported.[8,24] $K_4Mn_3F_{12}$ ($K_4Mn^{2+}(Mn^{3+})_2F_{12}$) exhibits a cation-deficient perovskite structure stabilized by the Jahn-Teller effect.[25] This material was synthesized through a solid state reaction using $KMn(II)F_3$ and $K_2Mn(IV)F_6$.[25] $Mn_3F_8 \cdot 12H_2O$ ($[Mn^{2+}(H_2O)_6][Mn^{3+}(H_2O)_2F_4]_2 \cdot 2H_2O$) exhibits a complex

hydrogen bond network between $[Mn(H_2O)_6]^{2+}$ cations and Jahn-Teller distorted $[Mn(H_2O)_2F_4]^-$ anions.[26]

In order to achieve the synthesis of new mixed valence manganese fluoride materials, a new synthetic method was required. We recently reported on the synthesis and characterization of a new charge-ordered $Fe^{2+}/Fe^{3+}$ fluoride material, $RbFe_2F_6$ ($RbFe^{2+}Fe^{3+}F_6$).[27] This material was synthesized through a mild hydrothermal method using $CF_3COOH$.[28] In this chapter, utilizing a similar synthetic technique, we report the synthesis of new, charge ordered, mixed valence $Mn^{2+}/Mn^{3+}$ fluoride materials, $Ba_3Mn_3F_{14}$ and $NaBa_7Mn_7F_{34}$ In addition to the crystal structures, characterization and magnetic measurements are reported.

## 5.3 Experimental Section

### 5.3.1 Reagents.

NaF (Alfa Aesar, 98 %), $BaF_2$ (Aldrich, 99.99 %), $MnF_3$ (Alfa Aesar, 98 %), and $CF_3COOH$ (Alfa Aesar, 99%) were used without any further purification.

### 5.3.2 Synthesis.

$Ba_3Mn_3F_{14}$ and $NaBa_7Mn_7F_{34}$ were obtained by hydrothermal methods using a diluted $CF_3COOH$ solution. Crystals of $Ba_3Mn_3F_{14}$ were grown by mixing 0.0894 g ($5.10\times10^{-4}$ mol) of $BaF_2$, 0.1556g ($1.39\times10^{-3}$ mol) of $MnF_3$, and 2 ml ($2.60\times10^{-2}$ mol) of $CF_3COOH$ with 5 ml of $H_2O$. Crystals of $NaBa_7Mn_7F_{34}$ were grown by mixing 0.0214 g ($5.10\times10^{-4}$ mol) of NaF, 0.0894 g ($5.10\times10^{-4}$ mol) of $BaF_2$, 0.1556g ($1.39\times10^{-3}$ mol) of $MnF_3$, and 2 ml ($2.60\times10^{-2}$ mol) of $CF_3COOH$ with 5 ml of $H_2O$. The resultant solutions were placed

in 23-mL Teflon-lined stainless autoclaves that were subsequently closed. The autoclaves were gradually heated to 230 ºC, held for 24 h, and cooled slowly to room temperature at a rate 6 ºC h$^{-1}$. The mother liquor was decanted from the products, and products were recovered by filtration and washed with distilled water and acetone. For $Ba_3Mn_3F_{14}$, light brown colored rod-shaped crystals, the only product from the reaction, was recovered in approximately 30 % yield based on $MnF_3$. For $NaBa_7Mn_7F_{34}$, mainly dark brown colored plate-shaped crystals, and some transparent crystals of $MnF_2$ were recovered. Transparent crystals of $MnF_2$ were removed by hand-sorting. The yield was approximately 10 % yield based on $MnF_3$. The powder X-ray diffraction pattern on the synthesized phase is in good agreement with the generated pattern from the single-crystal data.

## 5.4 Results and Discussion

**Synthesis.** The hydrothermal reaction of $BaF_2$ and $MnF_3$ in an aqueous solution of $CF_3COOH$ results in the formation of $Ba_3Mn_3F_{14}$, with some of the $Mn^{3+}$ cations reduced to $Mn^{2+}$. It is thought that the aqueous solution of $CF_3COOH$ is acting as a reducing agent. In order to investigate this, hydrothermal reactions were performed where the amount of $CF_3COOH$ was increased. The original reaction that produced $Ba_3Mn_3F_{14}$ had 2 ml of $CF_3COOH$ in 5 ml of $H_2O$. Separate reactions were performed where the amount of $CF_3COOH$ was increased to 3 ml, 4 ml, and 5 ml, with the $H_2O$ volume remaining at 5 ml. As seen in Figure 5.3, as the amount of $CF_3COOH$ is increased, additional products containing $Mn^{2+}$ are formed. These products include

BaMnF$_4$ and MnF$_2$. In fact, when the amount of CF$_3$COOH is increased to 5 ml, the majority phases in the mixture are only BaMnF$_4$ and MnF$_2$. These experiments strongly suggest that the aqueous CF$_3$COOH solution acts as a reducing agent, and reduces some of the Mn$^{3+}$ to Mn$^{2+}$.

Similarly, the hydrothermal reaction of NaF, BaF$_2$, and MnF$_3$ in aqueous solution of CF$_3$COOH results in the formation of NaBa$_7$Mn$_7$F$_{34}$, with some of the Mn$^{3+}$ cations reduced to Mn$^{2+}$. In fact, additional MnF$_2$ was also formed. Adding NaF induced further reduction of Mn$^{3+}$ to Mn$^{2+}$ and this is because in situ CF$_3$COONa was generated during hydrothermal reaction, it reacts as a buffer, thus it helps to reduce Mn$^{3+}$ to Mn$^{2+}$.
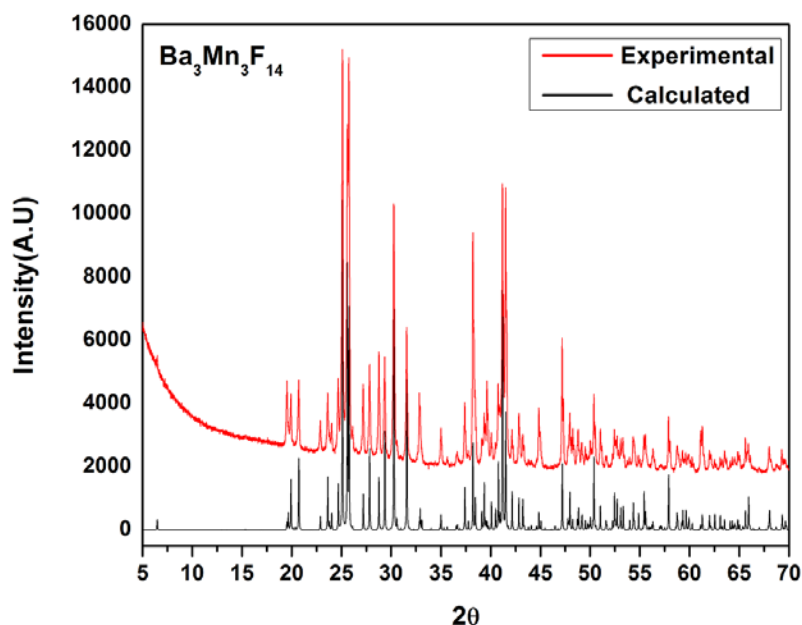


**Figure 5.1** Experimental and calculated powder X-ray diffraction patterns for Ba$_3$Mn$_3$F$_{14}$.
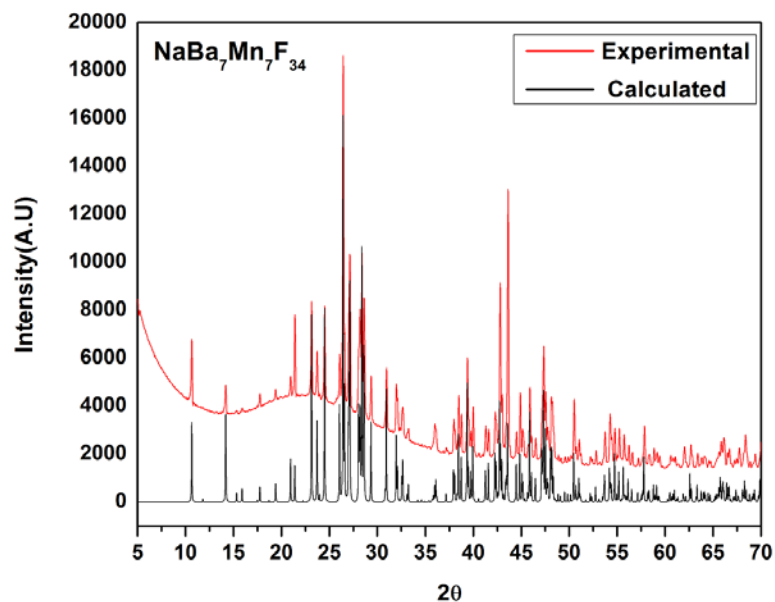
**Figure 5.2** Experimental and calculated powder X-ray diffraction patterns for $NaBa_7Mn_7F_{34}$.
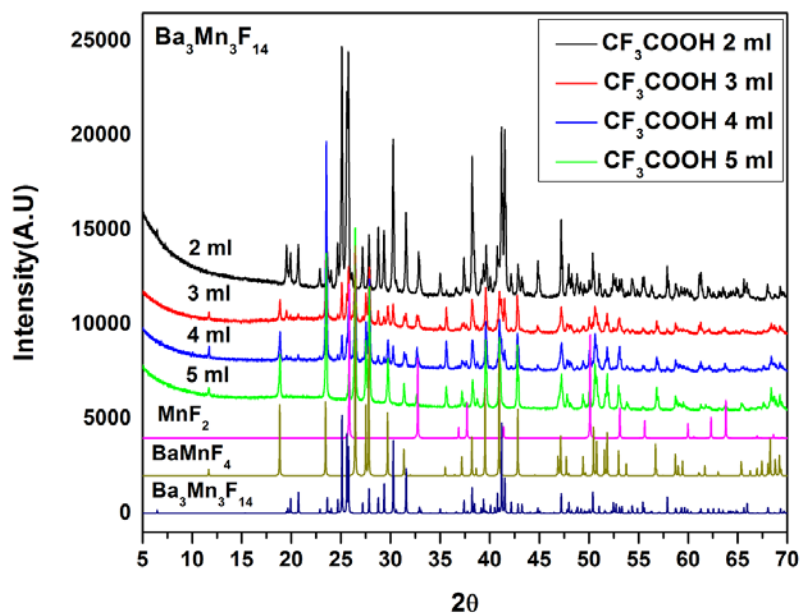


**Figure 5.3** Experimental powder X-ray diffraction patterns for samples using the different amount of $CF_3COOH$ (2 ml, 3 ml, 4 ml, and 5 ml) for $Ba_3Mn_3F_{14}$.

**Structure.** The room temperature structure of $Ba_3Mn_3F_{14}$ was determined to be in the

*P*nma space group, with lattice parameters of $a = 27.272(2)$ Å, $b = 5.6613(4)$ Å, $c =$

7.4711(6) Å. One structurally related complex fluoride compound, $Ba_3CuGa_2F_{14}$ was

known.[29] This material was reported in the pseudo-orthorhombic space group, $P2_1/n$

with the lattice parameter of $a = 7.402(3)$ Å, $b = 27.88(1)$ Å, $c = 5.521(2)$ Å, and $\beta =$

90.12(3)°.[29]

$Ba_3Mn_3F_{14}$ exhibits a chain structure consisting of separate edge-shared $Mn^{2+}F_6$ trigonal

prisms and corner-shared $Mn^{3+}F_6$ distorted octahedra that run along the *b*-direction

(Figure 5.4 and 5.5). Both chains are separated by $Ba^{2+}$ cations. The formula may be also

written as $Ba_3(Mn^{2+})(Mn^{3+})_2F_{14}$, and explicitly describes the charge ordering between

the $Mn^{2+}$ and $Mn^{3+}$ cations. The material has three crystallographically unique

manganese sites, one of which contains an one $Mn^{2+}$ and the other two of which each

contain one $Mn^{3+}$ cation. In connectivity terms, the structure may be written as

$((Mn^{2+}F_{2/1}F_{1/2}F_{1/2}F_{1/2}F_{1/2})^{2-}(Mn^{3+}F_{4/1}F_{1/2}F_{1/2})^{2-}(Mn^{3+}F_{4/1}F_{1/2}F_{1/2})^{2-})^{6-}$ where charge balance

is retained by three $Ba^{2+}$ cations. The $Mn^{2+}$ - F bond distances range between 2.103(3) -

2.143(3) Å, with an $Mn^{2+}$ - F - $Mn^{2+}$ bond angle of 106.17(13)° (Figure 5.6a).

Interestingly, the edge-shared $Mn^{2+}F_6$ trigonal prism is the first time observed. Although

other edge-shared $MF_6$ (M = $Cr^{2+}$ and $Cu^{2+}$) trigonal prisms were reported,[29-31] those

cations are first-order Jahn-Teller cations, which can sometimes adopt unusual

coordinations. However, $Mn^{2+}$ is not a first-order Jahn-Teller cation and it adopts mostly

corner-shared or edge-shared octahedral environment. The Jahn-Teller like character of

$Mn^{2+}$ (two short and four long bond distances) and its unusual coordination environment

in the structure should come from the reduction of $Mn^{3+}$ to $Mn^{2+}$ during the synthesis. The $Mn^{3+}$ - F bond distances range between 1.805(5) - 2.270(6) Å, with $Mn^{3+}$ - F - $Mn^{3+}$ bond angles of 139.0(2)° and 140.2(2)° (Figure 5.6b). It is important to note that two $Mn^{3+}$ cations are connected with disordered fluorine (F9a or F9b), thus a first-order Jahn-Teller distortion of $Mn^{3+}$ could not be clearly observed such as an elongation or compression of the $Mn^{3+}F_6$ octahedra. The $Ba^{2+}$ cations are in 12-fold coordination environments with $Ba^{2+}$ - F distances that range between 2.697(3) - 3.056(4) Å. Bond valence calculations[32-34] (Table 5.6) resulted in values of 1.96-1.99, 1.87, 3.07 and 0.932-1.05 for $Ba^{2+}$, $Mn^{2+}$, $Mn^{3+}$ and F⁻, respectively.
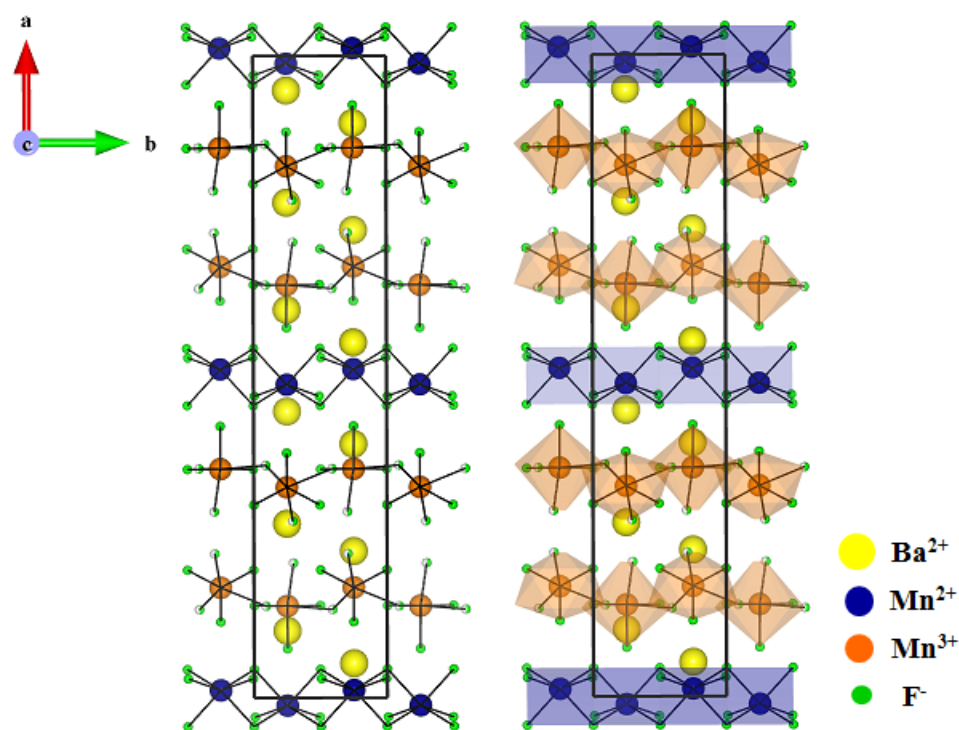


**Figure 5.4** Ball-and-stick and polyhedral representations for $Ba_3Mn_3F_{14}$ in the *ab*-plane.
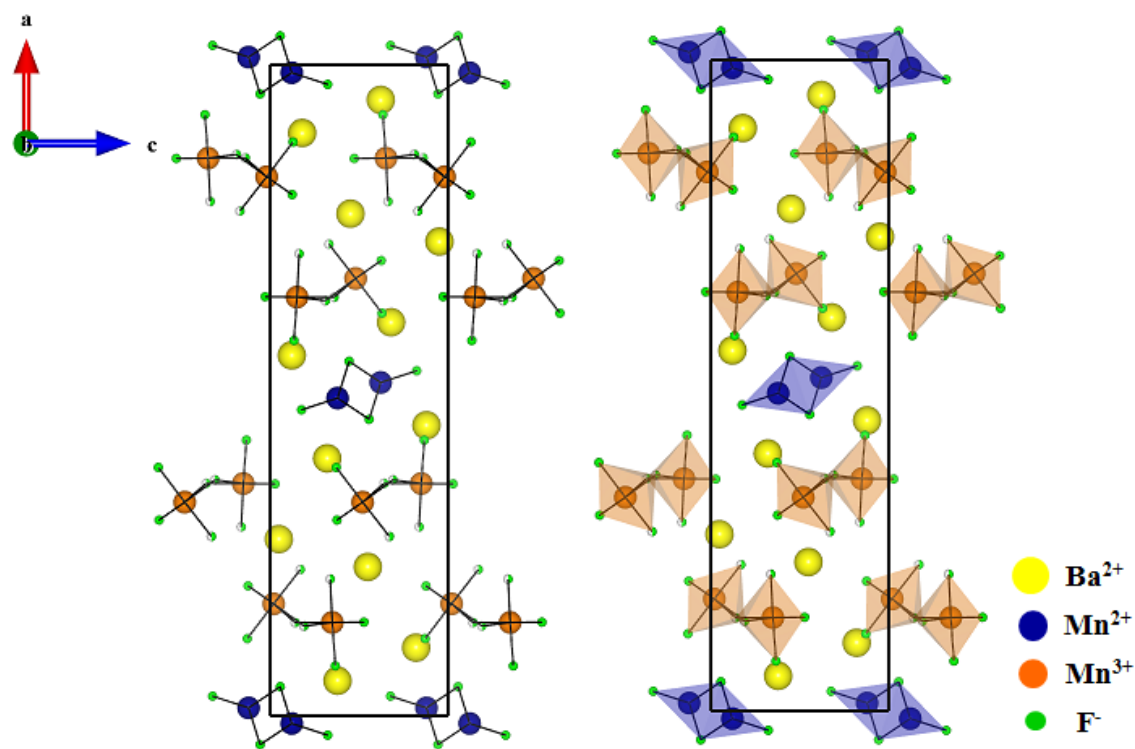
**Figure 5.5** Ball-and-stick and polyhedral representations for Ba$_3$Mn$_3$F$_{14}$ in the *ac*-plane.
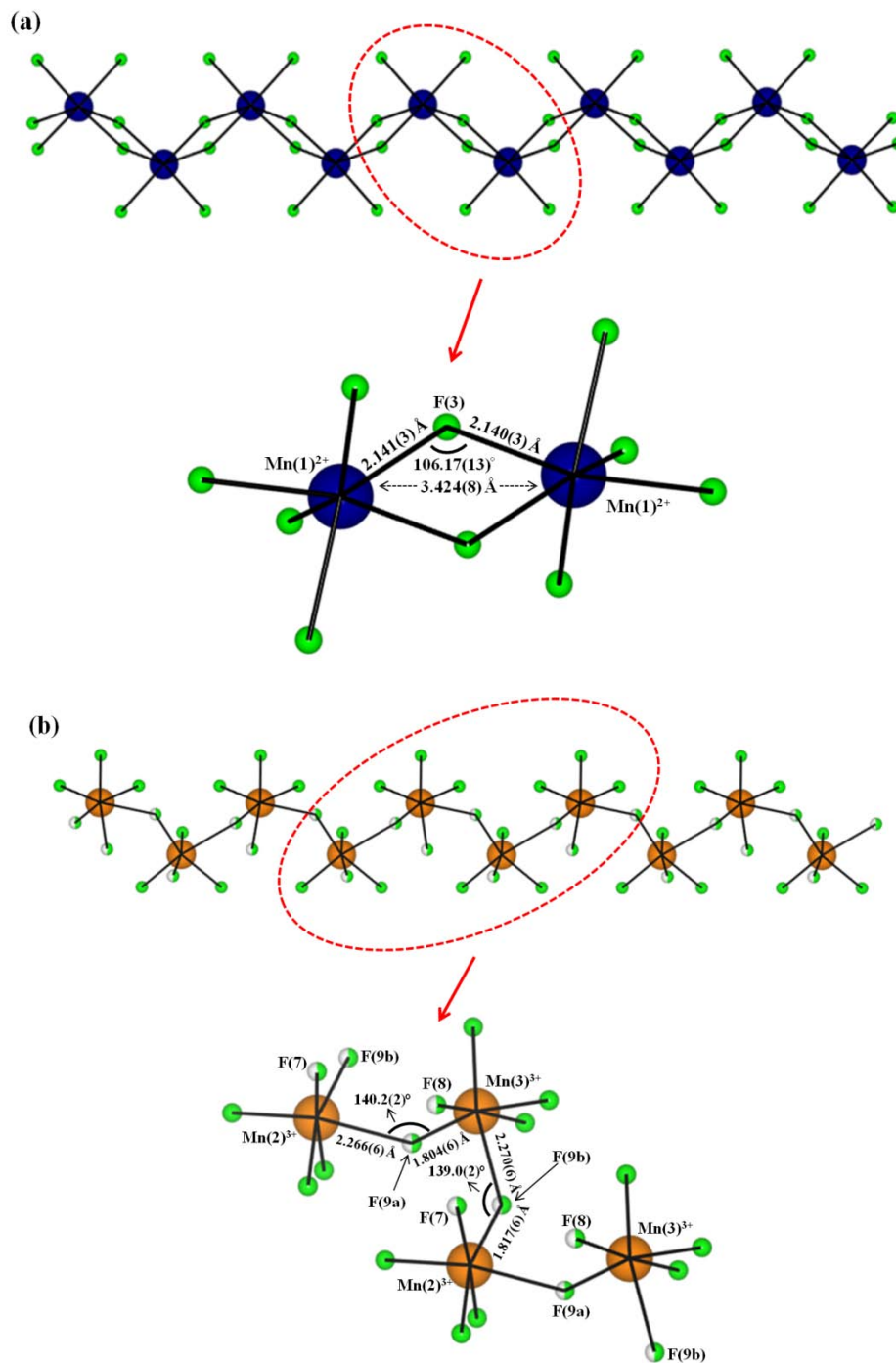
**Figure 5.6** Ball-and-stick diagrams for (a) zigzag chain of edge-sharing $Mn^{2+}F_6$ trigonal prism (blue) and (b) cis-chain of corner-sharing $Mn^{3+}F_6$ octahedra (orange) along the *b*-direction, respectively, from the crystal structure of $Ba_3Mn_3F_{14}$.

The room temperature structure of $NaBa_7Mn_7F_{34}$ was determined to be in the $C2/m$ space group, with lattice parameters of $a$ = 16.961(9), $b$ = 11.551(6), $c$ = 7.651(4) Å, $\beta$ = 101.785(12)°. This phase is strongly related to the Jarlite-type structure, which was from the mineral, $Na(Sr_6Na)MgAl_6F_{32}(OH)_2$.[35] Inspired by this crystal structure, magnetic cations substituted isostructural Fe analogues were also reported, e.g., $Ba_7MFe_6F_{34}$ ($M^{2+}$ = $Mn^{2+}$, $Fe^{2+}$, $Cu^{2+}$), $Ba_7Fe_6F_{32}\cdot2H_2O$, and $Pb_7Fe_7F_{34}$.[36-40] The difference between Fe analogues and $NaBa_7Mn_7F_{34}$ is that the empty 2b site is occupied by a $Na^+$ cation, thus one of manganese sites is disordered with $Mn^{2+}$ and $Mn^{3+}$.

$NaBa_7Mn_7F_{34}$ exhibits a chain structure consisting of corner-shared $Mn^{2+}F_6$, $(Mn^{2+}/Mn^{3+})F_6$ and $Mn^{3+}F_6$ distorted octahedra, which forms infinite helicoidal double-chains along the $b$-axis (Figure 5.7). Chains are separated by $Ba^{2+}$ cations. The formula may be also written as $NaBa_7(Mn^{2+})(Mn^{2+}/Mn^{3+})_2(Mn^{3+})_4F_{34}$, as the $Mn^{2+}$, $(Mn^{2+}/Mn^{3+})$, and $Mn^{3+}$ cations are ordered in the structure. The material has three crystallographically unique manganese sites, that contain $Mn^{2+}$, $(Mn^{2+}/Mn^{3+})$, and $Mn^{3+}$ cations, respectively. In connectivity terms, the structure may be written as $((Mn^{2+}F_{2/1}F_{1/2}F_{1/2}F_{1/2})^{2-}$ $(2((Mn^{2+}/Mn^{3+})F_{4/1}F_{1/2}F_{1/2}))^{5-}(4(Mn^{3+}F_{4/1}F_{1/2}F_{1/2}))^{8-})^{15-}$ where charge balance is retained by one $Na^+$ and seven $Ba^{2+}$ cations. The $Mn^{2+}$ - F bond distances range between 2.123(3) - 2.139(3) Å, $(Mn^{2+}/Mn^{3+})$ - F bond distance range between 1.887(8) - 2.081(6) Å, and $Mn^{3+}$ - F bond distance range between 1.822(3) - 2.106(3) Å. It is important to note that $Mn^{3+}$ and $(Mn^{2+}/Mn^{3+})$ cations are connected with disordered fluorine (F10a or F10b), thus a first-order Jahn-Teller distortion of $Mn^{3+}$ could not be clearly observed such as an elongation or compression of $Mn^{3+}F_6$ octahedra. The bond angle of $Mn^{2+}$ - F - $Mn^{3+}$ is

136.48(2)° and bond angle of $(Mn^{2+}/Mn^{3+})$ - F - $Mn^{3+}$ are 134.1(3)° and 137.3(5)°, respectively. The $Na^+$ cation is in 6-fold coordination environment with $Na^+$ - F distances that range between 2.188(4) - 2.498(3) Å and the $Ba^{2+}$ cations are in 9 to 11-fold coordination environments with $Ba^{2+}$ - F distances that range between 2.625(3) - 3.214(4) Å. Bond valence calculations[32-34] (Table 5.7) resulted in values of 0.938, 1.87-2.09, 1.85, 2.47, 2.93 and 0.869-1.26 for $Na^+$, $Ba^{2+}$, $Mn^{2+}$, $(Mn^{2+}/Mn^{3+})$, $Mn^{3+}$ and F$^-$, respectively.
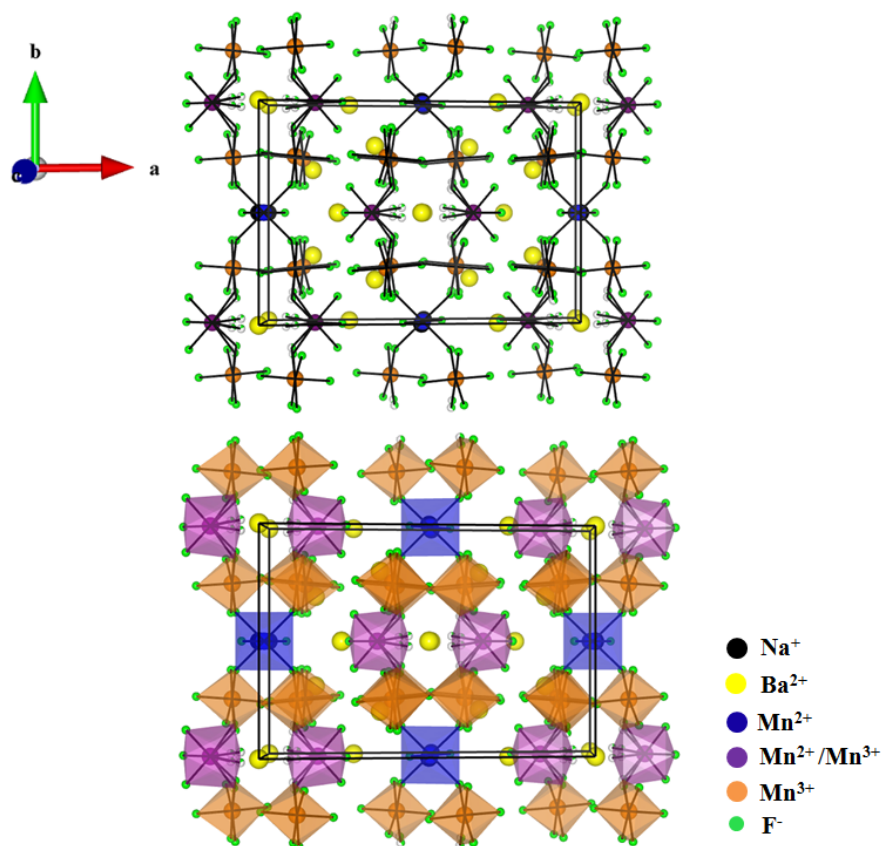


**Figure 5.7** Ball-and-stick and polyhedral representation for $NaBa_7Mn_7F_{34}$ in the *ab*-plane.
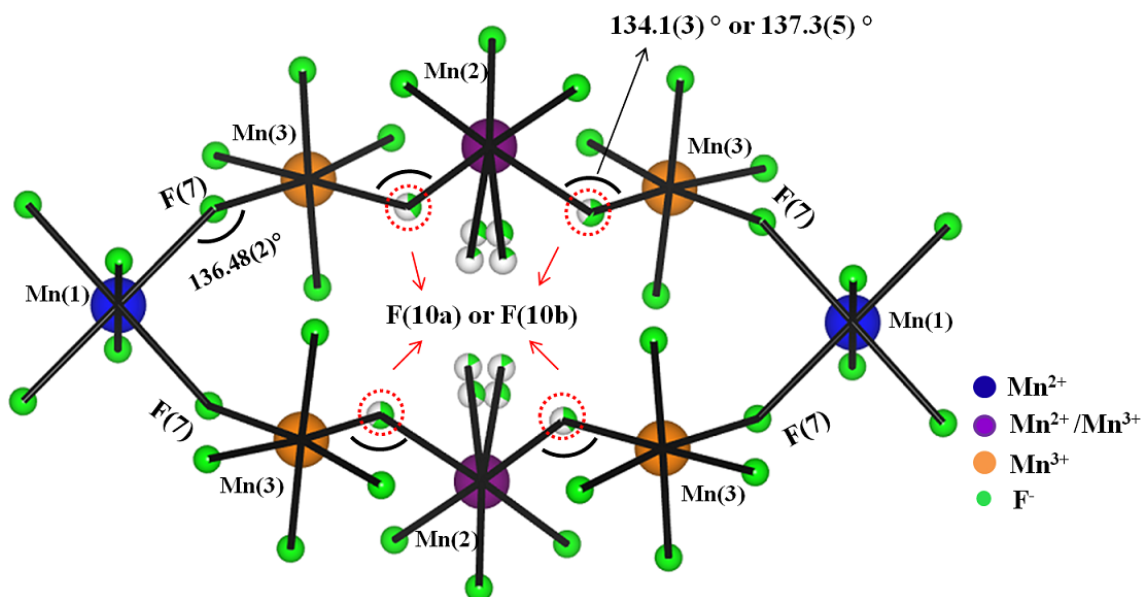
**Figure 5.8** Ball-and-stick diagram for one dimensional magnetic ring chain in $NaBa_7Mn_7F_{34}$.

**Infrared Spectroscopy.** The FT-IR spectra of $Ba_3Mn_3F_{14}$ and $NaBa_7Mn_7F_{34}$ revealed Mn-F and Ba-F vibrations between 1000 and 400 $cm^{-1}$ (Figure 5.11). The bands occurring between 650 – 450 $cm^{-1}$ and 450 – 400 $cm^{-1}$ can be assigned to Mn – F and Ba – F vibrations, respectively. These assignments are consistent with previous reports.[41-43]

**Ba(1)**            **Ba(2)**            **Ba(3)**

**Mn(1)**            **Mn(2)**            **Mn(3)**
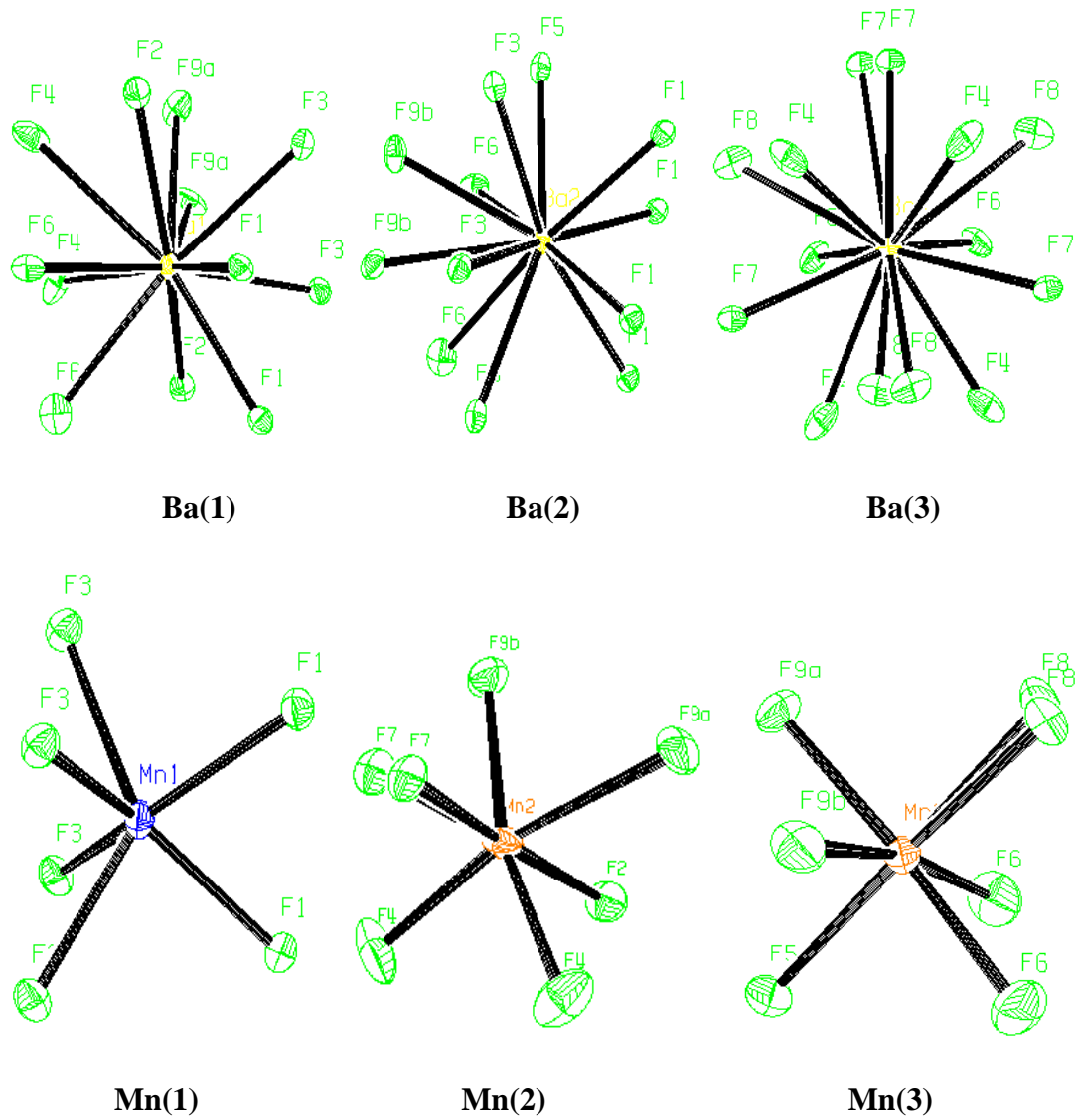
**Figure 5.9** ORTEP (50% probability ellipsoids) diagrams for $Ba_3Mn_3F_{14}$.
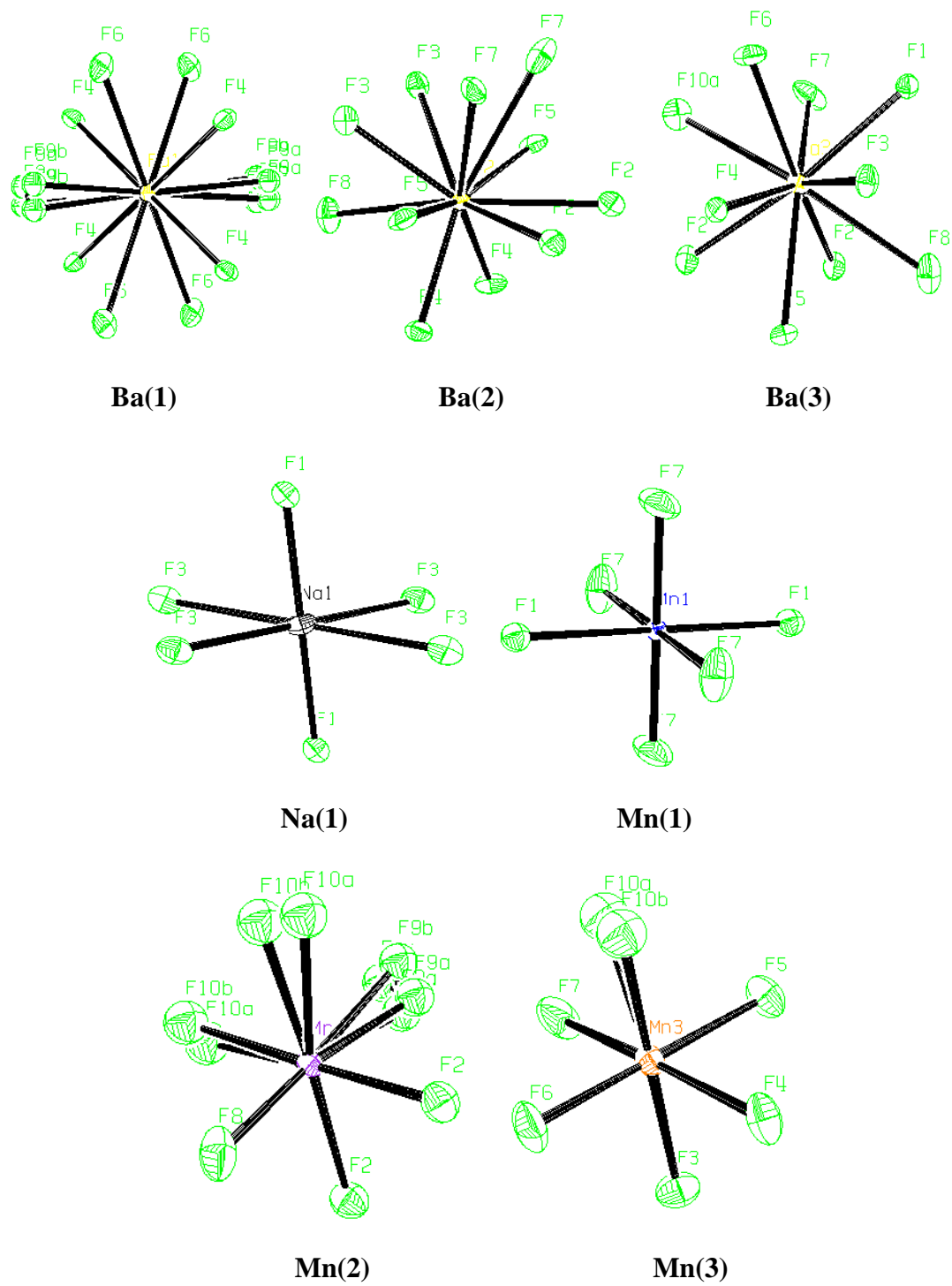
**Figure 5.10** ORTEP (50% probability ellipsoids) diagrams for NaBa$_7$Mn$_7$F$_{34}$.
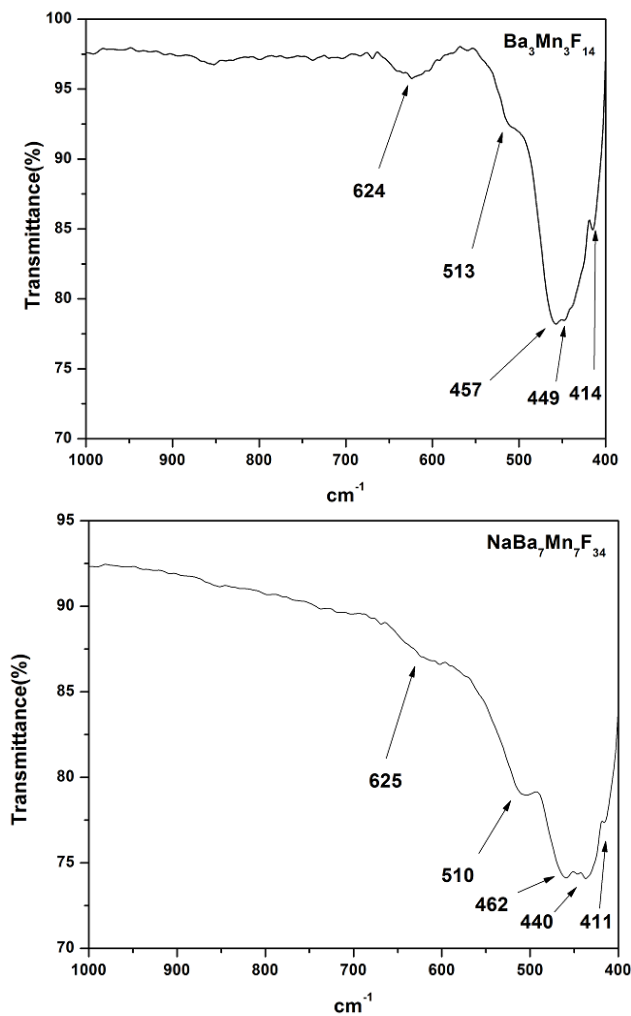
| Ba₃Mn₃F₁₄ | | NaBa₇Mn₇F₃₄ | |
|---|---|---|---|
| $\upsilon$(Mn-F) | $\upsilon$(Ba-F) | $\upsilon$(Mn-F) | $\upsilon$(Ba-F) |
| 624 | 449 | 625 | 440 |
| 513 | 414 | 510 | 411 |
| 457 | | 462 | |

**Figure 5.11** IR spectra and assignment for Ba₃Mn₃F₁₄ and NaBa₇Mn₇F₃₄.[41-43]

**UV-Vis Diffuse Reflectance Spectroscopy.** The UV-Vis diffuse reflectance spectra was measured on ground crystals of $Ba_3Mn_3F_{14}$ and $NaBa_7Mn_7F_{34}$ and the band gap energy of $Ba_3Mn_3F_{14}$ and $NaBa_7Mn_7F_{34}$ have been determined from the reflectance spectra using the Kubelka-Munk function[44] and the Tauc plot.[45]

From the Tauc plot of $[F(R)eV]^{1/2}$ versus eV for $Ba_3Mn_3F_{14}$ and $NaBa_7Mn_7F_{34}$, the optical band gaps of $Ba_3Mn_3F_{14}$ and $NaBa_7Mn_7F_{34}$ are estimated to be approximately 2.01 eV and 1.72 eV, respectively, which are consistent with the brown colors of the materials (See Figure 5.12 and Figure 5.13). For both compounds, two broad bands were observed in absorption spectra. One broad band near 350 nm was possibly attributable to metal to ligand charge transfer.[46-47] Another broad band near 500 nm was attributed to d-d transition of Mn cations.[46-47]


**Thermal Analysis.** The thermal behavior of $Ba_3Mn_3F_{14}$ and $NaBa_7Mn_7F_{34}$ was investigated using thermogravimetric analysis (TGA) under nitrogen atmosphere (See Figure 5.14). Both compounds are thermally stable to around 350 °C. Above this temperature, the materials decompose to $BaF_2$, $BaMnF_4$ and unknown phases. The final residue products were confirmed by PXRD (See Figure 5.15).
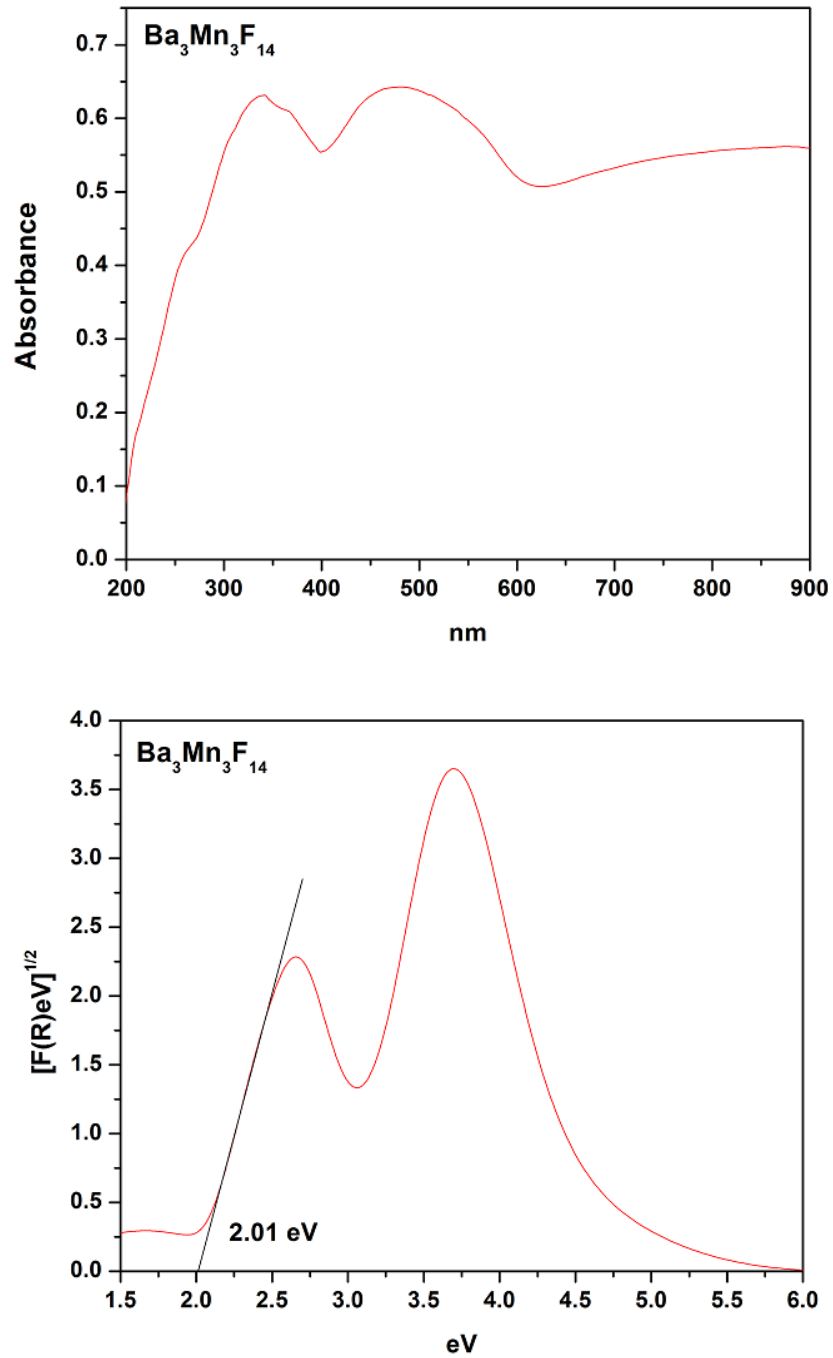
**Figure 5.12** The UV-Vis diffuse reflectance spectra (top) and the Tauc plot of $[F(R)eV]^{1/2}$ versus eV (bottom) for $Ba_3Mn_3F_{14}$.
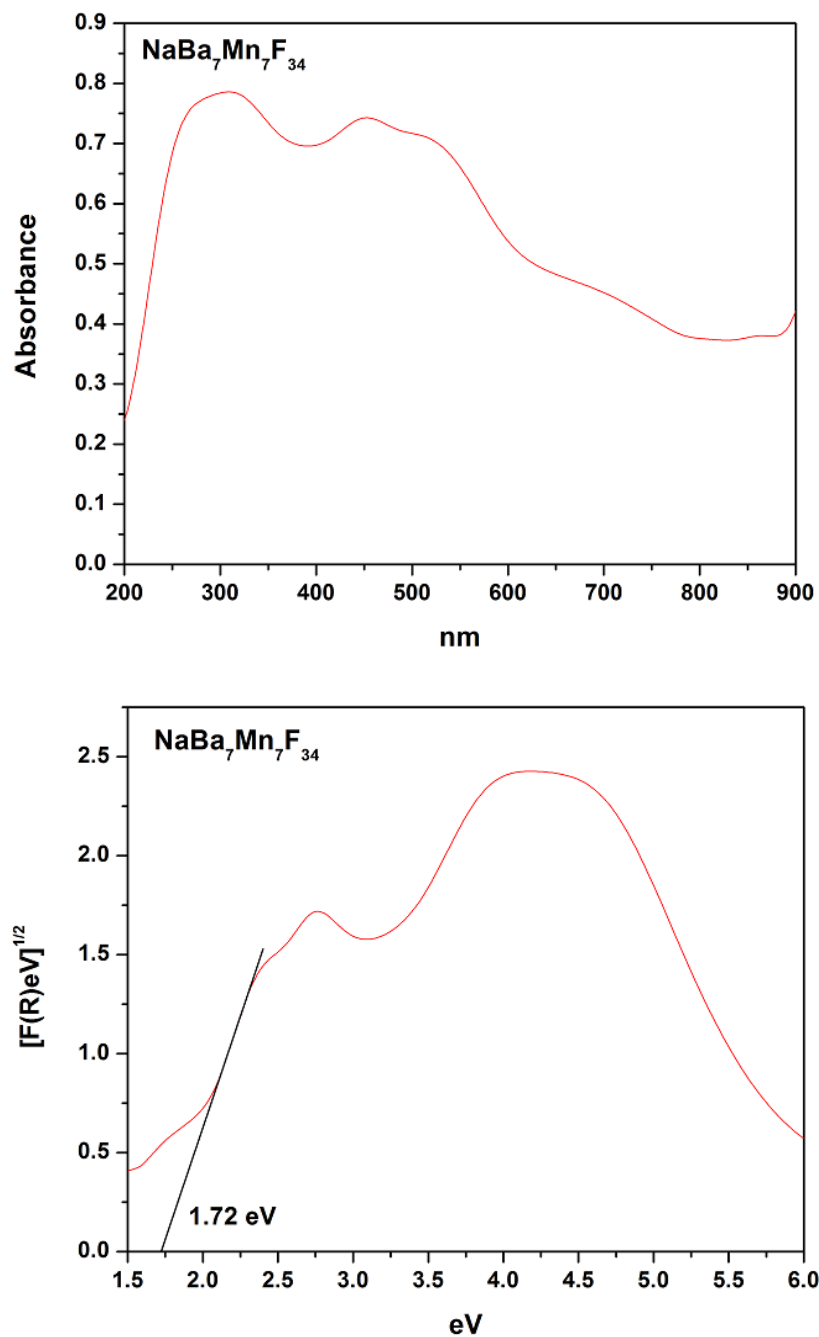
**Figure 5.13** The UV-Vis diffuse reflectance spectra (top) and the Tauc plot of $[F(R)eV]^{1/2}$ versus eV (bottom) for $NaBa_7Mn_7F_{34}$.
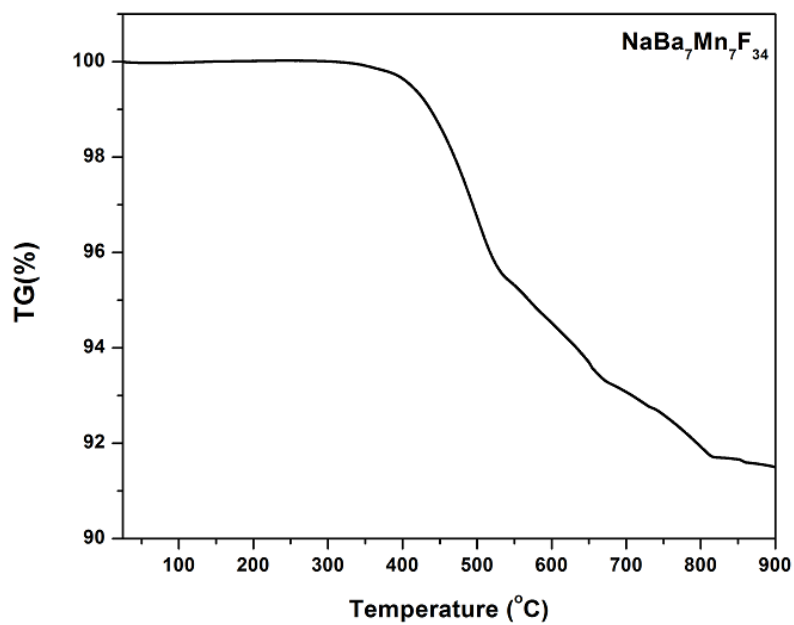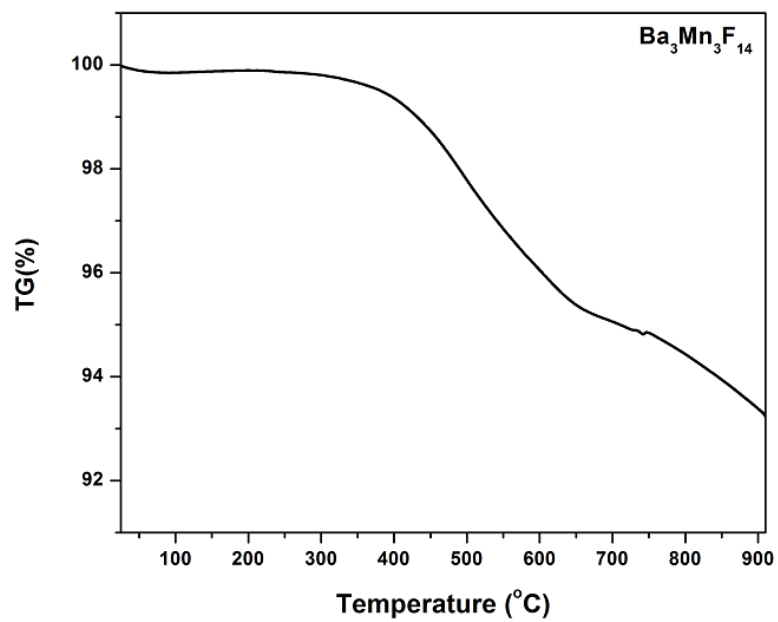
**Figure 5.14** Thermogravimetric analysis (TGA) diagram for $Ba_3Mn_3F_{14}$ (top) and $NaBa_7Mn_7F_{34}$ (bottom).
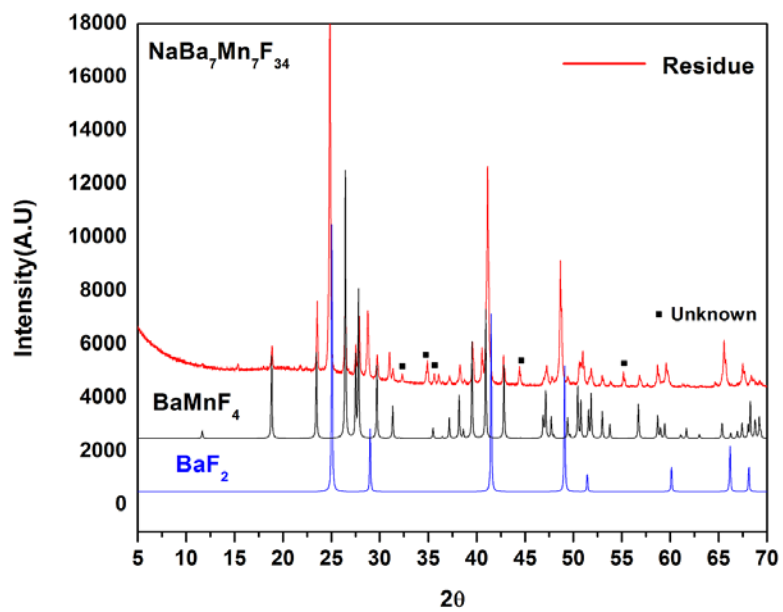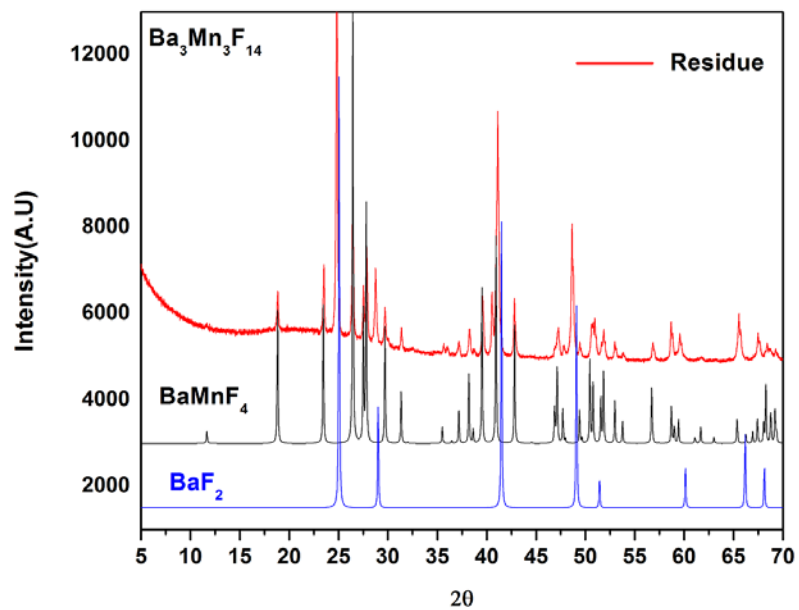
**Figure 5.15** Powder X-ray diffraction data for final residuals after TGA experiment: $Ba_3Mn_3F_{14}$ (top) and $NaBa_7Mn_7F_{34}$ (bottom).

**Magnetic Property** The dc magnetic susceptibility of $Ba_3Mn_3F_{14}$ was measured under 500 Oe in the temperature range 2-300 K and is shown as $\chi$ and $\chi^{-1}$ versus T plots in Figure 5.16a and Figure 5.16b, respectively. $Ba_3Mn_3F_{14}$ exhibited anti-ferromagnetic behavior with a Néel temperature of 7 K. There was no divergence between ZFC (Zero field cooled) and FC (Field cooled) magnetization curve above a Néel temperature, however, below a Néel temperature slightly divergence between ZFC and FC magnetization curve was observed. From the inverse susceptibility versus temperature shown in Figure 5.16b, the susceptibility data were fit to the Curie-Weiss law, $\chi = C / (T - \theta)$ for T > 50 K, where C is the Curie constant and $\theta$ is the Weiss constant. The Curie constant is 10.93 emu K mol$^{-1}$ and the Weiss constant is -12.44 K, which are extracted from the curve fitting. On the basis of fit, the effective magnetic moment is 5.40 $\mu_B$/f.u, which is slightly higher than the theoretical spin only value of 5.26 $\mu_B$/f.u. ($Mn^{2+}$ = 5.9 $\mu_B$ and $Mn^{3+}$ = 4.9 $\mu_B$). This difference could be explained by the orbital contribution of the Mn(III) cations. A small negative Weiss constant indicates weak anti-ferromagnetic interactions between Mn moments.

The magnetic interactions in $Ba_3Mn_3F_{14}$ could be classifies two types: a) intra-chain interactions between $Mn^{2+}$ and $Mn^{2+}$ or between $Mn^{3+}$ and $Mn^{3+}$ along the *b*-direction and b) inter-chain interactions between the $Mn^{2+}$- F - $Mn^{2+}$ chain and the $Mn^{3+}$ - F - $Mn^{3+}$ chain along the *a*-direction or between the two $Mn^{3+}$ - F - $Mn^{3+}$ chains along the *a*- or c-direction.

The intra-chain interactions take place through two possible super-exchange pathways: 1) a 90°-type super-exchange path via two fluoride ions bridges of edge-shared trigonal

prisms ($Mn(1)^{2+}$ - F - $Mn(1)^{2+}$) and 2) a 180°-type super-exchange path via bridging disordered fluorine ions of corner-shared distorted octahedra ($Mn(2)^{3+}$ - F - $Mn(3)^{3+}$ or $Mn(3)^{3+}$ - F - $Mn(2)^{3+}$).

The $Mn^{2+}(d^5)$ - $Mn^{2+}(d^5)$ interaction via 90°-type super-exchange paths in fluoride materials have not been studied well. There are very few examples, and those studies are only one, in which $Mn^{2+}$ cations located in edge-shared octahedra such as $MnF_2$, and $MnAlF_5$ and $BaMnFeF_7$.[48-51] In case of $MnF_2$ and $BaMnFeF_7$, ferromagnetic interaction was suggested and $MnAlF_5$ showed anti-ferromagnetic interaction. From consideration of the bond angle of $Mn^{2+}$ - F - $Mn^{2+}$ in these compounds (101.9° for $MnF_2$, 107.4° for $MnAlF_5$, and 100.2° for $BaMnFeF_7$), this results were quite consistent with Goodenough-Kanamori rule.[52-54] The bond angle of $Mn^{2+}$ - F - $Mn^{2+}$ in $Ba_3Mn_3F_{14}$ is 106.17(13)°, thus the $Mn^{2+}(d^5)$ - $Mn^{2+}(d^5)$ interaction in $Ba_3Mn_3F_{14}$ could be expected anti-ferromagnetic interactions attributable to the previous results.

The $Mn^{3+}(d^4)$ - $Mn^{3+}(d^4)$ interaction via 180°-type super-exchange paths in fluoride materials was well studied, and lead to anti-ferromagnetic coupling according to the Goodenough-Kanamori rule.[52-54] The bond angles of $Mn^{3+}$ - F - $Mn^{3+}$ in $Ba_3Mn_3F_{14}$ are 139.0(2)° and 140.2(2)°, respectively, thus the $Mn^{3+}(d^4)$ - $Mn^{3+}(d^4)$ interaction in $Ba_3Mn_3F_{14}$ could be expected anti-ferromagnetic interaction.

Isothermal magnetization of $Ba_3Mn_3F_{14}$ was measured at 2 K (below $T_N$) and 10 K (above $T_N$) as a function of applied field H are shown in Figure 5.17. The linear magnetization vs. field H was observed at 10 K and the magnetization vs. field H at 2 K showed the appearance of spin flop transition at the field of ~ 1.5 T attributable to inter-

chain interactions between the $Mn^{2+}$- F - $Mn^{2+}$ chain and the $Mn^{3+}$ - F - $Mn^{3+}$ chain along the $a$-direction and/or between two $Mn^{3+}$ - F - $Mn^{3+}$ chains along the $c$-direction. Spin flop transition will occur if the magnetic moments gradually rotate when the magnetic field increases. In order to understand the spin flop transition of $Ba_3Mn_3F_{14}$, the study of the magnetization curve versus the magnetic field using single crystal as a function of the crystallographic directions is required.

The dc magnetic susceptibility of $NaBa_7Mn_7F_{34}$ was measured under 1000 Oe in the temperature range 2-300 K and is shown as $\chi^{-1}$ and $\chi T$ versus T plots in Figure 5.18a and Figure 5.18b, respectively. From the inverse susceptibility versus temperature shown in Figure 5.18a, the susceptibility data were fit to the Curie-Weiss law, $\chi = C / (T - \theta)$ for T > 50 K, where C is the Curie constant and $\theta$ is the Weiss constant. The Curie constant is 24.82 emu K $mol^{-1}$ and the Weiss constant is -51.83 K, which are extracted from the curve fitting. On the basis of fit, the effective magnetic moment is 5.33 $\mu_B$/f.u, which is slightly higher than the theoretical spin only value of 5.21 $\mu_B$/f.u. ($Mn^{2+}$ = 5.9 $\mu_B$ and $Mn^{3+}$ = 4.9 $\mu_B$). This difference could be explained on the basis of the orbital contribution of the Mn(III) cations. A negative Weiss constant indicates anti-ferromagnetic interactions between Mn moments. The plot of $\chi T$ versus temperature shown in Figure 5.18b, exhibits a minimum of $\chi T$ around 10 K. This magnetic behavior is characteristic of ferrimagnetic chains.[55]

Magnetic properties and magnetic structures of Jarlite-related compounds, e.g. $Ba_7MFe_6F_{34}$ ($M^{2+}$ = $Mn^{2+}$, $Fe^{2+}$, $Cu^{2+}$) have been reported.[36-37,40] These compounds showed ferrimagnetic behavior ($T_C$ = 27, 30, 12 K, respectively) attributable to the

interplay between intra-chain interaction and inter-chain interaction in one dimensional magnetic ring chains in the crystal structure. Also, a theoretical model of one dimensional magnetic ring chain was proposed.[56]

Compared with previous magnetic studies of the Jarlite derivative compounds[36-37,40], magnetic behavior of $NaBa_7Mn_7F_{34}$ also showed ferrimagnetic behavior with very low magnetic transition temperature ($T_C$ = ~ 5 K). This result suggested that the presence of disordered manganese ($Mn^{2+}/Mn^{3+}$) as well as disordered fluorine (F10a or F10b) in one dimensional magnetic ring chains in the crystal structure give rise to lowering the magnetic transition temperature.

Isothermal magnetization of $NaBa_7Mn_7F_{34}$ was measured at 2 K (below $T_C$) as a function of the applied field H is shown in Figure 5.19. The magnetization vs. field H at 2 K showed the appearance of very weak spontaneous magnetization between - 2 and 2 T attributable to inter-chain interactions in one dimensional magnetic ring chains. More detailed magnetic studies and magnetic structure determination of $NaBa_7Mn_7F_{34}$ are required to understand the magnetic behavior.
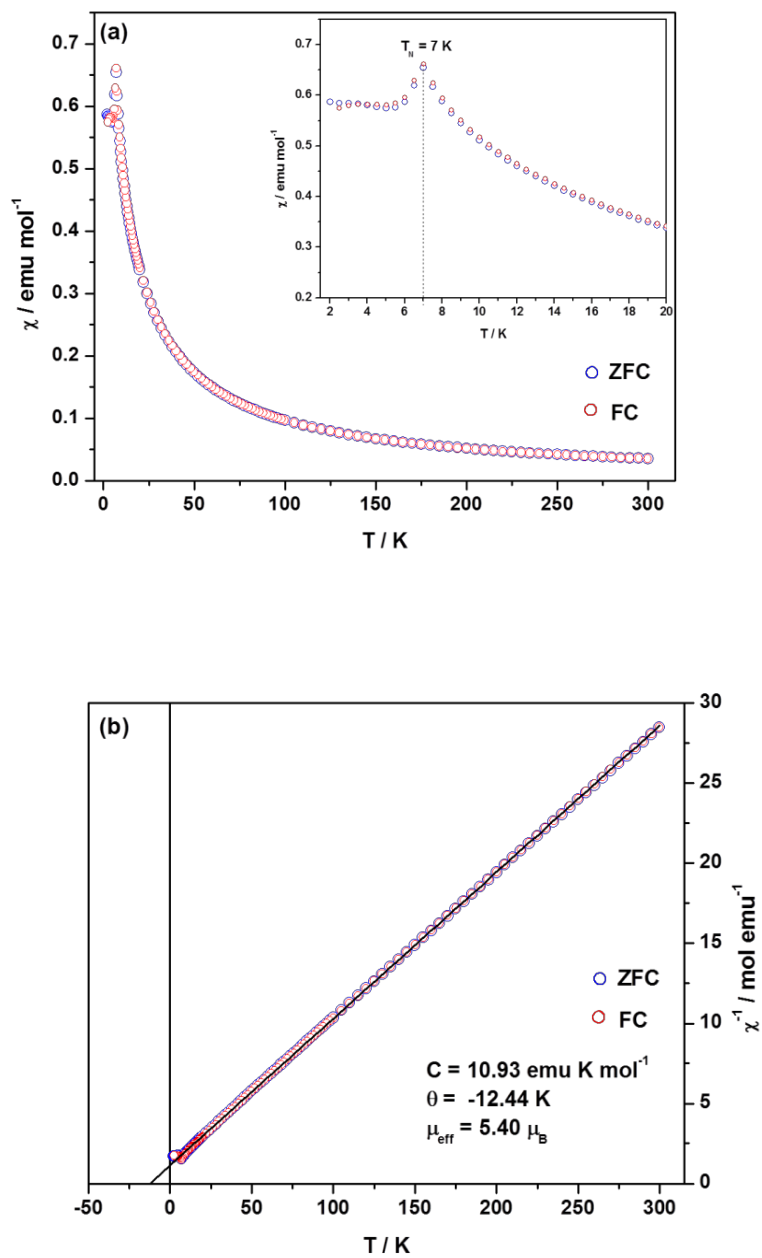
**Figure 5.16** Temperature dependence of (a) the magnetic susceptibility of $Ba_3Mn_3F_{14}$ measured in 500 Oe, and (b) the inverse magnetic susceptibility of $Ba_3Mn_3F_{14}$ with a Curie-Weiss fit (solid line). The inset to (a) shows a close up of the low-temperature region revealing the 7 K Néel temperature.
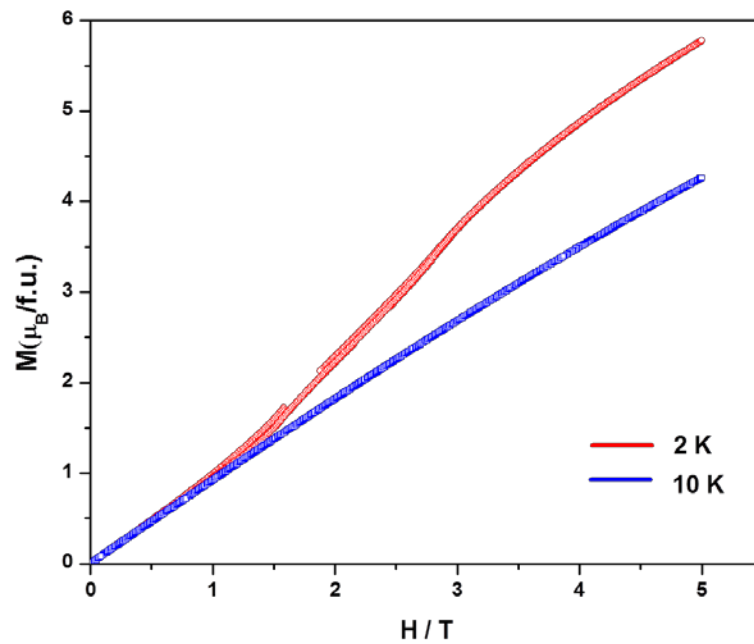
**Figure 5.17** Isothermal magnetization of $Ba_3Mn_3F_{14}$ measured at 2 K (below $T_N$) and 10 K (above $T_N$) as a function of applied field H.
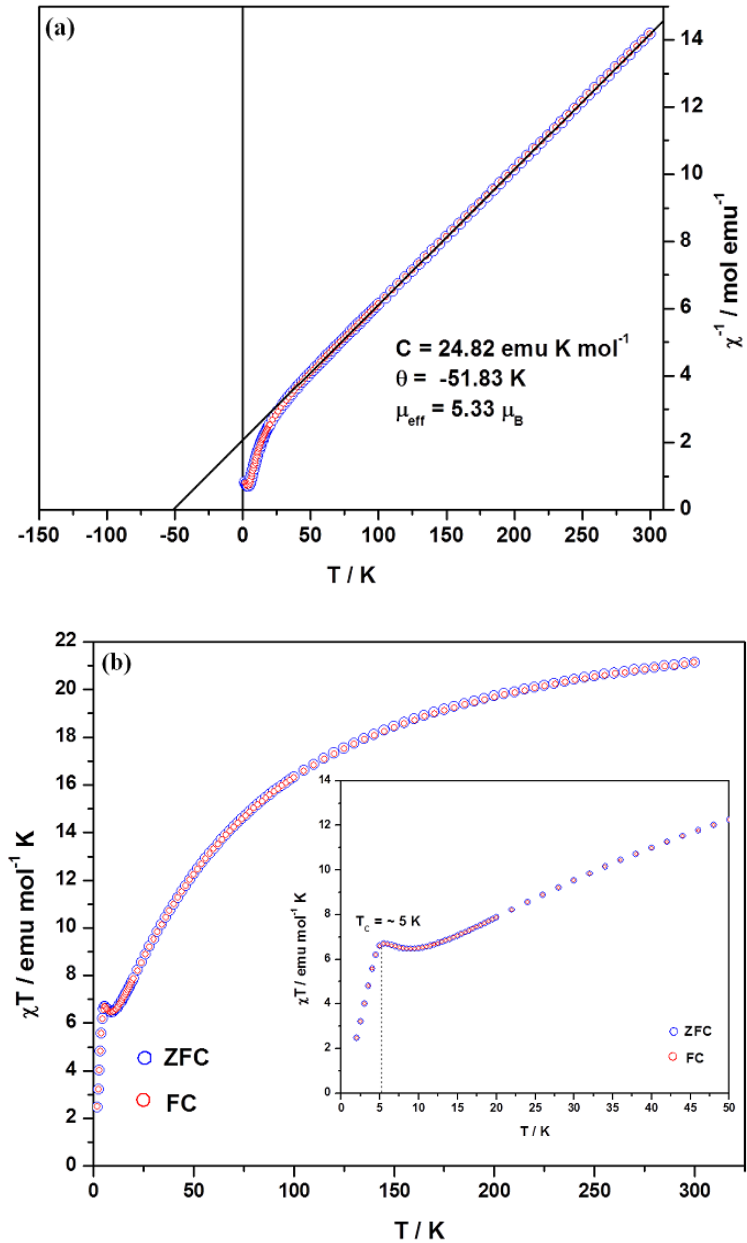
**Figure 5.18** Temperature dependence of (a) the inverse magnetic susceptibility of $NaBa_7Mn_7F_{34}$ measured in 1000 Oe with a Curie-Weiss fit (solid line), and (b) the plot of $\chi T$ for $NaBa_7Mn_7F_{34}$. The inset to (b) shows a close up of the low-temperature region revealing the minimum of $\chi T$ around 10 K.
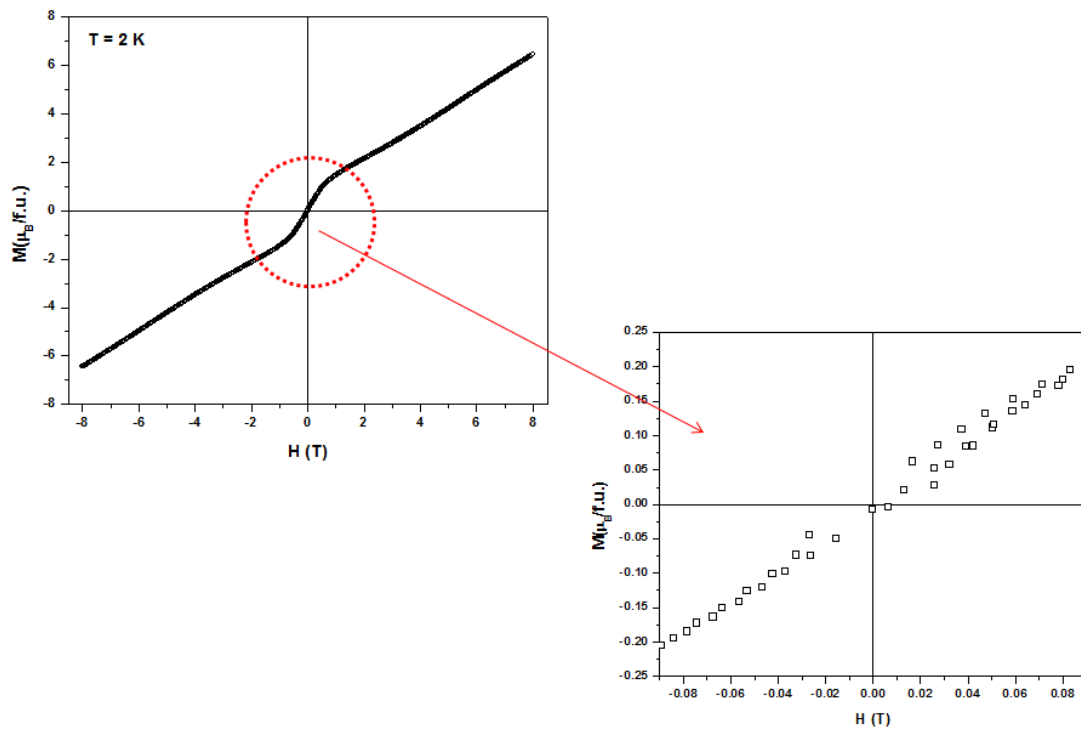
**Figure 5.19** Isothermal magnetization of NaBa$_7$Mn$_7$F$_{34}$ measured at 2 K (below T$_C$) as a function of applied field H.

## 5.5 Conclusion

We successfully synthesized the new mixed valence manganese ($Mn^{2+}/Mn^{3+}$) fluoride materials, $Ba_3Mn_3F_{14}$ and $NaBa_7Mn_7F_{34}$, via hydrothermal route using $CF_3COOH$ aqueous solution. $Ba_3Mn_3F_{14}$ showed anti-ferromagnetic behavior at 7 K and also demonstrated a field induced spin flop transition below a Néel temperature at the field of ~1.5 T attributable to inter-chain interactions. $NaBa_7Mn_7F_{34}$ showed ferrimagnetic behavior at ~ 5 K and also very weak spontaneous magnetization was observed between -2 and 2 T attributable to interplay between intra-chain interaction and inter-chain interaction in the crystal structure. More detailed magnetic measurements and magnetic structure determination are required to understand the magnetic behavior of $Ba_3Mn_3F_{14}$ and $NaBa_7Mn_7F_{34}$.

## 5.6 References

(1)     Hagenmuller, P. *INORGANIC SOLID FLUORIDES Chemistry and Physics*; Academic Press, INC.: Orlando, 1985.

(2)     Keve, E. T.; Abrahams, S. C.; Bernstein, J. L. *J. Chem. Phys.* **1969**, *51*, 4928.

(3)     Asahi, T.; Tomizawa, M.; Kobayashi, J.; Kleemann, W. *Phys. Rev. B* **1992**, *45*, 1971.

(4)     Poole, A.; Roessli, B.; Zaharko, O.; Kramer, K. W. *J. Phys.-Condes. Matter* **2011**, *23*, 266004.

(5)     Kohl, J.; Wiedemann, D.; Nakhal, S.; Bottke, P.; Ferro, N.; Bredow, T.; Kemnitz, E.; Wilkening, M.; Heitjans, P.; Lerch, M. *J. Mater. Chem.* **2012**, *22*, 15819.

(6)     Massa, W. *Z. Kristall.* **1983**, *162*, 166.

(7)     Massa, W.; Babel, D. *Chem. Rev.* **1988**, *88*, 275.

(8)     Massa, W. *Rev. Inorg. Chem.* **1999**, *19*, 117.

(9)     Sears, D. R.; Hoard, J. L. *J. Chem. Phys.* **1969**, *50*, 1066.

(10)    Pebler, J.; Massa, W.; Lass, H.; Ziegler, B. *J. Solid State Chem.* **1987**, *71*, 87.

(11)    Hahn, F.; Massa, W. *Z. Naturforsch.* **1990**, *B 45*, 1341.

(12)    Núñez, P.; Roisnel, T. *J. Solid State Chem.* **1996**, *124*, 338.

(13)    Carlson, S.; Xu, Y.; Norrestam, R. *Z. Kristallogr.* **1999**, *214*, 259.

(14)    Massa, W.; Steiner, M. *J. Solid State Chem.* **1980**, *32*, 137.

(15)    Wandner, K. H.; Hoppe, R. *Z. Anorg. Allg. Chem.* **1987**, *546*, 113.

(16)    Molinier, M.; Massa, W.; Khairoun, S.; Tressaud, A.; Soubeyroux, J. L. *Z. Naturforsch.* **1991**, *B 46*, 1669.

(17)    Molinier, M.; Massa, W. *Z. Naturforsch.* **1992**, *B 47*, 783.

(18)    Nuñez, P.; Tresaud, A.; Grannce, J.; Hagenmuller, P.; Massa, W.; Babel, D.; Boireau, A.; Soubeyroux, J. L. *Z. Anorg. Allg. Chem.* **1992**, *609*, 71.

(19)    Moron, M. C.; Palacio, F.; Rodriguez-Carvajal, J. *J. Phys.: Condens. Matter* **1993**, *5*, 4909.

(20)    Morón, M. C.; Palacio, F.; Clark, S. M.; Paduan-Filho, A. *Phys. Rev. B* **1995**, *51*, 8660.

(21)    Morón, M. C.; Palacio, F.; Clark, S. M. *Phys. Rev. B* **1996**, *54*, 7052.

(22)    Bukovec, P.; Hoppe, R. *Z. Anorg. Allg. Chem.* **1984**, *509*, 138.

(23)    Müller, U.; Hoppe, R. *Z. Anorg. Allg. Chem.* **1990**, *583*, 205.

(24)    Massa, W. *Habilitationsschrif* Marburg, 1982.

(25)    Frenzen, G.; Kummer, S.; Massa, W.; Babel, D. *Z. Anorg. Allg. Chem.* **1987**, *553*, 75.

(26)    Molinier, M.; Massa, W. *Z. Anorg. Allg. Chem.* **1994**, *620*, 833.

(27)    Kim, S. W.; Kim, S. H.; Halasyamani, P. S.; Green, M. A.; Bhatti, K. P.; Leighton, C.; Das, H.; Fennie, C. J. *Chem. Sci.* **2012**, *3*, 741.

(28)    Kim, S. W.; Chang, H. Y.; Halasyamani, P. S. *J. Am. Chem. Soc.* **2010**, *132*, 17684.

(29)    Samouél, M.; de Kozak, A.; Renaudin, J.; Ferey, G. *Z. Anorg. Allg. Chem.* **1990**, *590*, 200.

(30)    Welsch, M.; Holler, H.; Babel, D. *Z. Anorg. Allg. Chem.* **1989**, *575*, 171.

(31)    Dupont, N.; Gredin, P.; Pierrard, A.; de Kozak, A. *Solid State Sci.* **2000**, *2*, 531.

(32)     Brown, I. D.; Altermatt, D. *Acta Cryst.* **1985**, *B41*, 244.

(33)     Brese, N. E.; O'Keeffe, M. *Acta Cryst.* **1991**, *B47*, 192.

(34)     Brown, I. D. *The Chemical Bond in Inorganic Chemistry - The Bond Valence Model. IUCr monographs on Crystallography 12*; Oxford University Press, 2002.

(35)     Hawthorne, F. C. *Can. Mineral.* **1983**, *21*, 553.

(36)     Le, L. A.; Darriet, J.; Tressaud, A.; Hagenmuller, P. *C. R. Acad. Sci., Ser. 2* **1989**, *308*, 713.

(37)     Renaudin, J.; Ferey, G.; Drillon, M.; De, K. A.; Samouel, M. *C. R. Acad. Sci., Ser. 2* **1989**, *308*, 1217.

(38)     Crosnier-Lopez, M. P.; Calage, Y.; Duroy, H.; Fourquet, J. L. *Z. Anorg. Allg. Chem.* **1995**, *621*, 1025.

(39)     Pierrard, A.; de, K. A.; Gredin, P.; Renaudin, J. *Z. Anorg. Allg. Chem.* **1996**, *622*, 1200.

(40)     Darriet, J.; Le Lirzin, A.; Georges, R. In *Advanced Inorganic Fluorides*; Nakajima, T., Žemva, B., Tressaud, A., Eds.; Elsevier: Switzerland, 2000, p 283.

(41)     Sawodny, W.; Rau, K. M.; Bolkart, W. *J. Fluorine Chem.* **1989**, *43*, 119.

(42)     Sawodny, W.; Rau, K. M. *J. Fluorine Chem.* **1993**, *61*, 111.

(43)     Nakamoto, K. *Infrared and Raman Spectra of Inorganic and Coordination Compounds Part A: Theory and Applications in Inorganic Chemistry*; 5th ed.; John Wiley & Sons, Inc: New York, 1997.

(44)     Kubelka, P. M.; Munk, F. *Z. Tech. Phys.* **1931**, *12*, 593.

(45)     Tauc, J.; Grigorovici, R.; Vancu, A. *physica status solidi (b)* **1966**, *15*, 627.

(46)     Lever, A. B. P. *Inorganic Electronic Spectroscopy, 2nd ed.*; Elsevier Science Publishers B. V.: Amsterdam, 1984.

(47)     Aranda, M. A. G.; Bruque, S.; Attfield, J. P. *Inorg. Chem.* **1991**, *30*, 2043.

(48)     Nikotin, O.; Lindgård, P. A.; Dietrich, O. W. *J. Phys. C: Solid State Phys.* **1969**, *2*, 1168.

(49)     Tressaud, A.; Parenteau, J. M.; Dance, J. M.; Portier, J.; Hagenmuller, P. *Mater. Res. Bull.* **1973**, *8*, 565.

(50)     Wintenberger, M.; Dance, J. M.; Tressaud, A. *Solid State Commun.* **1975**, *17*, 185.

(51)     Lacorre, P.; Pannetier, J.; Pebler, J.; Nagel, S.; Babel, D.; de Kozak, A.; Samouël, M.; Férey, G. *J. Solid State Chem.* **1992**, *101*, 296.

(52)     Goodenough, J. B. *Phys. Rev.* **1955**, *100*, 564.

(53)     Kanamori, J. *J. Phys. Chem. Solid* **1959**, *10*, 87.

(54)     Goodenough, J. B. *Magnetism and the Chemical Bond*; Interscience: New York, 1963.

(55)     Khan, O. *Molecular Magnetism*; WILEY-VCH, 1993.

(56)     Qiang, X. U.; Darriet, J.; Georges, R. *J. Magn. Magn. Mater.* **1988**, *73*, 379.

**Table 5.1** Crystallographic Data for $Ba_3Mn_3F_{14}$ and $NaBa_7Mn_7F_{34}$.

| Parameter | $Ba_3Mn_3F_{14}$ | $NaBa_7Mn_7F_{34}$ |
|---|---|---|
| F.W. | 842.84 | 2014.95 |
| $T$ (K) | 296(2) | 296(2) |
| Crystal System | Orthorhombic | Monoclinic |
| Space Group | $Pnma$ (No.62) | $C2/m$ (No.12) |
| $a$ (Å) | 27.272(2) | 16.961(9) |
| $b$ (Å) | 5.6613(4) | 11.551(6) |
| $c$ (Å) | 7.4711(6) | 7.651(4) |
| Angle(deg) | $\alpha = \beta = \gamma = 90$ | $\beta = 101.785(12)$ |
| $V$ (Å$^3$) | 1153.51(15) | 1467.4(13) |
| Z | 4 | 2 |
| $\rho_{calcd}$ (g/cm$^3$) | 4.853 | 4.560 |
| $\mu$(mm$^{-1}$) | 13.43 | 12.34 |
| $2\theta_{max}$ (deg) | 58.30 | 57.89 |
| $R$ (int) | 0.0474 | 0.0332 |
| GOF | 1.165 | 1.129 |
| $R$ $(F)^a$ | 0.0256 | 0.0224 |
| $R_w$ $(F_o^2)^b$ | 0.0644 | 0.0587 |

$^aR$ $(F) = \Sigma||F_o| - |F_c||/\Sigma|F_o|$ , $^bR_w$ $(F_o^2) = [\Sigma w(F_o^2 - F_c^2)^2/\Sigma w(F_o^2)^2]^{1/2}$

**Table 5.2** Atomic Coordinates for $Ba_3Mn_3F_{14}$.

| Atom | x | y | z | $U_{eq}(\mathring{A}^2)^a$ |
|---|---|---|---|---|
| **Ba(1)** | 0.1045(6) | 0.2500 | 0.8200(9) | 0.0161(7) |
| **Ba(2)** | 0.0537(3) | -0.2500 | 0.3786(5) | 0.0140(7) |
| **Ba(3)** | 0.2714(2) | 0.2500 | 0.0486(4) | 0.0173(1) |
| **Mn(1) ($Mn^{2+}$)** | 0.0120(1) | -0.2500 | 0.8787(1) | 0.0144(8) |
| **Mn(2) ($Mn^{3+}$)** | 0.1718(9) | -0.2500 | 0.0197(6) | 0.0159(7) |
| **Mn(3) ($Mn^{3+}$)** | 0.1432(8) | 0.2500 | 0.3490(3) | 0.0186(6) |
| **F(1)** | 0.0300(1) | -0.0063(9) | 0.6765(1) | 0.0159(9) |
| **F(2)** | 0.1185(1) | -0.2500 | 0.8714(2) | 0.0197(1) |
| **F(3)** | -0.0445(5) | -0.0015(1) | 0.9434(7) | 0.0166(2) |
| **F(4)** | 0.1993(9) | -0.0017(3) | 0.8758(2) | 0.0317(8) |
| **F(5)** | 0.0765(4) | 0.2500 | 0.3663(9) | 0.0200(9) |
| **F(6)** | 0.1437(9) | 0.0023(7) | 0.5275(8) | 0.0267(3) |
| **F(7)** | 0.2246(1) | -0.2060(8) | 0.1700(1) | 0.0177(7) |
| **F(8)** | 0.2098(9) | 0.2034(6) | 0.3373(8) | 0.0271(5) |
| **F(9a)[b]** | 0.1430(1) | 0.0900(9) | 0.1400(7) | 0.0239(1) |
| **F(9b)[b]** | 0.1376(9) | -0.0904(1) | 0.1898(5) | 0.0219(2) |

[a] $U_{eq}$ is defined as one-third of the trace of the orthogonal $U_{ij}$ tensor.

[b] The site occupancy factor for these atoms is 0.5.

**Table 5.3** Atomic Coordinates for $NaBa_7Mn_7F_{34}$.

| Atom | sof | x | y | z | $U_{eq}(Å^2)^a$ |
|---|---|---|---|---|---|
| **Na(1)** | | 0.5 | 0 | 0 | 0.0241(8) |
| **Ba(1)** | | 0 | 0 | 0 | 0.0161(1) |
| **Ba(2)** | | 0.2615(5) | 0 | 0.1407(1) | 0.0166(2) |
| **Ba(3)** | | 0.3551(1) | 0.1963(4) | -0.3074(8) | 0.0176(3) |
| **Mn(1) ($Mn^{2+}$)** | | 0.5 | 0 | 0.5 | 0.0091(2) |
| **Mn(2) ($Mn^{2+}/Mn^{3+}$)** | | 0.1615(6) | 0 | 0.5514(8) | 0.0121(8) |
| **Mn(3) ($Mn^{3+}$)** | | 0.3942(3) | 0.2540(6) | 0.1957(8) | 0.0146(1) |
| **F(1)** | | 0.4402(2) | 0 | -0.2818(4) | 0.0190(7) |
| **F(2)** | | 0.2296(1) | 0.1175(2) | 0.4452(3) | 0.0240(5) |
| **F(3)** | | 0.3848(9) | 0.1268(2) | 0.0347(3) | 0.0239(5) |
| **F(4)** | | 0.3678(7) | 0.3649(2) | -0.0250(4) | 0.0243(5) |
| **F(5)** | | 0.2864(9) | 0.2427(2) | 0.1956(4) | 0.0255(6) |
| **F(6)** | | 0.5008(4) | 0.2694(3) | 0.1927(4) | 0.0302(6) |
| **F(7)** | | 0.4105(2) | 0.1265(3) | 0.3966(4) | 0.0377(8) |
| **F(8)** | | 0.2507(3) | 0 | 0.7676(5) | 0.0337(1) |
| **F(9a)** | 0.3 | 0.0930(8) | 0.0171(9) | 0.3254(1) | 0.0256(2)[b] |
| **F(9b)** | 0.2 | 0.0651(2) | 0.0227(2) | 0.341(2) | 0.0256(2)[b] |
| **F(10a)** | 0.6 | 0.4059(3) | 0.3602(6) | 0.3892(1) | 0.0344(1)[b] |
| **F(10b)** | 0.4 | 0.4086(5) | 0.3904(1) | 0.3347(2) | 0.0344(1)[b] |

[a] $U_{eq}$ is defined as one-third of the trace of the orthogonal $U_{ij}$ tensor.

[b] $U_{iso}$ isotropic thermal parameter

**Table 5.4** Selected Bond Distances and Angles for $Ba_3Mn_3F_{14}$.

| Bond | Distance (Å) | Bond | Distance (Å) |
|---|---|---|---|
| Ba(1) — F(1) | 2.719(3) × 2 | Mn(1) — F(1) | 2.103(3) × 2 |
| Ba(1) — F(2) | 2.881(7) × 2 | Mn(1) — F(3) | 2.140(3) × 2 |
| Ba(1) — F(3) | 2.789(3) × 2 | Mn(1) — F(3) | 2.143(3) × 2 |
| Ba(1) — F(4) | 2.982(3) × 2 | Mn(2) — F(2) | 1.830(4) |
| Ba(1) — F(6) | 2.808(3) × 2 | Mn(2) — F(4) | 1.922(3) × 2 |
| Ba(1) — F(9a) | 2.763(6) × 2 | Mn(2) — F(7) | 1.841(5) |
| Ba(2) — F(1) | 2.697(3) × 2 | Mn(2) — F(9a) | 2.266(6) |
| Ba(2) — F(1) | 2.737(3) × 2 | Mn(2) — F(9b) | 1.817(6) |
| Ba(2) — F(3) | 2.807(3) × 2 | Mn(3) — F(5) | 1.825(4) |
| Ba(2) — F(5) | 2.899(6) × 2 | Mn(3) — F(6) | 1.935(3) × 2 |
| Ba(2) — F(6) | 3.052(3) × 2 | Mn(3) — F(8) | 1.838(6) |
| Ba(2) — F(9b) | 2.837(6) × 2 | Mn(3) — F(9a) | 1.805(5) |
| Ba(3) — F(4) | 2.749(3) × 2 | Mn(3) — F(9b) | 2.270(6) |
| Ba(3) — F(4) | 2.930(4) × 2 | | |
| Ba(3) — F(6) | 2.723(3) × 2 | Mn(1) — Mn(1) | 3.424(8) |
| Ba(3) — F(7) | 2.842(5) | Mn(1) — Mn(2) | 4.486(1) |
| Ba(3) — F(7) | 3.020(7) × 2 | Mn(1) — Mn(3) | 4.564(1) |
| Ba(3) — F(8) | 2.745(6) | Mn(2) — Mn(3) | 3.830(5) |

| | Angle(°) |
|---|---|
| Mn(1) — F(3) — Mn(1) | 106.17(13) |
| Mn(2) — F(9a) — Mn(3) | 140.20(2) |
| Mn(2) — F(9b) — Mn(3) | 139.00(2) |

**Table 5.5** Selected Bond Distances and Angles for $NaBa_7Mn_7F_{34}$.

| Bond | Distance (Å) | Bond | Distance (Å) |
|---|---|---|---|
| **Na(1) — F(1)** | 2.188(4) × 2 | **Mn(1) — F(1)** | 2.123(3) × 2 |
| **Na(1) — F(3)** | 2.498(3) × 4 | **Mn(1) — F(7)** | 2.139(3) × 4 |
| **Ba(1) — F(4)** | 2.705(3)× 4 | **Mn(2) — F(2)** | 2.054(3) × 2 |
| **Ba(1) — F(6)** | 3.043(1) × 4 | **Mn(2) — F(8)** | 1.999(5) |
| **Ba(1) — F(9a)** | 2.668(8) | **Mn(2) — F(9a)** | 1.887(8) |
| **Ba(1) — F(9b)** | 2.629(2) | **Mn(2) — F(9b)** | 2.065(2) |
| **Ba(2) — F(2)** | 2.842(3)× 2 | **Mn(2) — F(10a)** | 2.081(6) |
| **Ba(2) — F(3)** | 2.806(3) × 2 | **Mn(2) — F(10b)** | 2.049(9) |
| **Ba(2) — F(4)** | 2.691(3) × 2 | **Mn(3) — F(3)** | 1.903(3) |
| **Ba(2) — F(5)** | 2.853(3) × 2 | **Mn(3) — F(4)** | 2.094(3) |
| **Ba(2) — F(7)** | 3.214(4) × 2 | **Mn(3) — F(5)** | 1.832(3) |
| **Ba(2) — F(8)** | 2.823(4) | **Mn(3) — F(6)** | 1.822(3) |
| **Ba(3) — F(1)** | 2.710(2) | **Mn(3) — F(7)** | 2.106(3) |
| **Ba(3) — F(2)** | 2.650(3) | **Mn(3) — F(10a)** | 1.901(6) |
| **Ba(3) — F(2)** | 2.658(3) | **Mn(3) — F(10b)** | 1.888(9) |
| **Ba(3) — F(3)** | 2.686(3) | | |
| **Ba(3) — F(4)** | 2.880(3) | **Mn(1) — Mn(3)** | 3.9424(2) |
| **Ba(3) — F(5)** | 2.737(3) | **Mn(2) — Mn(3)** | 3.6677(2) |
| **Ba(3) — F(6)** | 2.625(3) | **Mn(2) — Mn(2)** | 5.3748(3) |
| **Ba(3) — F(7)** | 2.779(3) | **Mn(3) — Mn(3)** | 5.2652(3) |
| **Ba(3) — F(8)** | 2.962(3) | | |
| | | **Angle(°)** | |
| **Mn(1) — F(7) — Mn(3)** | | 136.48(2) | |
| **Mn(2) — F(10a) — Mn(3)** | | 134.1(3) | |
| **Mn(2) — F(10b) — Mn(3)** | | 137.3(5) | |

**Table 5.6** Bond valence analysis of the $Ba_3Mn_3F_{14}$[a].

| Atom | F(1) | F(2) | F(3) | F(4) | F(5) | F(6) | F(7) | F(8) | F(9a)[b] | F(9b)[b] | $\Sigma_{cations}$ |
|---|---|---|---|---|---|---|---|---|---|---|---|
| Ba(1) | 0.238[×2] | [×2]0.153[×2] | 0.197[×2] | 0.117[×2] | | 0.187[×2] | | | 0.086[×2] | | 1.956 |
| Ba(2) | 0.252[×2]<br>0.227[×2] | | 0.188[×2] | | [×2]0.146[×2] 0.097[×2] | | | | | 0.086[×2] | 1.992 |
| Ba(3) | | | | 0.219[×2]<br>0.134[×2] | | 0.235[×2] | 0.171<br>[×2]0.105[×2] [×2]0.096[×2] | 0.222 | | | 1.971 |
| Mn(1) | 0.334[×2] | 0.303[×2]<br>0.300[×2] | | | | | | | | | 1.874 |
| Mn(2) | | 0.631 | | 0.492[×2] | | | 0.612 | | [×0.5]0.194 | [×0.5]0.653 | 3.074 |
| Mn(3) | | | | | 0.640 | 0.475[×2] | | 0.617 | [×0.5]0.675 | [×0.5]0.192 | 3.074 |
| $\Sigma_{anions}$ | 1.051 | 0.937 | 0.988 | 0.962 | 0.932 | 0.994 | 0.993 | 1.031 | 0.521 | 0.509 | |

124

**Table 5.7** Bond valence analysis of the NaBa$_7$Mn$_7$F$_{34}$[a].

| Atom | F(1) | F(2) | F(3) | F(4) | F(5) | F(6) | F(7) | F(8) | F(9a)[b] | F(9b)[b] | F(10a)[b] | F(10b)[b] | Σcations |
|---|---|---|---|---|---|---|---|---|---|---|---|---|---|
| Na(1) | 0.251[×2] | 0.109[×4] | | | | | | | | | | | 0.938 |
| Ba(1) | | | | 0.247[×4] | | 0.099[×4] | | | 0.365 | 0.201 | | | 1.951 |
| Ba(2) | | 0.171[×2] | 0.188[×2] | 0.257[×2] | 0.166[×2] | | 0.062[×2] | 0.180 | | | | | 1.868 |
| Ba(3) | | 0.281 0.287 | 0.260 | 0.154 | 0.227 | 0.202 | 0.307 | [×2]0.123 | | | | | 2.085 |
| Mn(1) | 0.317[×2] | | | | | 0.304[×4] | | | | | | | 1.850 |
| Mn(2) | | 0.382[×2] | | | | | | 0.443 | 0.400 | 0.123 | 0.431 | 0.304 | 2.465 |
| Mn(3) | | | 0.518 | 0.309 | 0.628 | 0.646 | 0.299 | | | | 0.317 | 0.211 | 2.928 |
| Σanions | 1.056 | 1.121 | 1.075 | 0.967 | 1.021 | 0.947 | 0.972 | 0.869 | 0.765 | 0.324 | 0.748 | 0.515 | |

[a] Bond valence sums calculated with the formula: $S_i = \exp[(R_0\text{-}R_i)/B]$, where $S_i$ = valence of bond "$i$", $R_0$ is a constant dependent on the bonded elements, $R_i$ is the bond length of bond $i$ and B=0.37. Left and right superscripts indicate the # of equivalent bonds for anions and cations, respectively.

[b] The site occupancy factor of F(9a), F(9b), F(10a), and F(10b) is 0.3, 0.2, 0.6, 0.4, respectively.

# CHAPTER 6. CrF$_3$·0.5H$_2$O: Synthesis, Structure, and Characterization of a New Cubic Pyrochlore-related Mixed-metal Fluoride

## 6.1 Abstract

A new cubic pyrochlore-related mixed metal fluoride material, CrF$_3$·0.5H$_2$O has been synthesized and characterized. This material was synthesized through mild hydrothermal conditions using aqueous CF$_3$COOH solution. The material exhibits a three-dimensional pyrochlore-related structure consisting of corner-shared Cr$^{3+}$F$_6$ and isolated water molecules. In addition to single-crystal diffraction data, magnetometry measurements were carried out. Infrared, UV-vis, thermogravimetric measurements were also performed. Crystal data: CrF$_3$·0.5H$_2$O, Cubic, space group *Fd-3m* (No. 227), $a = b = c = 10.2584(6)$ Å, $V = 1079.54(19)$ Å$^3$, $Z = 16$, $T = 296(2)$ K.

## 6.2 Introduction

Pyrochlore-related materials have been studied extensively due to their interesting physical properties, e.g. magnetic frustration,[1-2] magnetoresistance,[3] superconductivity,[4] ferroelectrics[5] and so on. Pyrochlore-related materials have a general formula $A_2B_2X_7$ or $AB_2X_6$, where A, B are metals, X is an anion. Their physical properties are derived from the various atoms occupying different crystallographic sites in the pyrochlore lattice.

With respect to complex fluoride materials, $AM^{2+}M^{3+}F_6$ (A = $K^+$, $Rb^+$, $Cs^+$, $NH_4^+$; $M^{2+}$ = $Mg^{2+}$, $Mn^{2+}$, $Fe^{2+}$, $Co^{2+}$, $Ni^{2+}$, $Cu^{2+}$ ; $M^{3+}$ = $Al^{3+}$, $Ga^{3+}$, $V^{3+}$, $Cr^{3+}$, $Fe^{3+}$) type pyrochlore materials were synthesized and characterized.[6-7] Both crystallographic disorder and order are observed between the $M^{2+}$ and $M^{3+}$ cations on the octahedral sites. The crystallographic disorder of $M^{2+}$ and $M^{3+}$ cations gives rise to spin-glass behavior in cubic pyrochlore $CsNiCrF_6$.[8-9] Ordering of the $M^{2+}$ and $M^{3+}$ cations leads to the lowering of crystallographic symmetry (cubic to orthorhombic), e.g., modified pyrochlore $AFe_2F_6$ (A = $Rb^+$, $Cs^+$, $NH_4^+$).[2,10-12]

Furthermore, simple cubic pyrochlore fluoride materials, $M^{3+}F_3 \cdot 0.5H_2O$ or $M^{3+}_2F_6(H_2O)$ ($M^{3+}$ = $Al^{3+}$, $Fe^{3+}$, $V^{3+}$) were also synthesized and characterized.[13-16] $AlF_3 \cdot 0.5H_2O$ was obtained from the thermal decomposition of $AlF_3 \cdot 3H_2O$. $V_2F_6(H_2O)$ was prepared by the hydrothermal reaction using vanadium metal and HF aqueous solution. Recently, $FeF_3 \cdot 0.5H_2O$ was synthesized by the precipitation of $Fe(NO)_3 \cdot 9H_2O$ in hydrophobic $BF_4^-$ - based ionic liquids, $BmimBF_4$ and $C_{10}mimBF_4$.

We recently reported the synthesis and characterization of a new charge-ordered $Fe^{2+}/Fe^{3+}$ fluoride material, $RbFe_2F_6$. This material was synthesized through a mild

hydrothermal method using $CF_3COOH$.[2] In this chapter, utilizing a similar synthetic technique, we report the synthesis of cubic pyrochlore $CrF_3 \cdot 0.5H_2O$. In addition to the crystal structure, characterization and magnetic measurements were reported.

## 6.3 Experimental Section

**6.3.1 Reagents.** $CrF_3 \cdot 4H_2O$ (Aldrich, 97 %) and $CF_3COOH$ (Alfa Aesar, 99%) were used without any further purification.

**6.3.2 Synthesis.** $CrF_3 \cdot 0.5H_2O$ was obtained by hydrothermal method using a diluted $CF_3COOH$ solution. Crystals of $CrF_3 \cdot 0.5H_2O$ were grown by mixing 0.3621 g ($2.00 \times 10^{-3}$ mol) of $CrF_3 \cdot 4H_2O$ and 3 ml ($3.90 \times 10^{-2}$ mol) of $CF_3COOH$ with 5 ml of $H_2O$. The resultant solution was placed in a 23-mL Teflon-lined stainless autoclave that was subsequently sealed. The autoclave was gradually heated to 230 ℃, held for 24 h, and cooled slowly to room temperature at a rate 6 ℃ $h^{-1}$. The mother liquor was decanted from the only solid product, dark green colored octahedral crystals of $CrF_3 \cdot 0.5H_2O$, was recovered by filtration and washed with distilled water and acetone. The yield was ~70 % on the basis of $CrF_3 \cdot 4H_2O$. The powder X-ray diffraction pattern on the synthesized phase is in good agreement with the generated pattern from the single-crystal data.

## 6.4 Results and Discussion

**Synthesis.** Previously similar pyrochlore-related fluoride materials, e.g., Pyr-$FeF_3$ and $V_2F_6(H_2O)$ were synthesized and characterized.[15,17] Pyr-$FeF_3$ was prepared by the topotatic oxidation of modified pyrochlore material, $NH_4Fe_2F_6$. However, its preparation

was quite complicated and needed more steps. $V_2F_6(H_2O)$ was prepared by hydrothermal method using vanadium metal and aqueous HF solution at $200^oC$ for 5 days. Its preparation was quite simple, but took a long time. We were able to synthesize $CrF_3\cdot0.5H_2O$ through mild hydrothermal method using $CrF_3\cdot4H_2O$ and diluted $CF_3COOH$ aqueous solution at 230 $^oC$ for 24 h. Its preparation is quite simple, time-efficient, and highly reproducible. We have previously demonstrated that this method can be used to synthesize other complex fluoride materials.[2,18]

**Structure.** The room temperature structure of $CrF_3\cdot0.5H_2O$ was determined to be in the *Fd-3m* space group (No. 227), with lattice parameters of $a = b = c = 10.2584(6)$ Å. This represents a conventional β-pyrochlore lattice. β-pyrochlore could be written as $AB_2X_6$, which A is generally a large low valent cation (8b site), B is a relatively high valent cation which could have octahedral environment (16c site), and X is an anion (48f site). From $CrF_3\cdot0.5H_2O$, A cations are substituted by water molecules ($H_2O$), B cation is the chromium ion ($Cr^{3+}$), and X anion is the fluorine ion ($F^-$).

$CrF_3\cdot0.5H_2O$ exhibits a three dimensional structure consisting of corner shared $Cr^{3+}F_6$ octahedra and isolated water molecules (Figure 6.2). In connectivity term, the structure may be written as $(Cr^{3+}F_{6/2})^0(0.5H_2O)$. Infinite chains of corner shared $Cr^{3+}F_6$ octahedra are connected in two perpendicular ways. Its three dimensional $Cr_2F_6$ frameworks generates hexagonal open cages and isolated water molecules are located in these open cages. It is important to note that it could have some hydrogen bonds between water molecules and fluorine ions in the $Cr_2F_6$ framework. These possible hydrogen bonds

could affect the thermal behavior of samples. Also interestingly, corner shared tetrahedral units of four $Cr^{3+}$ in the structure could generate geometrical magnetic frustration.[1] The bond distance of $Cr^{3+}$ - F is 1.9347(8) Å, the distance of $Cr^{3+}$ - $Cr^{3+}$ is 3.6269(2) Å and the bond angles of $Cr^{3+}$ - F - $Cr^{3+}$ is 139.21(13)°. Bond valence calculation[19-21] (Table 6.4) resulted in values of 2.83 and 0.944 for $Cr^{3+}$ and $F^-$, respectively.
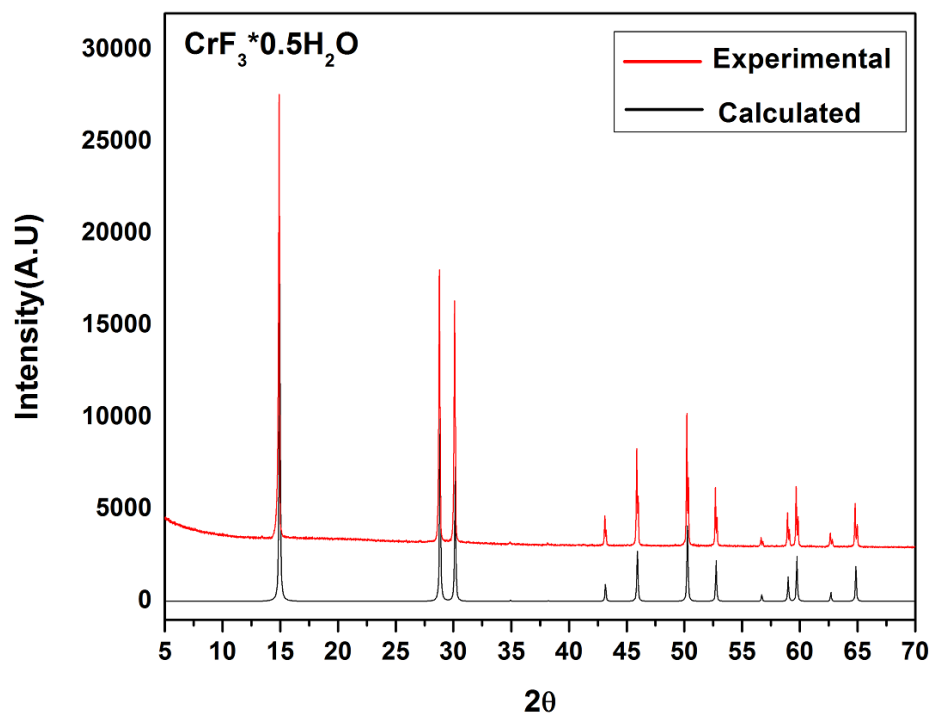


**Figure 6.1** Experimental and calculated powder X-ray diffraction patterns for $CrF_3 \cdot 0.5H_2O$.
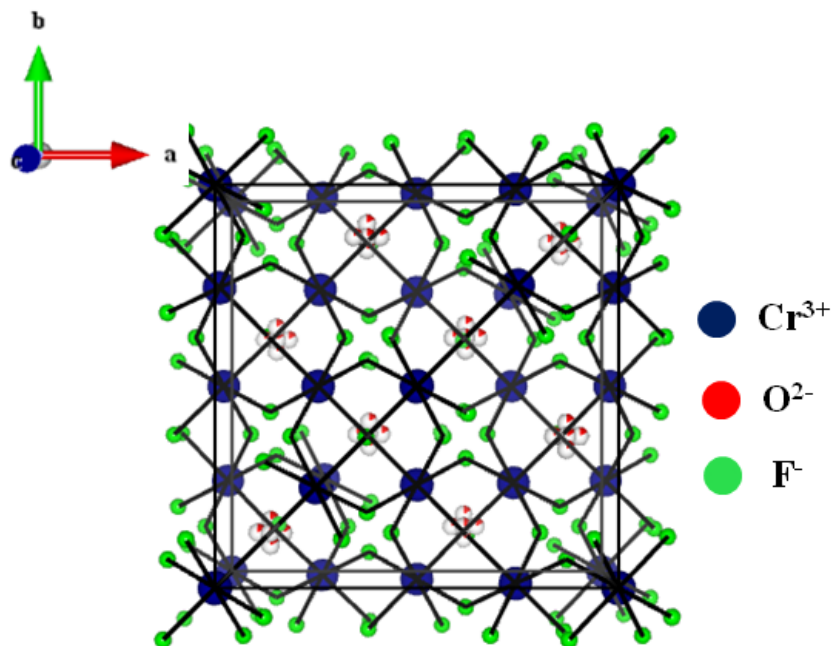
**Figure 6.2** Ball-and-stick representation of $CrF_3 \cdot 0.5H_2O$ in the *ab*-plane.



**Cr(1)**
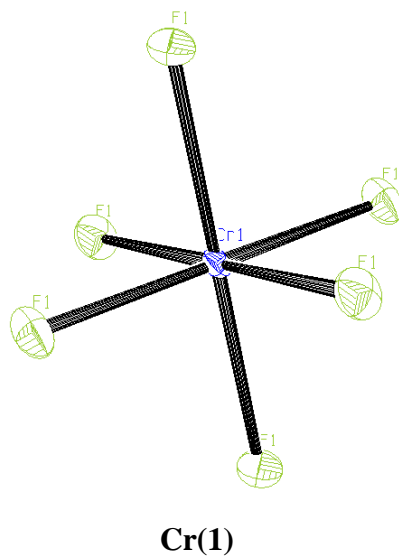
**Figure 6.3** ORTEP (50% probability ellipsoids) diagrams for $CrF_3 \cdot 0.5H_2O$.

**Thermal Analysis.** The thermal behavior of $CrF_3 \cdot 0.5H_2O$ was investigated using thermogravimetric analysis (TGA) under nitrogen atmosphere (Figure 6.4). There are two weight loss steps observed. The first weight loss (exp. 9.7%) occurred between 25 $^{o}C$ and 250 $^{o}C$ could assign the release of water molecules from open channels (calc. 7.6 %) or HF (calc. 8.5 %). From the powder XRD pattern of the sample annealed at 250 $^{o}C$ under nitrogen atmosphere, there was no phase transformation, annealed product retained its pyrochlore structure (Figure 6.5a). Thus, it is more likely to be releasing water molecules rather than HF. However, it is possible to retain some water molecules because of hydrogen bonding between water molecules and fluorine ions. We will discuss this possibility in the infrared spectroscopy section. A second weight loss occurred around 350 $^{o}C$, indicating the decomposition of samples. The powder XRD pattern of the sample annealed at 450 $^{o}C$ under nitrogen atmosphere showed amorphous phase, which indicated sample decomposition (Figure 6.5b). Finally, the powder XRD pattern of the final residue product after TGA experiment showed $Cr_2O_3$, which could explain the hydrolysis of sample by remaining water molecules (Figure 6.5c).
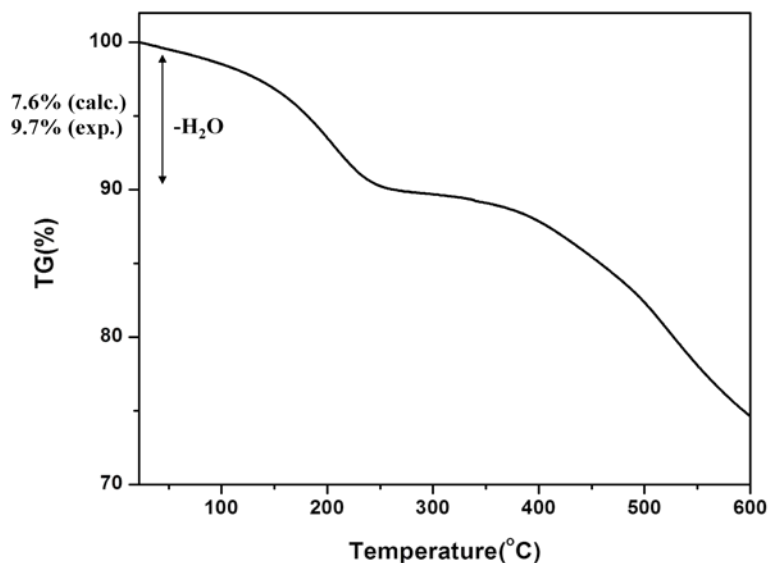
**Figure 6.4** Thermogravimetric analysis for $CrF_3 \cdot 0.5H_2O$.

**Infrared Spectroscopy.** The FT-IR spectra of $CrF_3 \cdot 0.5H_2O$ at room temperature and after annealing at 250 $^{o}$C for 48 h under nitrogen atmosphere showed three major bands around 3300 $cm^{-1}$, 1600 $cm^{-1}$ and 1150 $cm^{-1}$, which are attributable to O-H vibrations in water molecules and around 700 $cm^{-1}$, which is attributable to Cr - F vibration (Figure 6.6). These assignments are consistent with previous reports.[22] Even though the bands of O-H vibration decreased after annealing, significant amounts of water molecules still remained. This result suggested that the presence of hydrogen bonding between $H_2O$ and $F^-$ in $Cr_2F_6$ framework retarded perfect dehydration of samples at relatively high temperatures (250 $^{o}$C).
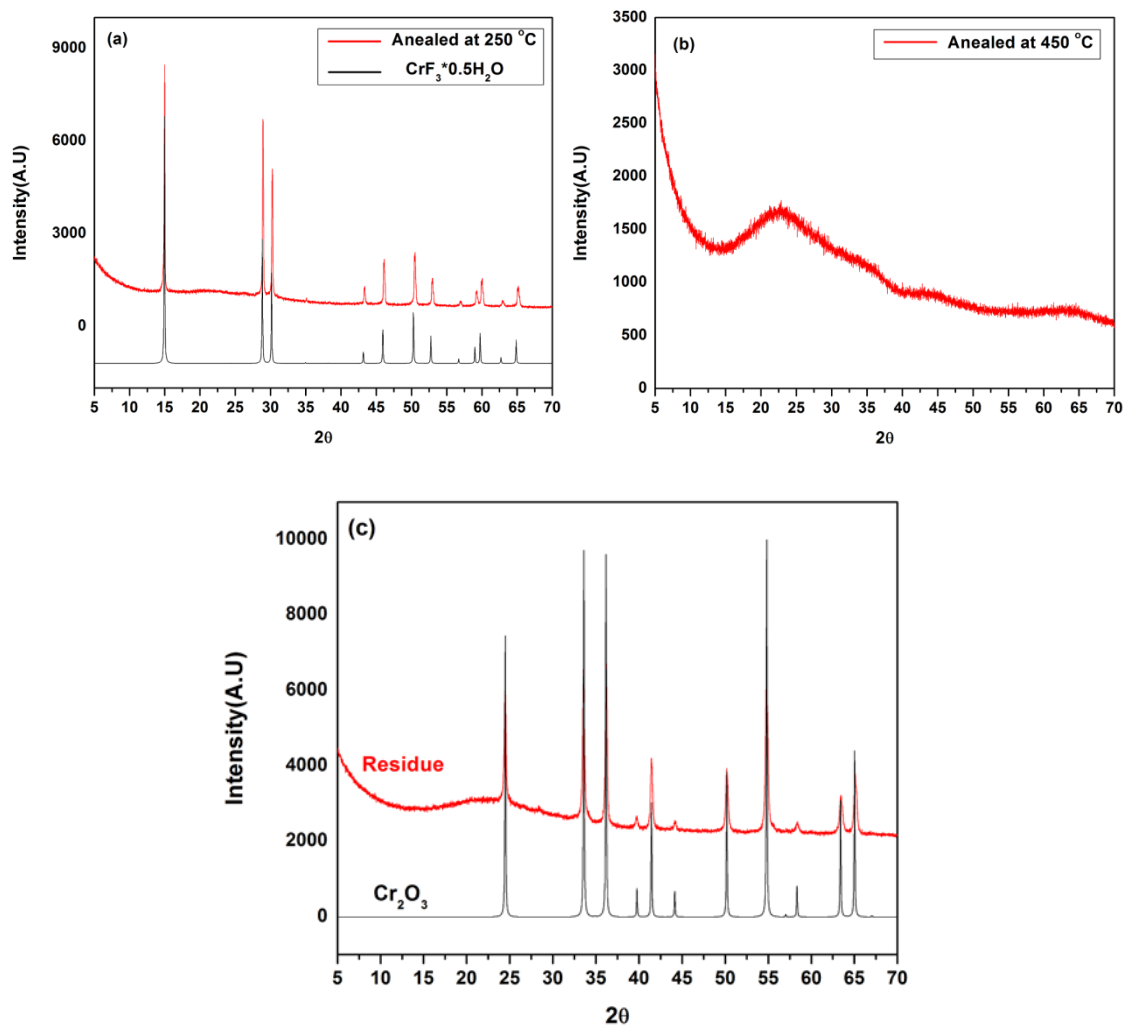
**Figure 6.5** Powder X-ray diffraction data for (a) annealed at 250 $^o$C under nitrogen atmosphere, (b) annealed at 450 $^o$C under nitrogen atmosphere and (c) final residuals after TGA Experiment.
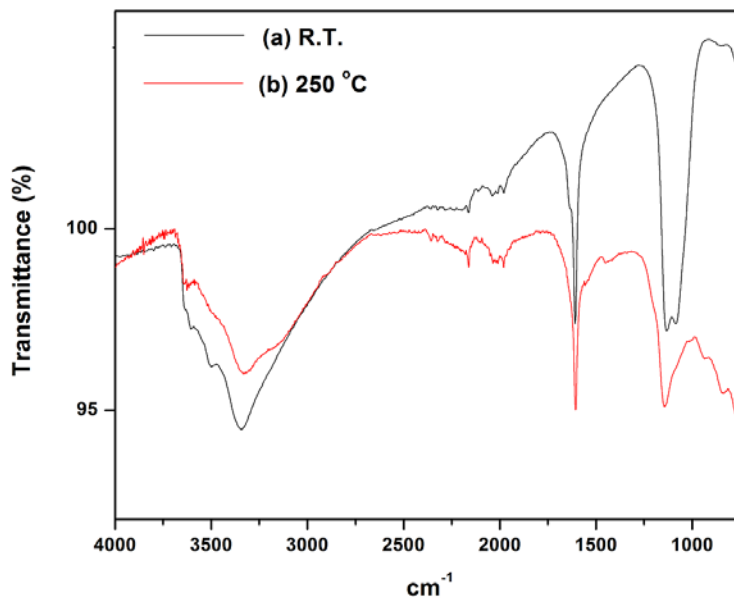
| Band (cm$^{-1}$) | Assignment |
|---|---|
| ~3300 | Stretching vibration of O-H in $H_2O$ |
| ~1600 | Bending vibration of O-H in $H_2O$ |
| ~1150 | Bending vibration of O-H in $H_2O$ |
| ~700 | Vibration of Cr - F |

**Figure 6.6** IR spectra and assignment for (a) $CrF_3 \cdot 0.5H_2O$ at room temperature and (b) samples annealed at 250 $^{\circ}$C for 48 h under nitrogen atmosphere.

**UV-Vis Diffuse Reflectance Spectroscopy.** The UV-Vis diffuse reflectance spectra were measured on ground crystals of $CrF_3 \cdot 0.5H_2O$ and the band gap energy of $CrF_3 \cdot 0.5H_2O$ have been determined from the reflectance spectra using the Kubelka-Munk function and the Tauc plot.[23-25] From the Tauc plot of $[F(R)eV]^{1/2}$ versus eV for

$CrF_3 \cdot 0.5H_2O$, the optical band gap of $CrF_3 \cdot 0.5H_2O$ is estimated to be approximately 1.72 eV, which is consistent with dark-green color of the material. Four bands are observed in the absorption spectra. One small band near 250 nm indicates metal-to-ligand charge transfer. Three bands between 300 nm to 800 nm indicate spin allowed d-d transition of $Cr^{3+}(d^3)$ (See Figure 6.7).[26]
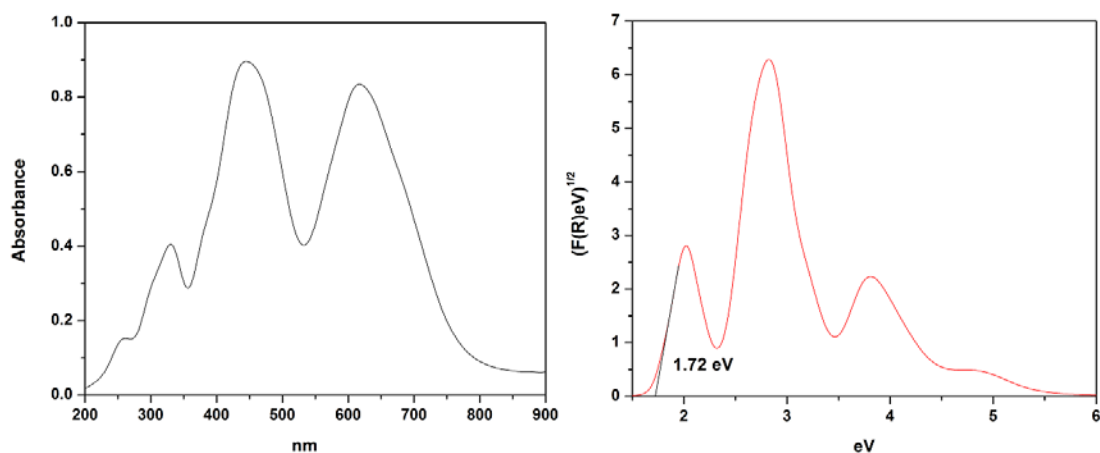


| Absorption (nm) | Assignment |
|:---:|:---:|
| 254 | Charge Transfer |
| 328 | $^4A_{2g} \rightarrow {}^4T_{1g}(P)$ |
| 445 | $^4A_{2g} \rightarrow {}^4T_{1g}(F)$ |
| 619 | $^4A_{2g} \rightarrow {}^4T_{2g}$ |

**Figure 6.7** The UV-Vis diffuse reflectance spectra, Tauc plot of $[F(R)eV]^{1/2}$ versus eV and assignment for $CrF_3 \cdot 0.5H_2O$.

**Magnetic Property** The dc magnetic susceptibility of $CrF_3 \cdot 0.5H_2O$ was measured under 100 Oe in the temperature range 2-300 K and is shown as $\chi$ and $\chi^{-1}$ versus T plots in Figure 6.8a and Figure 6.8b, respectively. From the inverse susceptibility versus temperature shown in Figure 6.8b, the susceptibility data were fit to the Curie-Weiss law, $\chi = C / (T - \theta)$ for T > 25 K, where C is the Curie constant and $\theta$ is the Weiss constant. The Curie constant is 1.83 emu K $mol^{-1}$ and the Weiss constant is -125.89 K, which are extracted from the curve fitting. On the basis of fit, the effective magnetic moment is 3.83 $\mu_B$/f.u. The theoretical spin only value is 3.87 $\mu_B$/f.u.($Cr^{3+}$), in good agreement with the data. The large negative Weiss constant indicates strong anti-ferromagnetic interactions between $Cr^{3+}$ moments. The 180° type super-exchange couplings between $Cr^{3+}$ and $Cr^{3+}$ connected by $F_{2p}$ orbitals ($Cr^{3+}$ - $F_{2p}$ - $Cr^{3+}$) give rise to strong anti-ferromagnetic interactions according to the Goodenough-Kanamori rule.[27-29] The divergence between zero-field cooled (ZFC) and field cooled (FC) magnetic susceptibility below 4.5 K indicates that material could have a non-aligned magnetic structure attributable to the presence of geometrical frustration. More detailed magnetic measurements such as ac magnetic susceptibility and neutron diffraction are required to understand the magnetic behavior of $CrF_3 \cdot 0.5H_2O$.
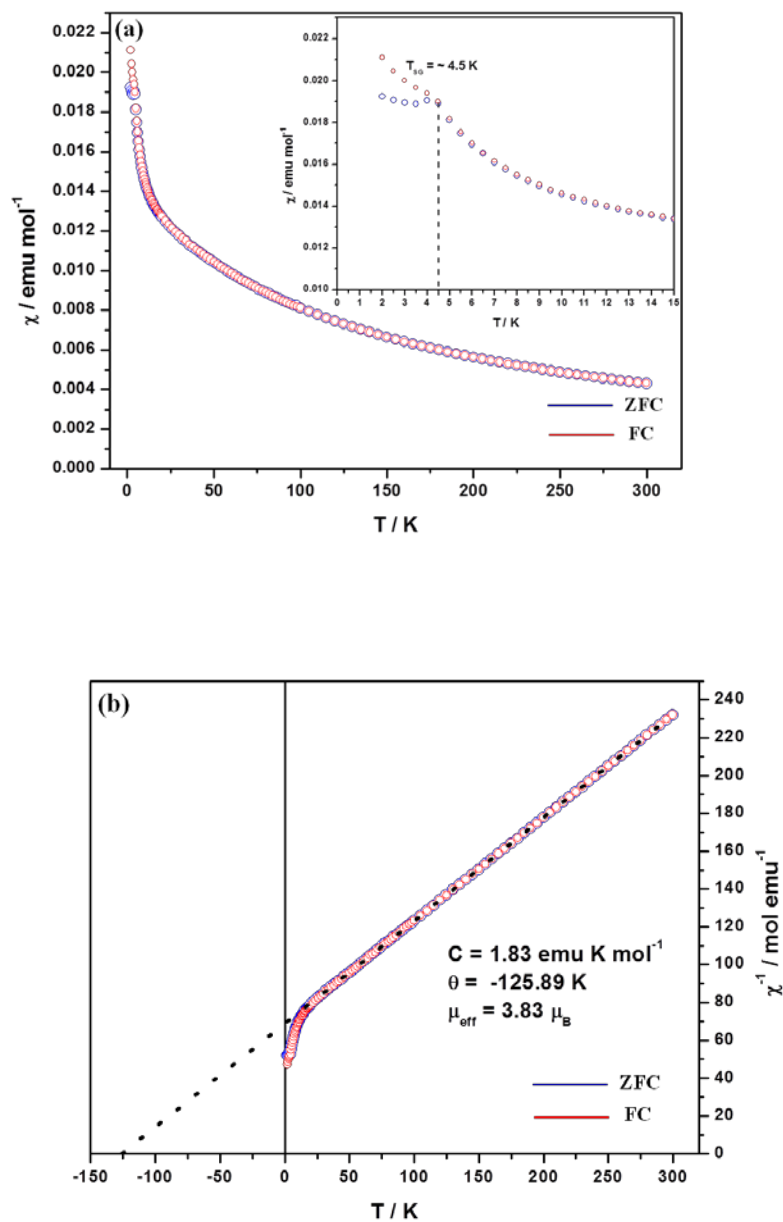
**Figure 6.8** Temperature dependence of (a) the magnetic susceptibility measured in 100 Oe, and (b) the inverse magnetic susceptibility with a Curie-Weiss fit (dotted line). The inset to (a) shows a close up of the low-temperature region revealing the 4.5 K magnetic transition temperature.

## 6.5 Conclusion

We have synthesized and characterized a new cubic pyrochlore-related material, $CrF_3 \cdot 0.5H_2O$. This material showed strong antiferromagentic interactions with a magnetic transition at 4.5 K. More detailed magnetic measurements such as ac magnetic susceptibility and neutron diffraction are required to confirm spin glass behavior of $CrF_3 \cdot 0.5H_2O$.

## 6.6 References

(1)     Ramirez, A. *Comments. Cond. Mat. Phys.* **1996**, *18*, 21.

(2)     Kim, S. W.; Kim, S.-H.; Halasyamani, P. S.; Green, M. A.; Bhatti, K. P.; Leighton, C.; Das, H.; Fennie, C. *J. Chem. Sci.* **2012**, *3*, 741.

(3)     Shimakawa, Y.; Kubo, Y.; Manako, T. *Nature (London)* **1996**, *379*, 53.

(4)     Sakai, H.; Yoshimura, K.; Ohno, H.; Kato, H.; Kambe, S.; Walstedt, R. E.; Matsuda, T. D.; Haga, Y.; Onuki, Y. *J. Phys.: Condens. Matter* **2001**, *13*, L785.

(5)     Shrout, T. R.; Halliyal, A. *Am. Ceram. Soc. Bull.* **1987**, *66*, 704.

(6)     Babel, D.; Pausewang, G.; Viebahn, W. *Z. Naturforsch., B* **1967**, *22*, 1219.

(7)     Babel, D. *Z. Anorg. Allg. Chem.* **1972**, *387*, 161.

(8)     Zinkin, M. P.; Harris, M. J.; Zeiske, T. *Phys. Rev. B: Condens. Matter* **1997**, *56*, 11786.

(9)     Canals, B.; Lacroix, C. *Phys. Rev. B: Condens. Matter Mater. Phys.* **2000**, *61*, 1149.

(10)     Ferey, G.; LeBlanc, M.; De, P. R. *J. Solid State Chem.* **1981**, *40*, 1.

(11)     Baum, E.; Dahlke, P.; Kaiser, V.; Molinier, M.; Schmidt, R. E.; Pebler, J.; Massa, W.; Babel, D. *Z. Anorg. Allg. Chem.* **2006**, *632*, 2244.

(12)     Molokeev, M. S.; Bogdanov, E. V.; Misyul, S. V.; Tressaud, A.; Flerov, I. N. *J. Solid State Chem.* **2013**, *200*, 157.

(13)     Herron, N.; Thorn, D. L.; Harlow, R. L.; Jones, G. A.; Parise, J. B.; Fernandez-Baca, J. A.; Vogt, T. *Chem. Mater.* **1995**, *7*, 75.

(14)     Kemnitz, E.; Hess, A.; Rother, G.; Troyanov, S. *J. Catal.* **1996**, *159*, 332.

(15)     Barthelet, K.; Marrot, J.; Riou, D.; Ferey, G. *J. Solid State Chem.* **2001**, *162*, 266.

(16)     Li, C.; Yin, C.; Gu, L.; Dinnebier, R. E.; Mu, X.; van Aken, P. A.; Maier, J. *J. Am. Chem. Soc.* **2013**, *135*, 11425.

(17)     De Pape, R.; Ferey, G. *Mater. Res. Bull.* **1986**, *21*, 971.

(18)     Kim, S. W.; Chang, H. Y.; Halasyamani, P. S. *J. Am. Chem. Soc.* **2010**, *132*, 17684.

(19)     Brown, I. D.; Altermatt, D. *Acta Cryst.* **1985**, *B41*, 244.

(20)     Brese, N. E.; O'Keeffe, M. *Acta Cryst.* **1991**, *B47*, 192.

(21)     Brown, I. D. *The Chemical Bond in Inorganic Chemistry - The Bond Valence Model. IUCr monographs on Crystallography 12*; Oxford University Press, 2002.

(22)     Nakamoto, K. *Infrared and Raman Spectra of Inorganic and Coordination Compounds Part A: Theory and Applications in Inorganic Chemistry*; 5th ed.; John Wiley & Sons, Inc: New York, 1997.

(23)     Kubelka, P. M.; Munk, F. Z. *Tech. Phys.* **1931**, *12*, 593.

(24)     Tauc, J.; Grigorovici, R.; Vancu, A. *physica status solidi (b)* **1966**, *15*, 627.

(25)     Tauc, J. *Mater. Res. Bull.* **1970**, *5*, 721.

(26)     Lever, A. B. P. *Inorganic Electronic Spectroscopy, 2nd ed.*; Elsevier Science Publishers B. V.: Amsterdam, 1984.

(27)     Goodenough, J. B. *Phys. Rev.* **1955**, *100*, 564.

(28)     Kanamori, J. *J. Phys. Chem. Solid* **1959**, *10*, 87.

(29)     Goodenough, J. B. *Magnetism and the Chemical Bond*; Interscience: New York, 1963.

**Table 6.1** Crystallographic Data for $CrF_3 \cdot 0.5H_2O$.

| Parameter | $CrF_3 \cdot 0.5H_2O$ |
|:---:|:---:|
| F.W. | 117.00 |
| $T$ (K) | 296(2) |
| $\lambda$ (Å) | 0.71073 |
| Crystal System | Cubic |
| Space Group | $Fd\text{-}3\,m$ (No.227) |
| $a = b = c$ (Å) | 10.2584(6) |
| $V$ (Å$^3$) | 1079.54(19) |
| $Z$ | 16 |
| $\rho_{calcd}$ (g/cm$^3$) | 2.879 |
| $\mu$(mm$^{-1}$) | 4.077 |
| $2\theta_{max}$ (deg) | 57.056 |
| $R$ (int) | 0.0247 |
| GOF | 1.256 |
| $R$ $(F)$[a] | 0.0197 |
| $R_w$ $(F_o{}^2)$[b] | 0.0516 |

[a]$R$ $(F) = \Sigma||F_o| - |F_c||/\Sigma|F_o|$ , [b]$R_w$ $(F_o{}^2) = [\Sigma w(F_o{}^2 - F_c{}^2)^2/\Sigma w(F_o{}^2)^2]^{1/2}$

**Table 6.2** Atomic Coordinates for $CrF_3 \cdot 0.5H_2O$.

| Atom | x | y | z | $U_{eq}(\mathring{A}^2)^a$ |
|------|------|------|------|------|
| **Cr(1)** | 0.5 | 0.5 | 0 | 0.0074(5) |
| **F(1)** | 0.4343(2) | 0.625 | 0.125 | 0.0169(6) |
| **Ow(1)**[b] | 0.3944(9) | 0.3944(9) | 0.3944(9) | 0.0300(7) |

[a] $U_{eq}$ is defined as one-third of the trace of the orthogonal $U_{ij}$ tensor.

[b] The site occupancy factor for these atoms is 0.25.

**Table 6.3** Selected Bond Distances and Angles for $CrF_3 \cdot 0.5H_2O$.

| Bond | Distance ($\mathring{A}$) | Bond | Distance ($\mathring{A}$) |
|------|------|------|------|
| **Cr(1) — F(1)** | $1.9347(8) \times 6$ | **Cr(1) — Cr(1)** | 3.6269(2) |
| **F(1) — Ow(1)** | $2.9866(2) \times 2$ | | |

| | Angle ($^o$) | | Angle ($^o$) |
|------|------|------|------|
| **F(1) — Cr(1) — F(1)** | 88.70(9) | **Cr(1) — F(1) — Cr(1)** | 139.21(13) |
| **F(1) — Cr(1) — F(1)** | 91.30(9) | | |
| **F(1) — Cr(1) — F(1)** | 180.0 | | |

**Table 6.4** Bond valence analysis for $CrF_3 \cdot 0.5H_2O^a$.

| Atom | F(1) | Ow(1) | $\Sigma_{cations}$ |
|---|---|---|---|
| **Cr(1)** | $^{[x2]}$ 0.4722$^{[x6]}$ | - | **2.83** |
| $\Sigma_{anions}$ | **0.944** | - | |

[a] Bond valence sums calculated with the formula: $S_i = \exp[(R_0-R_i)/B]$, where $S_i$=valence of bond "$i$" and B=0.37. Superscripts indicate the # of equivalent bonds for anions; subscripts indicate that the # of equivalent bonds for cations.

## CHAPTER 7. Conclusions and Future Work

## 7.1 General conclusions

Through exploratory synthesis techniques, the attempts to synthesize new multiferroic fluoride materials resulted in several new transition metal ($Fe^{2+}/Fe^{3+}$, $Mn^{2+}/Mn^{3+}$, and $Cr^{3+}$) fluoride materials. All of the materials in this dissertation were synthesized by hydrothermal techniques using $CF_3COOH$ aqueous solution instead of aqueous HF.[1] The crystal structures of the materials were characterized by single crystal diffraction, and the purity of their bulk phases was confirmed by powder X-ray diffraction. As a general characterization, infrared (IR), UV-vis diffuse reflectance spectroscopy, thermogravimetric analysis (TGA), differential thermal analysis (DTA) were utilized to obtain vibrational modes, band gaps, and thermal behavior of the reported materials.[2-6] The bond valence sum (BVS)[7-9] calculation was used for the determination of the oxidation state of transition metal ions. For mixed valence iron ($Fe^{2+}/Fe^{3+}$) fluoride materials, $^{57}$Fe-Mössbauer spectroscopy was used to characterize the ratio of $Fe^{2+}$ and $Fe^{3+}$.[10] The magnetic behavior of materials were investigated by a commercial SQUID (Superconducting Quantum Interference Device) magnetometer (Quantum Design) or a Quantum Design Physical Property Measurement System (PPMS) as a function of temperature from 2.0 to 300 K.

In mixed valence system, charge ordering or magnetic ordering could be observed and would generate some unexpected physical properties such as electronic ferroelectricity and magnetic ferroelectricity, even in materials that do not belong to polar space

groups.[11-13] However, these kinds of phenomena have mostly been observed in oxide system, e.g., $Fe_3O_4$ and $LuFe_2O_4$.[11,14] Because of difficulties of preparation of new mixed metal fluoride material, especially materials containing mixed valence transition metal cations ($Fe^{2+}/Fe^{3+}$, $Mn^{2+}/Mn^{3+}$, $Cr^{2+}/Cr^{3+}$) with geometrical or magnetic frustration, very few materials have been investigated. Also well-defined crystal structures as well as characterization of many fluoride materials are lacking. In this dissertation, a new synthetic method using $CF_3COOH$ aqueous solution under hydrothermal conditions was applied to synthesize new mixed metal fluoride materials with mixed valence transition metal cations ($Fe^{2+}/Fe^{3+}$, $Mn^{2+}/Mn^{3+}$). They were then characterized by various spectroscopy techniques, investigation of the possibility of electronic ferroelectricity or magnetic ferroelectricity in newly synthesized mixed valence transition metal fluoride materials for multiferroic properties performed. Even though I did not successfully synthesize new multiferroic fluoride materials, the newly prepared fluoride materials showed various structural forms (pyrochlore, layered perovskite, or chain) as well as interesting magnetic properties such as magnetic frustration. It is very difficult to find new synthetic strategies to generate ferroelectricity in mixed metal fluoride materials. However, this dissertation could give useful information to design and synthesize new mixed metal fluoride materials with multiferroic property.

## 7.2 $RbFe_2F_6$ system

A new charge-ordered magnetically frustrated mixed-metal fluoride with a pyrochlore-related structure, $RbFe_2F_6$ has been synthesized through hydrothermal techniques using

CF$_3$COOH aqueous solution.[1,15] The crystal structure of RbFe$_2$F$_6$ was determined by single crystal X-ray diffraction, and the material was characterized by infrared, UV-vis, [57]Fe-Mössbauer spectroscopy and thermal analyses. The material exhibits a three-dimensional pyrochlore-related structure consisting of corner-shared Fe$^{2+}$F$_6$ and Fe$^{3+}$F$_6$ octahedra. Ordering of the Fe$^{2+}$ and Fe$^{3+}$ cations leads to the lowering of crystallographic symmetry (cubic to orthorhombic). No structural phase transformation is detected from the variable-temperature neutron diffraction data. Magnetic data clearly reveal strong anti-ferromagnetic interactions (a Curie–Weiss temperature of -270 K) but sufficient frustration to prevent ordering until 16 K. More detailed magnetic measurements, calculation, and neutron diffraction study are in progress to understand the magnetic properties as well as possible other physical properties. Efforts to synthesize new mixed valence transition metal (Fe$^{2+}$/Fe$^{3+}$, Mn$^{2+}$/Mn$^{3+}$, Cr$^{2+}$/Cr$^{3+}$) fluoride materials with pyrochlore-related structure are also in progress.

## 7.3 K$_4$Fe$_3$F$_{12}$ system

A new mixed valence iron (Fe$^{2+}$/Fe$^{3+}$) fluoride material with a layered perovskite-related structure, K$_4$Fe$_3$F$_{12}$ has been synthesized through hydrothermal method using CF$_3$COOH aqueous solution.[1] The crystal structure of K$_4$Fe$_3$F$_{12}$ was determined by single crystal X-ray diffraction, and the material was characterized by infrared, UV-vis, [57]Fe-Mössbauer spectroscopy and thermal analyses. The material exhibits a layered perovskite structure consisting of corner-shared Fe$^{2+}$F$_6$ and Fe$^{3+}$F$_6$ octahedra. Each corner-shared FeF$_6$ octahedron is formed the perovskite layers in an ordered fashion; the

$Fe^{2+}F_6$ octahedral layer is sandwiched by two $Fe^{3+}F_6$ layers. Interestingly, this is very rare example, showing a layered perovskite structure in a fluoride system. Magnetic data showed ferrimagnetic behavior (Tc = ~120 K). More detailed magnetic measurements and neutron diffraction study are in the progress to understand the magnetic properties as well as possible other physical properties. Efforts to synthesize new mixed valence transition metal ($Fe^{2+}/Fe^{3+}$, $Mn^{2+}/Mn^{3+}$, $Cr^{2+}/Cr^{3+}$) fluoride materials with a layered perovskite structure are also in progress.

## 7.4 $Ba_3Mn_3F_{14}$ and $NaBa_7Mn_7F_{34}$ system

Two new mixed valence manganese ($Mn^{2+}/Mn^{3+}$) fluoride materials, $Ba_3Mn_3F_{14}$ and $NaBa_7Mn_7F_{34}$ have been synthesized by hydrothermal method using $CF_3COOH$ aqueous solution,[1] and their crystal structures were determined by single crystal X-ray diffraction. The aqueous solution of $CF_3COOH$ acted as a reducing agent, and reduced some of the $Mn^{3+}$ to $Mn^{2+}$ during hydrothermal reaction. Those materials were characterized by infrared, UV-vis, and thermal analyses. The oxidation states of manganese were determined by the bond valence sum (BVS) calculation. $Ba_3Mn_3F_{14}$ exhibits a one-dimensional chain structure consisting of separate edge-shared $Mn^{2+}F_6$ trigonal prism and corner-shared $Mn^{3+}F_6$ distorted octahedra that run along the b-direction. $NaBa_7Mn_7F_{34}$ exhibits a Jarlite-type structure consisting of corner-shared $Mn^{2+}F_6$, $(Mn^{2+}/Mn^{3+})F_6$ and $Mn^{3+}F_6$ distorted octahedra, which forms infinite helicoidal double-chains along the *b*-axis. $Ba_3Mn_3F_{14}$ showed anti-ferromagnetic behavior at 7 K and also observed field induced spin flop transition below a Néel temperature at the field of ~1.5

T attributable to inter-chain interactions. $NaBa_7Mn_7F_{34}$ showed Ferrimagnetic behavior at ~ 5 K and also very weak spontaneous magnetization was observed between -2 and 2 T attributable to inter-chain interaction in the crystal structure. More detailed magnetic measurements of $Ba_3Mn_3F_{14}$ and $NaBa_7Mn_7F_{34}$ are in progress. The efforts to synthesize new mixed valence manganese ($Mn^{2+}/Mn^{3+}$) fluoride materials using hydrothermal method using $CF_3COOH$ aqueous solution are also in progress.

## 7.5 CrF$_3$·0.5H$_2$O system

A new cubic pyrochlore-related mixed-metal fluoride material, $CrF_3·0.5H_2O$ has been synthesized and characterized. This material was synthesized through mild hydrothermal conditions using aqueous $CF_3COOH$ solution.[1] The crystal structure of $CrF_3·0.5H_2O$ was determined by single crystal X-ray diffraction. The material was characterized by infrared, UV-vis, and thermal analyses. The material exhibits a three-dimensional pyrochlore-related structure consisting of corner-shared $Cr^{3+}F_6$ and isolated water molecules. The oxidation state of chromium was determined by the bond valence sum (BVS) calculation and it was also confirmed by magnetic measurement. Magnetic behavior indicates strong anti-ferromagnetic interactions with magnetic transition at 4.5 K. More detailed magnetic measurements such as ac magnetic susceptibility measurement are in progress to understand magnetic behavior in $CrF_3·0.5H_2O$. Attempts to synthesize new mixed valence chromium ($Cr^{2+}/Cr^{3+}$) fluoride materials using $CrF_3·0.5H_2O$ as a starting material are still in progress.

**7.6 References**

(1)     Kim, S. W.; Chang, H. Y.; Halasyamani, P. S. *J. Am. Chem. Soc.* **2010**, *132*, 17684.

(2)     Kubelka, P. M.; Munk, F. Z. *Tech. Phys.* **1931**, *12*, 593.

(3)     Tauc, J.; Grigorovici, R.; Vancu, A. *physica status solidi (b)* **1966**, *15*, 627.

(4)     Tauc, J. *Mater. Res. Bull.* **1970**, *5*, 721.

(5)     Lever, A. B. P. *Inorganic Electronic Spectroscopy, 2nd ed.*; Elsevier Science Publishers B. V.: Amsterdam, 1984.

(6)     Nakamoto, K. *Infrared and Raman Spectra of Inorganic and Coordination Compounds Part A: Theory and Applications in Inorganic Chemistry*; 5th ed.; John Wiley & Sons, Inc: New York, 1997.

(7)     Brown, I. D.; Altermatt, D. *Acta Cryst.* **1985**, *B41*, 244.

(8)     Brese, N. E.; O'Keeffe, M. *Acta Cryst.* **1991**, *B47*, 192.

(9)     Brown, I. D. *The Chemical Bond in Inorganic Chemistry - The Bond Valence Model. IUCr monographs on Crystallography 12*; Oxford University Press, 2002.

(10)    Long, G. J.; Grandjean, F. *Mössbauer Spectroscopy Applied to Magnetism and Materials Science.*; Plenum Press: New York, 1993.

(11)    Khomskii, D. I. *J. Magn. Magn. Mater.* **2006**, *306*, 1.

(12)    Cheong, S.-W.; Mostovoy, M. *Nat. Mater.* **2007**, *6*, 13.

(13)    van, d. B. J.; Khomskii, D. I. *J. Phys.: Condens. Matter* **2008**, *20*, 434217/1.

(14)    Ikeda, N.; Ohsumi, H.; Ohwada, K.; Ishii, K.; Inami, T.; Kakurai, K.; Murakami, Y.; Yoshii, K.; Mori, S.; Horibe, Y.; Kito, H. *Nature (London, U. K.)* **2005**, *436*, 1136.

(15)     Kim, S. W.; Kim, S.-H.; Halasyamani, P. S.; Green, M. A.; Bhatti, K. P.;

Leighton, C.; Das, H.; Fennie, C. J. *Chem. Sci.* **2012**, *3*, 741.